# Polymer Electrolyte Membrane Fuel Cells: Aging and Dynamic behaviour

Luis Carlos Pérez Martínez

Dissertation presented for the degree of

Doctor in Chemical and Biological Engineering

by

Porto University

Supervisors

Adélio Miguel Magalhães Mendes

José Manuel Ribeiro de Sousa

**LEPAE - Laboratory of Engineering Processes, Environment and Engineering**

Chemical Engineering Department

Faculty of Engineering – University of Porto

Porto, 2013

FCT Fundação para a Ciência e a Tecnologia
MINISTÉRIO DA CIÊNCIA, TECNOLOGIA E ENSINO SUPERIOR

# Acknowledgments

I acknowledge the Portuguese Foundation of Science and Technology (FCT) for my PhD grant reference SFRH/BD/44684/2008. Financial support of FCT through projects PTDC/EQU-EQU/70574/2006 and PTDC/EQU-EQU/104217/2008 is acknowledged too. The financial support received from VTT – The Technical Research Centre of Finland during my visits in 2010 and 2012 is acknowledged as well.

I want to thank my supervisors, Professors Adélio Mendes and José Sousa for providing me the outstanding opportunity of studying my PhD at FEUP. I appreciate all their support throughout the duration of my studies.

During this journey I met a lot of incredible people. It would be impossible to mention all of them; however, the work presented in this thesis would not have been possible without the support of Dr. Lucia Brandão, who helped me to build confidence during the first part of my PhD. Her husband, José Luis, was a key person for my integration in the Portuguese society. Their support and friendship proved to be invaluable to me.

I would like to highlight the support of Dr. Marta Boaventura. It would have been really interesting to arrive earlier to the faculty and learn more from her. She was especially empathetic during the last part of my PhD and it would not have been possible, literally, to deliver my thesis without her kind help.

My deepest gratitude to Dr. Jari Ihonen of VTT. Without his guidance and patience this work could not have been possible. Apart of giving me the nice opportunity of visiting Finland, he taught me technical and not so technical things that will be really important for my life.

A few words to my wife, Joana. She was always by my side supporting me in the bad times. I feel simply blessed for having this wonderful woman to share my life with and for that reason this work is mostly dedicated to her.

To my family, I always felt your love and support despite the distance. You were always there taking care of me. This work is also a gift for them.

Last but not least, I want to express my endless gratitude to my father and mother in law, José Luis and Teresa. They showed how much they appreciate me during this time and this work is a present for them.

To the best indoor soccer players of Portugal, the people of the FEUPsal team, are worth to mention since we spent great times together.

To Portugal, from where I learnt the word “saudade” and to Finland, from where I learnt the word “sisu”. These words have no translation in other languages so they show how much I learnt a lot from these countries and their people.

Last but not least, I would like to express my gratitude to Olivier Thomann of VTT for the last minute translation of the abstract to French.

## Abstract

This thesis targets the study of Polymer Electrolyte Membrane Fuel Cells (PEMFC) operating between 60-80 °C. This topic is of extreme importance since PEMFC may substitute heat engines as the main energy conversion technology for small stationary and transportation applications during the 21st century due to their higher efficiency and environmental friendliness.

Firstly, it is presented a comprehensive literature review concerning segmented PEMFC (SFC). It is highlighted that the local electrochemical activity of PEMFC varies as a consequence of the interaction between several parameters. The different types of SFC are categorized and fundamental considerations for their construction are provided. It is shown how SFC are useful to study: i) the influence of the design, assembly and operating parameters of the cell on the local electrochemical activity of PEMFC and ii) the spatial distribution of gaseous species, water and temperature.

The local electrochemical activity of a SFC operated in fuel recirculation mode is evaluated at 60 °C with the purpose of understanding the distribution of water within the cell. Current density distribution (CDD) measurements are obtained for steady state conditions and water balance and mean gas velocity calculations are performed. Local flooded and dried zones of the cell are highlighted. It is concluded that the recirculation rate strongly influences the distribution of water within the cell, in contrast to other parameters such as anode pressure and purge frequency. Furthermore, a technique for improving the accuracy of local electrochemical activity measurements is introduced.

A methodology to mitigate the effect of CO in PEMFC for stationary applications is described. The methodology minimizes the amount of $O_2$ fed along with the $H_2$-CO mixture in order to oxidize the CO. For this, a novel arrangement of cells with similarities to SFC is assembled and the anode exhaust gas composition is analyzed with a gas chromatograph. Furthermore, the amount of CO adsorbed onto the catalyst and the fraction of catalytic sites covered by CO are estimated. It is found

that air volumetric flow rates below 1.0% (relative to the $H_2$ volumetric flow rate) are enough to mitigate the effect of CO at concentrations between 13-19 ppm and a cell operating temperature of 65 °C.

The effect of fuel utilization on the dynamics of CO poisoning is studied under operating conditions and CO concentrations relevant for automotive PEMFC systems. Specifically, a membrane electrode assembly (MEA) with an anode catalyst loading of 0.05 mg Pt $cm^{-2}$ and a cell temperature of 80 °C is used. Moreover, three fuel utilizations, 70%, 40% and 25% and CO concentrations between 0.18-1 ppm are used. The anode exhaust gas composition is analyzed with a gas chromatograph. It is shown that the fuel utilization strongly influences the dynamics of CO poisoning in PEMFC. It is demonstrated that as the fuel utilization decreases, the molar flow rate of CO at the anode outlet increases, leading to a slower decrease in performance of the cell.

# Sumário

A presente tese foca o estudo de células de combustível de electrólito de membrana polimérica com alimentação de hidrogénio (PEMFC), que operam entre 60-80 °C. Este tópico é de extrema importância dado que as PEMFC podem substituir os motores térmicos como a principal tecnologia de conversão de energia para aplicações estacionárias de pequena dimensão e de transportes no século 21, devido à sua maior eficiência e menor impacto ambiental.

Esta tese apresenta primeiramente uma revisão da literatura sobre PEMFC segmentadas (SFC). É realçada a variação da atividade eletroquímica local das PEMFC em consequência da interação entre diversos parâmetros. Os diferentes tipos de SFC são categorizados e fornecidas considerações fundamentais para a sua construção. A utilidade das SFC é demonstrada para o estudo da i) influência do *design*, montagem e dos parâmetros de operação na actividade electroquímica local da PEMFC e da ii) distribuição espacial das espécies gasosas, água e temperatura.

A actividade electroquímica local de uma SFC, operando a 60 °C e com recirculação de combustível, é avaliada de forma a compreender a distribuição de água na célula. Foram obtidas medições de distribuição de densidades de corrente em estado estacionário e foram calculados o balanço de água e a velocidade média de gás, tendo sido realçadas as zonas da célula que estão encharcadas e aquelas que estão secas. Conclui-se que a velocidade de recirculação influencia de forma significativa a distribuição de água na célula, contrastando com outros parâmetros como a pressão no ânodo e a frequência de purga. Foi ainda introduzida uma técnica para melhorar a precisão das medições de distribuição de densidades de corrente.

No decorrer deste trabalho é desenvolvida uma metodologia para mitigar o efeito do monóxido de carbono (CO) na PEMFC, em estado estacionário. Esta metodologia baseia-se numa nova configuração de células com similaridades a SFC, que minimiza a quantidade de oxigénio alimentado juntamente com a mistura $H_2$-CO, de forma a oxidar o CO. O gás à saída do ânodo foi analisado por cromatografia gasosa e a

quantidade de CO adsorvido no catalisador e a fração de locais activos ocupados por CO foram estimados. Foi observado que, para uma célula a operar a 65 °C, um caudal de ar inferir a 1.0% (relativamente ao caudal de H2) é suficiente para mitigar o efeito do CO a concentrações entre 13-19 ppm.

O efeito da utilização de combustível na dinâmica de envenenamento por CO foi estudado a 80 °C em conjuntos membrana /eléctrodos (MEAs) com carga de platina no ânodo de 0.05 mg Pt $cm^{-2}$. Foram utilizadas concentrações de CO relevantes para aplicação automóvel, entre 0.18-1 ppm. O gás à saída do ânodo foi analisado recorrendo a cromatografia gasosa. Foi demostrado que a utilização de combustível influencia fortemente a dinâmica de envenenamento da PEMFC. À medida que a utilização de combustível diminui, o fluxo molar de CO à saída do ânodo aumenta, originando uma menor diminuição de desempenho da célula.

# Sommaire

Cette thèse porte sur l'étude des piles à combustible à membrane électrolyte polymère (PEMFC) fonctionnant entre 60-80 °C. Ce sujet d'étude est important car les PEMFC pourraient remplacer les moteurs thermiques en tant que principale technologie de conversion d'énergie pour les applications stationnaires petites et de transport pendant le 21ème siècle grâce à leur haute efficacité et leur faible impact environnemental.

Ce travail commence par une revue exhaustive de la littérature au sujet des PEMFC segmentées (SFC). Il est mis en évidence que l'activité électrochimique locale des PEMFC varie en conséquence de l'interaction de plusieurs paramètres. Les différents types de SFC sont catégorisés et des considérations fondamentales pour leurs constructions sont fournies. Il est expliqué comment les SFC sont utiles à l'étude de: i) l'influence des principales conceptions, assemblages et paramètres de fonctionnement sur l'activité électrochimique locale de la PEMFC et ii) la distribution spatiale d'espèces gazeuses, de l'eau et de la température.

L'activité électrochimique locale d'une SFC fonctionnant avec recirculation du combustible a été évaluée à 60 °C dans le but d'étudier la distribution de l'eau dans la pile. Des mesures de distribution de la densité du courant (CDD) ont été obtenues à condition stable et le bilan d'eau et la vitesse moyenne des gaz ont été calculés. Les zones inondées et sèches de la pile sont mises en évidence. Il est conclu que le taux de recirculation influence fortement la distribution de l'eau dans la pile, au contraire d'autres paramètres comme la pression anodique et la fréquence des purges. De plus, une technique pour améliorer la précision de la mesure de l'activité électrochimique locale est présentée.

Une méthodologie pour diminuer l'effet d'empoisonnement au CO dans les PEMFC pour applications stationnaires a été développée. La méthodologie minimise la quantité d'$O_2$ injecté avec le mélange de $H_2$-CO afin d'oxyder le CO. Pour cela, un nouvel arrangement de piles similaire au SFC a été assemblé et la composition des gaz d'échappement de l'anode a été analysée avec un équipement de

chromatographie en phase gazeuse. En plus, la quantité de CO adsorbé sur le catalyseur et la fraction de sites catalytiques couverte par le CO est estimée. Il a été trouvé qu'un débit d'air en dessous de 1.0% (relativement au débit d'H2) est suffisant pour atténuer l'effet du CO à des concentrations entre 13-19 ppm et avec une pile fonctionnant à 65 °C.

L'effet de l'utilisation du combustible sur la dynamique de l'empoisonnement au CO est étudié en condition de fonctionnement et avec des concentrations de CO pertinentes pour des systèmes automobile de PEMFC. Spécifiquement, un assemblage d'électrode membranaire (MEA) avec 0.05 mg Pt $cm^{-2}$ sur l'anode, une concentration de CO entre 0.18-1 ppm et une pile fonctionnant à 80 °C ont été utilisés. La composition des gaz d'échappement a été analysée avec un équipement de chromatographie en phase gazeuse. Il a été montré que l'utilisation du combustible influence fortement la dynamique d'empoisonnement au CO d'une PEMFC. Il est démontré que pour une moindre utilisation du combustible, le débit molaire de CO à la sortie de l'anode augmente, ce qui se traduit par une plus lente diminution de performance de la pile.

# Contents

## Figure Captions

## Table captions

# Chapter I

# Chapter 1 - Introduction

## 1.1. The energy challenge

The current energy system faces critical challenges related to its lack of sustainability, low stability and low efficiency. The supply and demand of energy relies mostly on burning fossil fuels to produce heat and power at the lowest price. According to the International Energy Agency, 81% of the world´s primary energy demand came from oil, coal and natural gas in 2010 [1]. The lack of sustainability of the system is visible from the fact that fossil fuels reserves are finite while the low stability of the system becomes evident from the fact that the reserves are located in different geographic zones from where they are intensively demanded.

Furthermore, the use of fossil fuels has led to growing environmental concerns associated to the discharge of carbon dioxide ($CO_2$), methane ($CH_4$), nitrous oxide ($N_2O$) and volatile organic compounds (VOCs) to the atmosphere. These gases represent a public health threat [2] and it is believed that most of them are responsible for climate change [3].

Figure 1.1 shows a Sankey diagram of the global energy system in 2010 [1]. The primary energy demand was complimented with renewable energy sources (mainly hydropower but also biomass, wind and solar) and nuclear energy which accounted for 13% and 6% of the total, respectively. In decreasing order, the energy demand by sector was: buildings with 2931 million tons of oil equivalent (Mtoe), industry with 2421 Mtoe, transportation with 2377 Mtoe and others with 970 Mtoe. The possibility of increasing the efficiency of the energy system becomes evident from the losses depicted in Figure 1.1, which accounted for 21% of the total energy generated.

The main prospective scenario outlined in the world energy outlook of 2012 indicates that the primary energy demand will rise by over one-third until 2035 in order to satisfy the needs of the fast growing population. Under that scenario, the consumption of natural gas, coal and oil increases 50%, 21% and 12% respectively. It

is projected that the share of renewable energy sources increases up to from 31% from the current 20%.

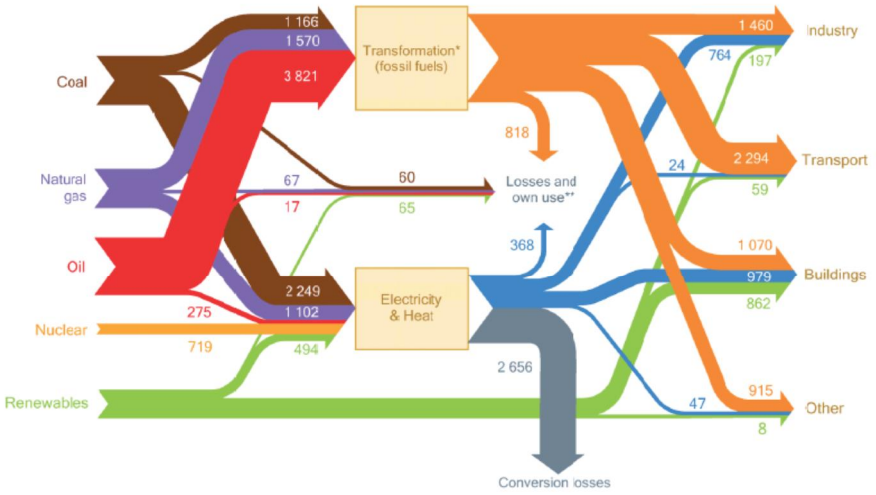


* Transformation of fossil fuels from primary energy into a form that can be used in the final consuming sectors. ** Includes losses and fuel consumed in oil and gas production, transformation losses and own use, generation lost or consumed in the process of electricity production, and transmission and distribution losses.

Figure 0.1. The global energy system in 2010 [1].

The increase in the energy demand and the environmental concerns have created a technological challenge to mankind. The nature of the energy system makes of heat engines the most popular energy conversion technology. The issues with heat engines are the emissions of noxious gases and their low efficiency, limited by the Carnot efficiency [4]. Renewable energy sources seem to be a good option, however, they are intermittent. Nuclear energy raises safety and security concerns and technical difficulties handling the residues.

As observed, there is a need for energy conversion technologies that: i) run on alternative fuels, ii) have higher efficiencies than heat engines, ii) operate independently of the weather and iv) minimize the environmental impact. It is believed that fuel cells incorporate such attributes which is why they are considered the most promising energy conversion technologies of the 21$^{st}$ century.

## 1.2. Fuel cells

### 1.2.1. Operating principles

The operating principles and main characteristics of fuel cells have remained the same since they were first conceptualized as a "gas battery" back in the 19$^{th}$ century by Sir William Grove [5]. Fuel cells are electrochemical devices that generate electrical energy and heat as long as fuel and oxidant are supplied. A simplified configuration of a fuel cell consists of an electrolyte with planar structure to which fuel and oxidant are fed in opposite sides – Figure 1.2. The electrolyte serves as barrier that prevents the direct combustion of the reactants and physically separates the anode and the cathode. The electrons are passed through an external circuit and reach the cathode while the ions migrate through the electrolyte to generate the products of the overall reaction.

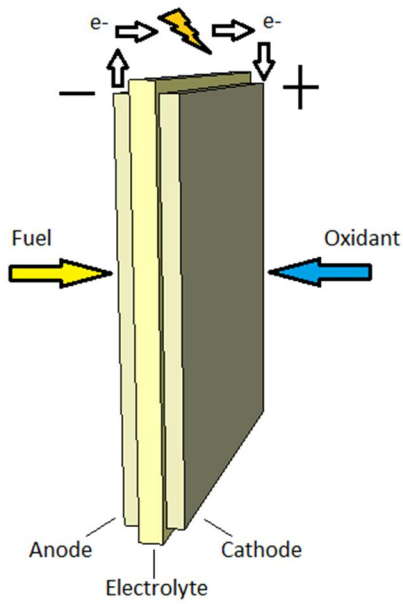


Figure 1.2. Simplified scheme of a fuel cell.

Fuel cells have similarities with both batteries and heat engines. The main similarity between fuel cells and batteries is the direct conversion of chemical into electrical energy. The main difference is that batteries produce electrical energy from the

chemical energy stored within them and fuel cells will produce it as long as reactants are fed. Either primary (disposable) or secondary (rechargeable) batteries are in disadvantage to fuel cells in the latter point. Regarding heat engines, the main similarity relies on the possibility of generating electrical energy and heat and as long as reactants are supplied. The main difference is that fuel cells generate electricity without intermediate heat exchange processes which is why they are more efficient.

### 1.2.2. Types of fuel cells

Fuel cells are typically classified according to their electrolyte and fuel [6]. Every type of fuel cell has advantages and disadvantages but all share common challenges regarding the development of materials for their construction, durability improvement, cost reduction and some of them the absence of fuel distribution infrastructure.

Solid oxide fuel cells (SOFC) use yttria stabilized zirconia (YSZ) as electrolyte. This solid state electrolyte transports $O^{2-}$ ions from the cathode to the anode. The anode is fed with different fuel sources such as hydrogen ($H_2$), reformed hydrocarbons ($CH_n$) or others that can be converted to syngas (an $H_2$-CO mixture) [7]. The cathode is fed with oxygen ($O_2$) from air and the products of the overall reaction are $H_2O$ and $CO_2$. This type of fuel cell can be further divided in: intermediate temperature SOFC (IT-SOFC), ranging between 500-750 °C, and high temperature SOFC (HT-SOFC), ranging between 850-1000 °C [8]. The operating temperature leads to slow start-ups and to difficulties in finding suitable materials for their construction. Nonetheless, SOFC are being actively integrated in combined heat and power (CHP) systems [9].

Molten carbonate fuel cells (MCFC) use lithium ($Li_2CO_3$), potassium ($K_2CO_3$) or sodium ($Na_2CO_3$) carbonate as electrolyte. The electrolyte is in liquid phase and transports $CO_3^{-2}$ ions from the cathode to the anode [10]. The anode is fed with $H_2$, $CH_n$ or syngas whilst the cathode is fed with $O_2$ from air and $CO_2$. The products of the reaction are $H_2O$ and $CO_2$. The typical operating temperature of 650 °C leads to slow start-ups while the corrosive nature of the electrolyte tends to accelerate degradation of the components.

Alkaline Fuel Cells (AFC) use potassium hydroxide (KOH) as electrolyte. The electrolyte is a liquid solution and transports hydroxyl $OH^-$ ions from the cathode to the anode [11]. The anode is fed with $H_2$ and the cathode with $O_2$ from air. The product of the reaction is $H_2O$. The operating temperature depends on the concentration of the electrolyte but is in the range of 60-250 °C. Even though lower operating temperatures provide faster start-ups; the low tolerance to $CO_2$ has limited the development of the technology as this compound depletes the electrolyte producing $K_2CO_3$ [12].

Phosphoric acid fuel cells (PAFC) use phosphoric acid ($H_3PO_4$) as electrolyte. The electrolyte is in liquid state and transports $H^+$ ions from the anode to the cathode. The anode is fed with $H_2$ and the cathode with $O_2$ from air. The product of the reaction is $H_2O$. The operating temperature ranges between 150-200 °C. PAFCs are in commercial stage [13], however, it has low power density range and the catalyst is platinum (Pt) as catalyst, which increases considerably its cost [6].

Direct methanol fuel cells are fed with methanol ($CH_3OH$) in liquid or gaseous state at the anode and $O_2$ at the cathode. The electrolyte is a fluorinated or non-fluorinated polymeric composite membrane [14]. The membrane transports $H^+$ ions from the anode to the cathode, being the overall products of the reaction $CO_2$ at the anode and $H_2O$ at the cathode. The operating temperature ranges between 20-200 °C depending on the application. This type of cells has been highlighted as an ideal power source for portable electronic devices [15]. A greater success of DMFC relies on the possibility of increasing their power density, the lowest of all fuel cells, while at the same time overpassing fuel management, design (miniaturization), durability and cost issues [16].

Polymer Electrolyte Membrane Fuel Cells (PEMFC) are also called Proton Exchange Membrane Fuel Cells [17]. The anode is fed with $H_2$ and the membrane transports $H^+$ ions (protons) from the anode to the cathode. The cathode is fed with $O_2$, being the overall product of the reaction $H_2O$ at the cathode. This type of fuel cell can be further divided in two according to its operating temperature: low temperature PEMFC (for simplicity referred as PEMFC), up to 80 °C, and high temperature PEMFC

(HT-PEMFC); ranging between 120-200 °C [18]. The operating temperature dictates the chemical composition of the electrolyte. For PEMFC, polymeric composite membranes based on perfluorosulfonic acid (PFSA) are commonly used [19, 20] while for HT-PEMFC, the preferred electrolyte is based on polybenzimidazole (PBI) doped with $H_3PO_4$ [21].

It is important to highlight the different state of development between PEMFC and HT-PEMFC. Exemplarily, the higher operating temperature and characteristics of the electrolyte of HT-PEMFC make necessary the development of compatible components, accelerates components degradation and produces acid leaching [18]. Moreover, HT-PEMFC show slower start-up and shut-down capabilities than PEMFC.

PEMFC have the highest power density of all types of fuel cells and the widest range of applications (e.g. transportation, stationary and portable) among other interesting features. The interest and state of development of this type of fuel cell is such, that 87.2% of the worldwide fuel cells shipments were PEMFC, according to a survey of 2012 [22]. The main issue with PEMFC is that they are still not competitive in durability and cost, with exception of some niche market applications [23].

## 1.3. Low temperature polymer electrolyte membrane fuel cells (PEMFC)

As said before, this type of fuel cells have many interesting features which make them very attractive: quick start-up and shut-down capabilities, sustained operation at high current density, low weight, compactness, the potential for high volume manufacturing and long lifetime [24-27].

Despite the effort made to bring PEMFC to market, there are still two issues that limit the mass commercialization of this technology: i) the lack of a stable high purity $H_2$ supply infrastructure [28, 29] and ii) overpass fundamental research issues [30, 31] which involve interdisciplinary research and development (R&D) activities with governmental support, in order to increase their durability and reduce costs.

It is believed that a stable high purity $H_2$ supply is technically feasible and may even lead to what is known as "hydrogen economy", for which $H_2$ is the main energy vector [32, 33]. In turn, a better understanding of the operating parameters, with focus on their effect in the phenomena occurring at the electrodes, and the processes limiting its efficiency as well as the failure modes, causes and mechanisms of degradation, can help us to increase the durability and reduce their cost [34-37].

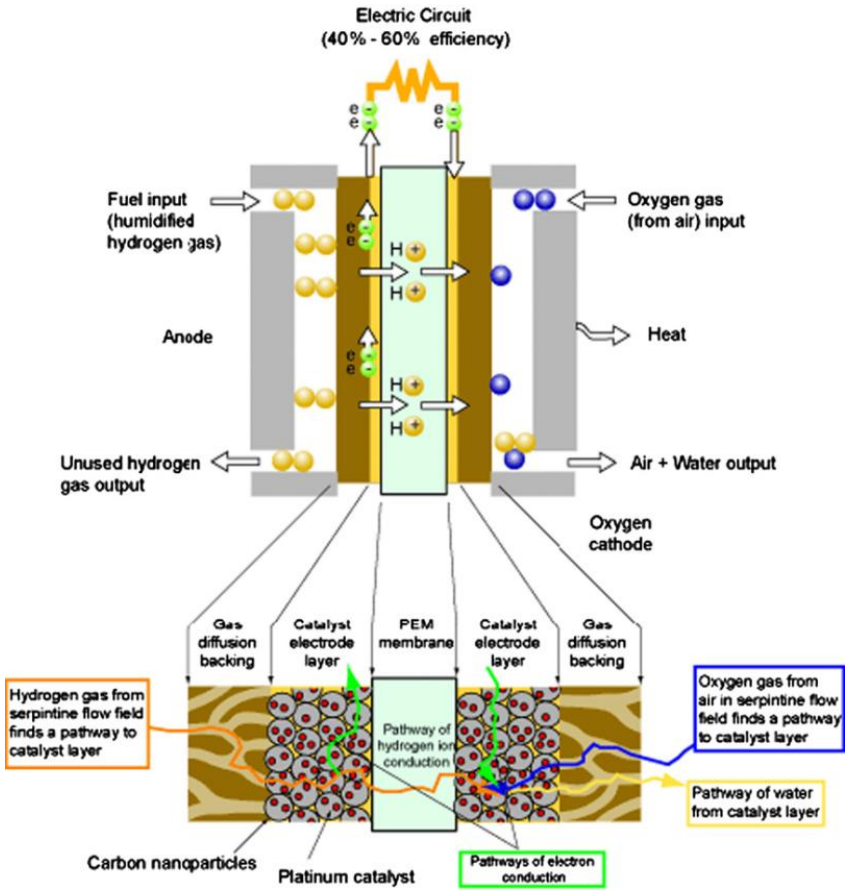


Figure 1.3. Detailed scheme of a PEMFC. Adapted from [30]

Figure 1.3 shows a detailed scheme of PEMFC. During operation, the hydrogen oxidation reaction (HOR) takes place at the anode (Equation 1) and the oxygen reduction reaction (ORR) at the cathode (Equation 2), generating $H_2O$ (Equation 3). For the HOR and ORR to occur, the electrolyte, the reactants and electrically connected catalyst regions must contact each other in what is called triple phase

boundary (TPB) [38]. The $H_2$ and $O_2$ are delivered to the gas diffusion backing (GDB), also called gas diffusion layer (GDL), using gas flow fields with serpentine-type geometry. The flow fields provide at the same time a path to remove the unused reactants and the $H_2O$. The main components of PEMFC are described in more detail below.

$$H_2 \rightarrow 2H^+ + 2e^- \quad (1)$$

$$\frac{1}{2}O_2 + 2H^+ + 2e^- \rightarrow H_2O \quad (2)$$

$$H_2 + \frac{1}{2}O_2 \rightarrow H_2O \quad (3)$$

### 1.3.1. Membrane

The core component of PEMFC is the membrane. If the membrane incorporates the catalyst, a membrane electrode assembly (MEA) is formed. Another alternative to this configuration is to deposit the catalyst on the GDL; nevertheless, the MEA configuration is preferred since the power density may be up to 18% higher [39].

The desired properties of a membrane suitable for PEMFC are: good chemical, mechanical and electrochemical stability, high proton conductivity and zero electronic conductivity, thermal and hydrolytic stability, chemically compatible with the electrode components, null permeability to reactants, high durability and low cost.

The chemical structure, physical properties, mass and proton transport phenomena of PFSA membranes have been summarized in several review papers and reference books [40-42] The chemical structure of Nafion® (Figure 1.4), which has served as base for developing other membranes, is based on a polytetrafluoroethylene (PTFE) backbone, sold as Teflon®. The PTFE is subjected to a sulphonation process in which a sulphonic acid ($-SO_3H$) side chain is added. The actual end of the chain is an $SO_3^-$ ion that attracts the $H^+$.

The most relevant physical properties of PFSA membranes are its conductivity (or resistivity), thickness, and ion exchange capacity (IEC). The proton conductivity of PFSA membranes affects the efficiency of the electrochemical reaction [43]. The thickness of the membrane influences the permeability of reactants [44] and ultimately the efficiency of PEMFC. The IEC of the membranes is related to the number of sulfonic sites which are susceptible to transport protons [45, 46]. The conductivity of PFSA membranes ranges between 0.0051-0.114 S $cm^{-1}$, the thickness between 5-254 µm and the IEC between 0.9-2.7 mol equivalent $g^{-1}$.

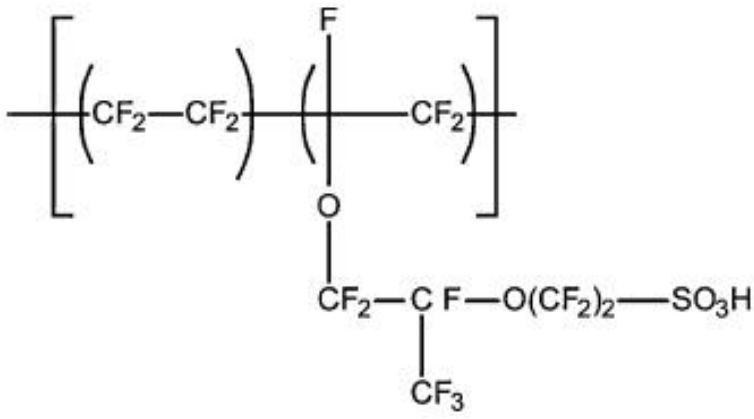


Figure 1.4. Basic structure of Nafion®.

Commercially available polymeric composite membranes based on PFSA include trade names as Gore® (W. L. Gore & Associates, Inc.), Flemion® (Asahi Glass Co., Ltd.), Aciplex® (Asahi Kasei Co., Ltd.), Fumapem® (Fuma-tech GmbH) and Greenerity® (SolviCore GmbH & Co. KG) and Nafion® (EI du Pont de Nemours & Co.) which is the most commonly used. The loss of proton conductivity when exposed to harsh operating conditions and the high cost of PFSA membranes is incentivizing the search for alternative membranes [20, 47].

### 1.3.2. Catalysts

The anode and cathode are catalytic films bonded to the membrane (in the MEA configuration). Due to their effectiveness to perform the HOR and ORR, unary Pt, binary Pt-M or ternary Pt-M-M, with M being a transition metal, are the catalysts of

choice [48, 49]; although the high cost of Pt [50] is motivating the search of alternatives [51, 52]. The catalysts are supported on carbon based or non-carbonaceous materials (i.e. titania, indium oxides, zirconia, silica, tungsten, etc.) since this structures show improved stability and higher activity compared to unsupported ones [53].

Conventional catalysts are based on Pt nanoparticles, 2-5 nm size, that are dispersed onto the support, 20 to 50 times larger [54]. The thickness of the catalytic film depends upon the amount of catalyst deposited on the membrane, which must be minimized to reduce costs. Moreover, the thickness must be kept below 10 μm otherwise the protons do not reach the catalytic film, that becomes inactive [55]. Other parameter related to the amount of catalyst deposited on the membrane is the catalyst loading, being this in the range of 0.05-0.4 mg Pt $cm^{-2}$.

The most important parameter determining the performance of PEMFC catalyst is the absolute ORR kinetic activity ($A \cdot cm^{-2}$), defined as the as the current density measured at 900mV under one atmosphere of fully saturated $O_2$ at 80 °C [54]. The absolute ORR kinetic activity is then useful to compare catalysts with regard to their area specific activity ($A \cdot cm^{-2}$ of Pt) and mass activity (A·mg of Pt).

The importance of the catalyst and catalyst support has led to extensive R&D in the field [56-58]. Recent breakthroughs in this field of research include, optimization of the molecular interactions between reactants and the catalyst surface by controlling the structure of the catalyst (i.e. using core-shell structures) [59], development of selective catalysts that suppress the undesired ORR at the anode side during startup and shutdown [60], use of iron-based catalyst to perform the ORR [61], development of PtNi alloys [54] or Pt monolayers on PdAu nanoparticles [62] in automotive PEMFC applications and the incorporation of grapheme as catalyst support [63].

### 1.3.3. Gas diffusion layer (GDL)

The main roles of an ideal GDL include: i) to diffuse effectively the reactants into the TPB, ii) to assist in the water management of the cell by allowing it to reach or removing it from the TPB and iii) to transport the electrons [64, 65].

The GDL is a carbon-based porous material manufactured in single layer or multiple layer configurations [55, 66]. Conventionally, the GDL consists of two layers, the first in contact with the electrode (microporous layer - MPL) and the second in contact with flow field (macroporous substrate - MPS) [67]. The MPL is a mixture of carbon black and PTFE, and its function is to reduce the electric contact resistance between the electrode and the MPS. The hydrophobic characteristics of the PTFE prevent the accumulation of water. In turn, the MPS provide mechanical strength, charge and mass transport capabilities to the MEA.

The most important characteristics of the GDL have been reviewed extensively [67, 68] and include: thickness, permeability, conductivity (or resistivity), porosity, and mass transport properties. The GDL characteristics are usually determined using ex-situ techniques [69, 70]. It is important to highlight that the GDL characteristics vary as a function of its compression, ultimately influencing the performance of PEMFC [71, 72]. Numerical studies report that compression of the GDL influences mainly the mass transport [68, 73], contact resistance [74] and heat transfer [75, 76] of PEMFC. The GDL thickness ranges between 150-360 μm, the permeability (Gurley) between 0.35-170 $cm^3\ cm^{-2}\ s^{-1}$ and the resistivity 6.7-14 $m\Omega\ cm^{-2}$.

Commercially available GDL include trade names such as Sigracet® (SGL Carbon SE, Germany), Pyrofil® (Mitsubishi Rayon Co. Ltd., Japan) and AvCarb® (AvCarb LLC, USA).

### 1.3.4. Bipolar plates (BP)

The BP are rigid and electrically conductive structures that incorporate the flow fields. Whenever two or more repetitive units, each formed by one MEA, one anode bipolar and one cathode bipolar plate, are electrically and hydraulically connected, a PEMFC stack is formed (Figure 1.5). Each repetitive unit is called a single or individual cell and they are usually connected in series in conventional stacks. The main functions of the BP are [77]: i) to distribute the reactants within the cells, ii) to facilitate the water management within the cells, iii) to collect the current from the cells, iv) to separate individual cells of the stack and v) to facilitate heat management of the stack.

The fundamental technical requirements of BP include: low cost, low pressure drop, high electrical conductivity (> 100 S $cm^{-1}$), low permeability to gases, suitability for high volume manufacturing, high mechanical strength, low weight, low volume and high chemical stability and corrosion resistance (< 16 µA $cm^{-2}$) [77]. Furthermore, it has been provided a guideline comprising 51 design requirements for BP of automotive stacks [79]. The numbers of requirements for BP have led to the development of different materials [80-82] and flow field designs [83-85].

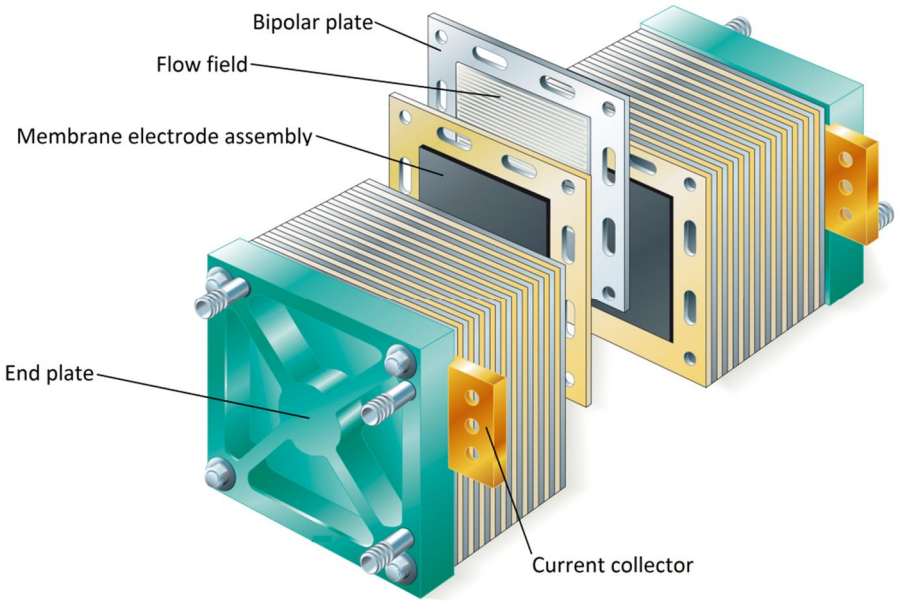


Figure 1.5. Main components of a PEMFC stack Adapted from [78].

It is noteworthy that different approaches have been proposed and categorized in order to prevent the leakage of reactants at the single cell level, namely: PEM direct sealing structure, PEM-wrapped frame sealing structure, MEA-wrapped frame sealing structure and rigid protective frame sealing structure [86].

## 1.4. Technological challenges of PEMFC

It is necessary to define target costs and performance parameters that would make PEMFC competitive with conventional technologies. The United States Department of Energy (DOE) has set different cost and performance targets for 2017 and identified the major challenges for the mass commercialization of PEMFC [87]: i)

target cost of \$30 $kW^{-1}$ for automotive and \$1,000–\$1,700 $kW^{-1}$ for stationary applications, ii) durability of 5,000 h (≈ 240,000 km) and 40-80 °C operating temperature for automotive and > 40,000 h of reliable operation between -35-40 °C for stationary applications v) the need of improved heat recovery systems that allow 80% efficiency in stationary combined heat and power (CHP) applications iv) system size comparable to that of current automotive technologies and iv) air, thermal and water management for both automotive and stationary applications; since ancillary equipments available (i.e. the balance of plant – BOP) are not optimized for fuel cell applications and the performance of the cell is very sensitive to small differences in operating conditions.

As of 2012, the cost and durability of PEMFC was \$47 $kW^{-1}$ and 2,500 h [87]. The latter highlights the big effort that is still needed to bring the benefits of the technology to society. Two key issues concerning the performance, reliability and durability of PEMFC are the water management and the effect of hydrogen impurities.

### 1.4.1. Water Management

The term water management refers to the study of the state of water (i.e. liquid or gas), its transport mechanisms within the cell and their implications on the performance and durability of PEMFC.

The water management issue becomes more sensitive at the MEA level since the proton conductivity of PFSA membranes is a function of its water activity [88]. The latter is explained since proton migration occurs in the ionomer hydrated phase after dissociation of the sulfonic acid groups [89]; which contrasts to a dry ionomer phase where the sulfonic acid groups are not dissociated, leading to a decrease in the conductivity of the membrane.

There is a paradoxical effect of water in PEMFC. On the one hand, the water content of the membrane needs to be maximized in order to achieve high proton conductivity during operation. On the other, if the water vapor saturation pressure is reached, the condensed water may hinder the paths for reactants distribution within

the cell. Whenever insufficient water is provided to the membrane and its proton conductivity decreases, “membrane drying” occurs. In turn, if delivery of reactants is limited by condensed water, “flooding” occurs. Interestingly, while membrane drying is limited to that component, flooding happens at the catalyst, the GDL and/or the flow fields [90].

It is important to know the parameters influencing the state of water and the water transport mechanisms to address the water management within the cell. The state of water within the cell is dictated by its saturation pressure, which is a function of the temperature [91]. The water transport mechanisms within the cell have been extensively studied both experimentally [92, 93] and numerically [94-96].

Figure 1.6 summarizes the water transport mechanisms in PEMFC. The electro-osmotic drag (EOD) is associated to the simultaneous transport of water molecules per each proton that migrates from the anode to the cathode due to electromotive forces crosswise the membrane [97]. The EOD coefficient is defined as the ratio of mole-of-water per mole-of-proton transported through the membrane in the absence of concentration and pressure gradient [43].

At microscopic level, the protons interact with the electrons of surrounding water molecules and form hydronium complexes ($H_mO_n^+$, with m = 3, 5 or 9 and n = 1, 2 or 4), an aggregate that consists of one or several water molecules and a proton [98]. Moreover, if the transport of hydronium complexes happens from high to low concentration regions (by diffusion) the vehicular mechanism of proton migration takes place [99]. In the same way, if the water content of the membrane is high enough to connect the polymer side chains, the protons may be directly transferred from one water molecule to another, indicating that the hopping or Grothuss mechanism of proton migration takes place [100].

The three other water transport mechanisms may be either well understood (diffusion), negligible under many conditions (hydraulic permeation) or not yet well understood (thermal-osmotic drag).

First, diffusion of water from the cathode to the anode, also referred to as “back diffusion”, is linked to the water concentration gradient created due to the generation of water at the cathode [43]. Second, hydraulic permeation occurs as a consequence of a pressure gradient between the electrodes [101-103]. The latter studies have shown that the hydraulic permeation is very low and that, added to concerns regarding the mechanical constrain imposed to the membrane in differentially pressurized electrodes, have not motivated deeper research on that type of water transport mechanism. Third, the thermal-osmotic drag was observed to be a result of the through-plane temperature gradient crosswise the membrane, which transports water towards the colder zone [104, 105]. It is believed that the heat-pipe effect, which occurs when water evaporation induces a water-vapor flux down the temperature gradient, is the responsible for the thermal-osmotic drag in PEMFC [106, 107]. However, more research is needed to fully understand the thermal osmotic drag and its implications in PEMFC [108].

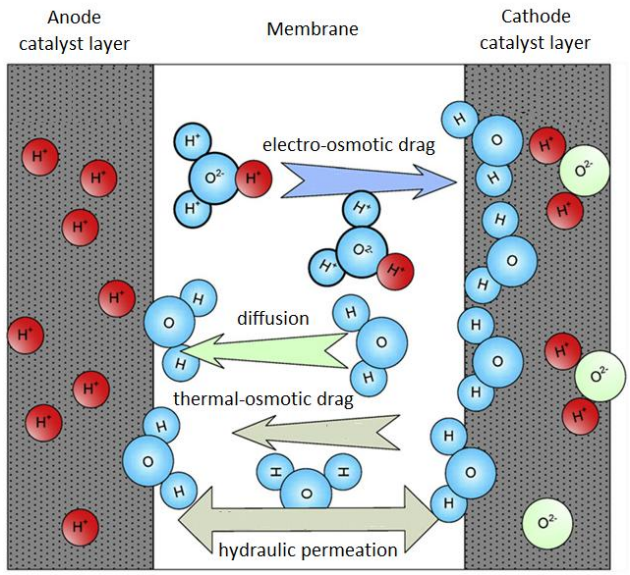


Figure 1.6. Water transport mechanisms in PEMFC. Adapted from [43].

It is observed that the spatial distribution of water not only determines the electrochemical performance of PEMFC but also affects strongly their durability. To operate the cell in dry conditions for short periods has immediate implications in the

electrochemical performance of PEMFC due to decreased conductivity of the membrane [109]. In turn, longer periods of dry operation cause irreversible damage to the membrane, which suffers mechanical degradation, becomes brittle and develops hot spots due to reactants crossover [110-113].

It is noteworthy that depending on the dominating water transport mechanism (Figure 1.6) flooding may appear at the anode and/or the cathode. Flooding causes what is called "reactants starvation" [114] and its short term implications include a decrease in the current or voltage [115]. The long term implications of reactants starvation due to flooding are many. $H_2$ starvation causes irreversible damage due to corrosion of the cathode catalyst support [116] and the dissolution and agglomeration of Pt into the membrane [117]. $O_2$ starvation has reported to be less critical than $H_2$ starvation [118], nevertheless it also results in permanent degradation due to dissolution and agglomeration of Pt into the membrane.

### 1.4.2. Effect of hydrogen impurities in PEMFC performance

Currently, $H_2$ is produced mainly from fossil fuels [119, 120] but also from water [121-124] and biomass [125-128]. The different feedstocks have led to the development of a broad suite of $H_2$ production technologies [129].

The type and amount of impurities depend strongly on the feedstock and the technology used for the production of $H_2$. If it is produced from $H_2O$ via electrolysis it may contain trace amounts (approx. 10 ppm) of $O_2$ and $H_2O$ [130]; not affecting the performance PEMFC. However, if $H_2$ is produced via gasification of coal or biomass, pyrolysis of biomass, steam reforming, auto thermal reforming or partial oxidation of different hydrocarbons, it will contain trace amounts (few to thousands of ppms) of CO [131-137]; affecting the performance of PEMFC.

CO has attracted most of the attention among other impurities such as carbon dioxide ($CO_2$), hydrogen sulfide ($H_2S$) and ammonia ($NH_3$) in the fuel. CO preferentially adsorbs onto the Pt and blocks the catalytic sites otherwise participating in the HOR (Equation 1) [138, 139]. The last process is called "CO

poisoning" and starts with a deeper understating of the HOR, which proceeds via the Tafel reaction [140] (Equation 4) followed by the Volmer reaction [141] (Equation 5):

$$H_2 + 2Pt \leftrightarrow 2Pt - H \quad (4)$$

$$2Pt - H \leftrightarrow 2Pt + 2H^+ + 2e^- \quad (5)$$

Then, with the presence of CO in the hydrogen, the impurity adsorbs onto the Pt according to [142]:

$$CO + Pt \leftrightarrow CO - Pt \quad (6)$$

Ultimately, the CO can be electrochemically or chemically oxidized and thus released from the Pt. Electrochemically oxidized within a potential range of 0.6-0.9 V, which is difficult to achieve in practice, via the "reactant pair mechanism" [141] (Equation 7). Chemically oxidized via a Langmuir-Hinshelwood mechanism [143] (Equations 8-10).

$$CO - Pt + H_2O \leftrightarrow Pt + CO_2 + 2H^+ \quad (7)$$

$$O_2 + 2Pt \leftrightarrow O_2 - Pt + Pt \rightarrow 2Pt - O \quad (8)$$

$$CO + Pt \leftrightarrow CO - Pt \quad (9)$$

$$CO - Pt + O - Pt \rightarrow CO_2 + 2Pt \quad (10)$$

Many factors influence the severity of CO poisoning in PEMFC: catalyst loading [144], catalyst structure and composition [145], operating temperature [146], CO concentration [147], membrane thickness and cathode backpressure [148], water vapor partial pressure [149], anode pressure [150] and potentiostatic or galvanostatic operation [151, 152].

CO decreases the performance, fuel and Pt utilization efficiency of PEMFC in the short term while in the long term reduces the electrochemically active area (ECA) of the anode [153].

## 1.5. Motivation and outline

This thesis was motivated by two major objectives: i) develop tools to evaluate the distributed performance of PEMFC with regard to water management and carbon monoxide poisoning and ii) study the dynamics of carbon monoxide poisoning under system-level relevant experimental conditions.

This thesis is divided in six Chapters. Chapter I is the Introduction; Chapter II is entitled, "Segmented PEMFC – A review"; Chapter III, "Water management studies"; Chapter IV, "Air bleed optimization studies"; Chapter V, "CO poisoning studies" and Chapter VI, "Conclusions and future work".

In Chapter II, a literature review on segmented Polymer Electrolyte Membrane Fuel Cells (SFC) is presented. The different approaches for the design, construction and electrochemical characterization of SFC are categorized. Recommendations for the design, construction and electrochemical characterization of SFC are given and the effect of different operating parameters on the current density distribution is analyzed. It is shown how other techniques such as gaseous species, water and temperature distribution can be coupled to SFC.

In Chapter III, an in-house designed and constructed test bench is built around a SFC operated in hydrogen recirculation mode. A technique for reducing the lateral current spreading in bipolar plates is presented. The local electrochemical activity of the cell is studied by performing current density distribution measurements. Complementarily, water balance analysis and mean gas velocity calculations are performed. The effect of hydrogen recirculation rate, anode pressure and purge cycle on the current density distribution is studied.

In Chapter IV, it is reported the design and construction of a new type of SFC suitable for studying the effect of impurities in PEMFC. The SFC is used to study the local effect of CO in PEMFC at relevant CO concentrations for PEMFC stationary applications. Moreover, $O_2$ is injected to the anode along with the fuel in order to oxidize the CO and the minimal amounts of $O_2$ needed to mitigate the effect of CO

are determined. The anode exhaust gas composition is measured using a gas chromatograph, facilitating the mass balance of CO. This work was performed at VTT – The Technical Research Centre of Finland.

In Chapter V, the effect of CO at relevant concentrations for PEMFC automotive applications is studied. The decrease in performance of the cell is tracked and the anode exhaust gas composition is continuously measured using a gas chromatograph. The effect of fuel utilization on the CO poisoning dynamics of PEMFC analyzed. This work was performed at VTT – The Technical Research Centre of Finland.

Finally, in Chapter VI the most representative findings of the thesis are summarized and research topics for the future are proposed.

## 1.6. References

[1] World Energy Outlook 2012, International Energy Agency.

[2] Haines, A., McMichael, A. J., Smith, K. R., Roberts, I., Woodcock, J., Markandya, A., Armstrong, B. G., Campbell-Lendrum, D., Dangour, A. D., Davies, M., Bruce, N., Tonne, C., Barrett, M., and Wilkinson, P., 2009, "Public health benefits of strategies to reduce greenhouse-gas emissions: overview and implications for policy makers," The Lancet, 374(9707), pp. 2104-2114.

[3] Tol, R. S. J., 2013, "Targets for global climate policy: An overview," Journal of Economic Dynamics and Control, 37(5), pp. 911-928.

[4] Lucia, U., 2013, "Carnot efficiency: Why?," Physica A: Statistical Mechanics and its Applications, 392(17), pp. 3513-3517.

[5] Andújar, J. M., and Segura, F., 2009, "Fuel cells: History and updating. A walk along two centuries," Renewable and Sustainable Energy Reviews, 13(9), pp. 2309-2322.

[6] Kirubakaran, A., Jain, S., and Nema, R. K., 2009, "A review on fuel cell technologies and power electronic interface," Renewable and Sustainable Energy Reviews, 13(9), pp. 2430-2440.

[7] Adams, T. A., Nease, J., Tucker, D., and Barton, P. I., 2012, "Energy Conversion with Solid Oxide Fuel Cell Systems: A Review of Concepts and Outlooks for the Short- and Long-Term," Industrial & Engineering Chemistry Research, 52(9), pp. 3089-3111.

[8] Brett, D. J. L., Atkinson, A., Brandon, N. P., and Skinner, S. J., 2008, "Intermediate temperature solid oxide fuel cells," Chemical Society Reviews, 37(8), pp. 1568-1578.

[9] Choudhury, A., Chandra, H., and Arora, A., 2013, "Application of solid oxide fuel cell technology for power generation—A review," Renewable and Sustainable Energy Reviews, 20(0), pp. 430-442.

[10] Kulkarni, A., and Giddey, S., 2012, "Materials issues and recent developments in molten carbonate fuel cells," Journal of Solid State Electrochemistry, 16(10), pp. 3123-3146.

[11] Bidault, F., Brett, D. J. L., Middleton, P. H., and Brandon, N. P., 2009, "Review of gas diffusion cathodes for alkaline fuel cells," Journal of Power Sources, 187(1), pp. 39-48.

[12] Tewari, A., Sambhy, V., Urquidi Macdonald, M., and Sen, A., 2006, "Quantification of carbon dioxide poisoning in air breathing alkaline fuel cells," Journal of Power Sources, 153(1), pp. 1-10.

[13] Mekhilef, S., Saidur, R., and Safari, A., 2012, "Comparative study of different fuel cell technologies," Renewable and Sustainable Energy Reviews, 16(1), pp. 981-989.

[14] Neburchilov, V., Martin, J., Wang, H. J., and Zhang, J. J., 2007, "A review of polymer electrolyte membranes for direct methanol fuel cells," Journal of Power Sources, 169(2), pp. 221-238.

[15] Rashidi, R., Dincer, I., Naterer, G. F., and Berg, P., 2009, "Performance evaluation of direct methanol fuel cells for portable applications," Journal of Power Sources, 187(2), pp. 509-516.

[16] Li, X., and Faghri, A., 2013, "Review and advances of direct methanol fuel cells (DMFCs) part I: Design, fabrication, and testing with high concentration methanol solutions," Journal of Power Sources, 226(0), pp. 223-240.

[17] Mench, M. M., 2008, Fuel Cell Engines, John Wiley & Sons, Inc., New Jersey.

[18] Chandan, A., Hattenberger, M., El-kharouf, A., Du, S., Dhir, A., Self, V., Pollet, B. G., Ingram, A., and Bujalski, W., 2013, "High temperature (HT) polymer electrolyte membrane fuel cells (PEMFC) – A review," Journal of Power Sources, 231(0), pp. 264-278.

[19] Jones, D. J., and Rozière, J., 2009, "FUEL CELLS – PROTON-EXCHANGE MEMBRANE FUEL CELLS | Membranes: Ambient Temperature," Encyclopedia of Electrochemical Power Sources, G. Editor-in-Chief: Jürgen, ed., Elsevier, Amsterdam, pp. 667-679.

[20] Yee, R. S. L., Rozendal, R. A., Zhang, K., and Ladewig, B. P., 2012, "Cost effective cation exchange membranes: A review," Chemical Engineering Research and Design, 90(7), pp. 950-959.

[21] Li, Q., He, R., Jensen, J. O., and Bjerrum, N. J., 2004, "PBI-Based Polymer Membranes for High Temperature Fuel Cells – Preparation, Characterization and Fuel Cell Demonstration," Fuel Cells, 4(3), pp. 147-159.

[22] "The Fuel Cell Today Industry Review 2012."

[23] Dicks, A. L., 2012, "4.08 - PEM Fuel Cells: Applications," Comprehensive Renewable Energy, S. Editor-in-Chief: Ali, ed., Elsevier, Oxford, pp. 203-245.

[24] Costamagna, P., and Srinivasan, S., 2001, "Quantum jumps in the PEMFC science and technology from the 1960s to the year 2000 Part I. Fundamental scientific aspects," Journal of Power Sources, 102(1-2), pp. 242-252.

[25] Costamagna, P., and Srinivasan, S., 2001, "Quantum jumps in the PEMFC science and technology from the 1960s to the year 2000: Part II. Engineering, technology

development and application aspects," Journal of Power Sources, 102(1–2), pp. 253-269.

[26] Gamburzev, S., and Appleby, A. J., 2002, "Recent progress in performance improvement of the proton exchange membrane fuel cell (PEMFC)," Journal of Power Sources, 107(1), pp. 5-12.

[27] Mehta, V., and Cooper, J. S., 2003, "Review and analysis of PEM fuel cell design and manufacturing," Journal of Power Sources, 114(1), pp. 32-53.

[28] Agnolucci, P., 2007, "Hydrogen infrastructure for the transport sector," International Journal of Hydrogen Energy, 32(15), pp. 3526-3544.

[29] Agnolucci, P., and McDowall, W., 2013, "Designing future hydrogen infrastructure: Insights from analysis at different spatial scales," International Journal of Hydrogen Energy, 38(13), pp. 5181-5191.

[30] Wang, Y., Chen, K. S., Mishler, J., Cho, S. C., and Adroher, X. C., 2011, "A review of polymer electrolyte membrane fuel cells: Technology, applications, and needs on fundamental research," Applied Energy, 88(4), pp. 981-1007.

[31] Behling, N., 2012, "Solving the fuel cell dilemma," Fuel Cells Bulletin, 2012(11), pp. 12-14.

[32] Dincer, I., and Zamfirescu, C., 2012, "Sustainable hydrogen production options and the role of IAHE," International Journal of Hydrogen Energy, 37(21), pp. 16266-16286.

[33] Mao, S. S., Shen, S., and Guo, L., 2012, "Nanomaterials for renewable hydrogen production, storage and utilization," Progress in Natural Science: Materials International, 22(6), pp. 522-534.

[34] Borup, R., Meyers, J., Pivovar, B., Kim, Y. S., Mukundan, R., Garland, N., Myers, D., Wilson, M., Garzon, F., Wood, D., Zelenay, P., More, K., Stroh, K., Zawodzinski, T., Boncella, J., McGrath, J. E., Inaba, M., Miyatake, K., Hori, M., Ota, K., Ogumi, Z., Miyata, S., Nishikata, A., Siroma, Z., Uchimoto, Y., Yasuda, K., Kimijima, K.-i., and Iwashita, N., 2007, "Scientific Aspects of Polymer Electrolyte Fuel Cell Durability and Degradation," Chemical Reviews, 107(10), pp. 3904-3951.

[35] Wu, J. F., Yuan, X. Z., Wang, H. J., Blanco, M., Martin, J. J., and Zhang, J. J., 2008, "Diagnostic tools in PEM fuel cell research: Part I - Electrochemical techniques," International Journal of Hydrogen Energy, 33(6), pp. 1735-1746.

[36] Schmittinger, W., and Vahidi, A., 2008, "A review of the main parameters influencing long-term performance and durability of PEM fuel cells," Journal of Power Sources, 180(1), pp. 1-14.

[37] Frank Bruijn, A., and Janssen, G. M., 2013, "PEM Fuel Cell Materials: Costs, Performance and Durability," Fuel Cells, K.-D. Kreuer, ed., Springer New York, pp. 249-303.

[38] O'Hayre, R., Barnett, D. M., and Prinz, F. B., 2005, "The Triple Phase Boundary: A Mathematical Model and Experimental Investigations for Fuel Cells," Journal of The Electrochemical Society, 152(2), pp. A439-A444.

[39] Liu, C.-Y., and Sung, C.-C., 2012, "A review of the performance and analysis of proton exchange membrane fuel cell membrane electrode assemblies," Journal of Power Sources, 220(0), pp. 348-353.

[40] Smitha, B., Sridhar, S., and Khan, A. A., 2005, "Solid polymer electrolyte membranes for fuel cell applications—a review," Journal of Membrane Science, 259(1–2), pp. 10-26.

[41] Mench, M. M., 2008, "Transport in Fuel Cell Systems," Fuel Cell Engines, John Wiley & Sons, Inc., pp. 191-284.

[42] Peighambardoust, S. J., Rowshanzamir, S., and Amjadi, M., 2010, "Review of the proton exchange membranes for fuel cell applications," International Journal of Hydrogen Energy, 35(17), pp. 9349-9384.

[43] Dai, W., Wang, H., Yuan, X.-Z., Martin, J. J., Yang, D., Qiao, J., and Ma, J., 2009, "A review on water balance in the membrane electrode assembly of proton exchange membrane fuel cells," International Journal of Hydrogen Energy, 34(23), pp. 9461-9478.

[44] Sakai, T., Takenaka, H., Wakabayashi, N., Kawami, Y., and Torikai, E., 1985, "Gas Permeation Properties of Solid Polymer Electrolyte (SPE) Membranes," Journal of The Electrochemical Society, 132(6), pp. 1328-1332.

[45] Navessin, T., Eikerling, M., Wang, Q., Song, D., Liu, Z., Horsfall, J., Lovell, K. V., and Holdcroft, S., 2005, "Influence of Membrane Ion Exchange Capacity on the Catalyst Layer Performance in an Operating PEM Fuel Cell," Journal of The Electrochemical Society, 152(4), pp. A796-A805.

[46] Pereira, F., Vallé, K., Belleville, P., Morin, A., Lambert, S., and Sanchez, C., 2008, "Advanced Mesostructured Hybrid Silica–Nafion Membranes for High-Performance PEM Fuel Cell," Chemistry of Materials, 20(5), pp. 1710-1718.

[47] Park, C. H., Lee, C. H., Guiver, M. D., and Lee, Y. M., 2011, "Sulfonated hydrocarbon membranes for medium-temperature and low-humidity proton exchange membrane fuel cells (PEMFCs)," Progress in Polymer Science, 36(11), pp. 1443-1498.

[48] Chuan-Jian Zhong and Jin Luo and Bin Fang and Bridgid, N. W. a. P. N. N. a. R. L. a. J. Y., 2010, "Nanostructured catalysts in fuel cells," Nanotechnology, 21(6), p. 062001.

[49] Seo, A., Lee, J., Han, K., and Kim, H., 2006, "Performance and stability of Pt-based ternary alloy catalysts for PEMFC," Electrochimica Acta, 52(4), pp. 1603-1611.

[50] Sun, Y., Delucchi, M., and Ogden, J., 2011, "The impact of widespread deployment of fuel cell vehicles on platinum demand and price," International Journal of Hydrogen Energy, 36(17), pp. 11116-11127.

[51] Chen, Z., Higgins, D., Yu, A., Zhang, L., and Zhang, J., 2011, "A review on non-precious metal electrocatalysts for PEM fuel cells," Energy & Environmental Science, 4(9), pp. 3167-3192.

[52] Brouzgou, A., Song, S. Q., and Tsiakaras, P., 2012, "Low and non-platinum electrocatalysts for PEMFCs: Current status, challenges and prospects," Applied Catalysis B: Environmental, 127(0), pp. 371-388.

[53] Sharma, S., and Pollet, B. G., 2012, "Support materials for PEMFC and DMFC electrocatalysts—A review," Journal of Power Sources, 208(0), pp. 96-119.

[54] Debe, M. K., 2012, "Electrocatalyst approaches and challenges for automotive fuel cells," Nature, 486(7401), pp. 43-51.

[55] Litster, S., and McLean, G., 2004, "PEM fuel cell electrodes," Journal of Power Sources, 130(1-2), pp. 61-76.

[56] Markovic, N. M., and Ross, P. N., 2002, "Surface science studies of model fuel cell electrocatalysts," Surface Science Reports, 45(4-6), pp. 121-229.

[57] Zhong Cj Fau - Luo, J., Luo J Fau - Fang, B., Fang B Fau - Wanjala, B. N., Wanjala Bn Fau - Njoki, P. N., Njoki Pn Fau - Loukrakpam, R., Loukrakpam R Fau - Yin, J., and Yin, J., "Nanostructured catalysts in fuel cells," (1361-6528 (Electronic)).

[58] Yu, X., Yuan, J., and Sundén, B., 2011, "Review on the Properties of Nano-/Microstructures in the Catalyst Layer of PEMFC," Journal of Fuel Cell Science and Technology, 8(3), pp. 034001-034001.

[59] Strasser, P., Koh, S., Anniyev, T., Greeley, J., More, K., Yu, C., Liu, Z., Kaya, S., Nordlund, D., Ogasawara, H., Toney, M. F., and Nilsson, A., 2010, "Lattice-strain control of the activity in dealloyed core–shell fuel cell catalysts," Nat Chem, 2(6), pp. 454-460.

[60] Genorio, B., Strmcnik, D., Subbaraman, R., Tripkovic, D., Karapetrov, G., Stamenkovic, V. R., Pejovnik, S., and Marković, N. M., 2010, "Selective catalysts for

the hydrogen oxidation and oxygen reduction reactions by patterning of platinum with calix[4]arene molecules," Nat Mater, 9(12), pp. 998-1003.

[61] Proietti, E., Jaouen, F., Lefèvre, M., Larouche, N., Tian, J., Herranz, J., and Dodelet, J.-P., 2011, "Iron-based cathode catalyst with enhanced power density in polymer electrolyte membrane fuel cells," Nat Commun, 2, p. 416.

[62] Sasaki, K., Naohara, H., Choi, Y., Cai, Y., Chen, W.-F., Liu, P., and Adzic, R. R., 2012, "Highly stable Pt monolayer on PdAu nanoparticle electrocatalysts for the oxygen reduction reaction," Nat Commun, 3, p. 1115.

[63] Sun, S., Zhang, G., Gauquelin, N., Chen, N., Zhou, J., Yang, S., Chen, W., Meng, X., Geng, D., Banis, M. N., Li, R., Ye, S., Knights, S., Botton, G. A., Sham, T.-K., and Sun, X., 2013, "Single-atom Catalysis Using Pt/Graphene Achieved through Atomic Layer Deposition," Sci. Rep., 3.

[64] Jordan, L. R., Shukla, A. K., Behrsing, T., Avery, N. R., Muddle, B. C., and Forsyth, M., 2000, "Diffusion layer parameters influencing optimal fuel cell performance," Journal of Power Sources, 86(1–2), pp. 250-254.

[65] Meng, H., and Wang, C.-Y., 2004, "Electron Transport in PEFCs," Journal of The Electrochemical Society, 151(3), pp. A358-A367.

[66] Park, S., Lee, J.-W., and Popov, B. N., 2012, "A review of gas diffusion layer in PEM fuel cells: Materials and designs," International Journal of Hydrogen Energy, 37(7), pp. 5850-5865.

[67] Cindrella, L., Kannan, A. M., Lin, J. F., Saminathan, K., Ho, Y., Lin, C. W., and Wertz, J., 2009, "Gas diffusion layer for proton exchange membrane fuel cells--A review," Journal of Power Sources, 194(1), pp. 146-160.

[68] Jang, J.-H., Yan, W.-M., and Shih, C.-C., 2006, "Effects of the gas diffusion-layer parameters on cell performance of PEM fuel cells," Journal of Power Sources, 161(1), pp. 323-332.

[69] Lee, H.-K., Park, J.-H., Kim, D.-Y., and Lee, T.-H., 2004, "A study on the characteristics of the diffusion layer thickness and porosity of the PEMFC," Journal of Power Sources, 131(1–2), pp. 200-206.

[70] Parikh, N., Allen, J. S., and Yassar, R. S., 2012, "Microstructure of Gas Diffusion Layers for PEM Fuel Cells," Fuel Cells, 12(3), pp. 382-390.

[71] Lee, W. K., Ho, C. H., Van Zee, J. W., and Murthy, M., 1999, "The effects of compression and gas diffusion layers on the performance of a PEM fuel cell," Journal of Power Sources, 84(1), pp. 45-51.

[72] Ge, J., Higier, A., and Liu, H., 2006, "Effect of gas diffusion layer compression on PEM fuel cell performance," Journal of Power Sources, 159(2), pp. 922-927.

[73] Shi, Z., Wang, X., and Guessous, L., 2010, "Effect of Compression on the Water Management of a Proton Exchange Membrane Fuel Cell With Different Gas Diffusion Layers," Journal of Fuel Cell Science and Technology, 7(2), pp. 021012-021012.

[74] Zhou, Y., Lin, G., Shih, A. J., and Hu, S. J., 2007, "A micro-scale model for predicting contact resistance between bipolar plate and gas diffusion layer in PEM fuel cells," Journal of Power Sources, 163(2), pp. 777-783.

[75] Hottinen, T., and Himanen, O., 2007, "PEMFC temperature distribution caused by inhomogeneous compression of GDL," Electrochemistry Communications, 9(5), pp. 1047-1052.

[76] Ahmed, D. H., Sung, H. J., and Bae, J., 2008, "Effect of GDL permeability on water and thermal management in PEMFCs—II. Clamping force," International Journal of Hydrogen Energy, 33(14), pp. 3786-3800.

[77] Hermann, A., Chaudhuri, T., and Spagnol, P., 2005, "Bipolar plates for PEM fuel cells: A review," International Journal of Hydrogen Energy, 30(12), pp. 1297-1302.

[78]http://www.theengineer.co.uk/in-depth/stack-assembly/292670.article, retrieved on July 2013.

[79] Cooper, J. S., 2004, "Design analysis of PEMFC bipolar plates considering stack manufacturing and environment impact," Journal of Power Sources, 129(2), pp. 152-169.

[80] de las Heras, N., Roberts, E. P. L., Langton, R., and R. Hodgson, D., 2009, "A review of metal separator plate materials suitable for automotive PEM fuel cells," Energy & Environmental Science, 2(2), pp. 206-214.

[81] Wang, H., and Turner, J. A., 2010, "Reviewing Metallic PEMFC Bipolar Plates," Fuel Cells, 10(4), pp. 510-519.

[82] Boyaci San, F. G., and Tekin, G., 2013, "A review of thermoplastic composites for bipolar plate applications," International Journal of Energy Research, 37(4), pp. 283-309.

[83] Li, X., and Sabir, I., 2005, "Review of bipolar plates in PEM fuel cells: Flow-field designs," International Journal of Hydrogen Energy, 30(4), pp. 359-371.

[84] Aiyejina, A., and Sastry, M. K. S., 2011, "PEMFC Flow Channel Geometry Optimization: A Review," Journal of Fuel Cell Science and Technology, 9(1), pp. 011011-011011.

[85] Arvay, A., French, J., Wang, J. C., Peng, X. H., and Kannan, A. M., 2013, "Nature inspired flow field designs for proton exchange membrane fuel cell," International Journal of Hydrogen Energy, 38(9), pp. 3717-3726.

[86] Ye, D.-h., and Zhan, Z.-g., 2013, "A review on the sealing structures of membrane electrode assembly of proton exchange membrane fuel cells," Journal of Power Sources, 231(0), pp. 285-292.

[87]http://www1.eere.energy.gov/hydrogenandfuelcells/fuelcells/fc_challenges.html , retrieved on July 2013."

[88] Carnes, B., and Djilali, N., 2006, "Analysis of coupled proton and water transport in a PEM fuel cell using the binary friction membrane model," Electrochimica Acta, 52(3), pp. 1038-1052.

[89] Deabate, S., Gebel, G., Huguet, P., Morin, A., and Pourcelly, G., 2012, "3 In situ and operando determination of the water content distribution in proton conducting membranes for fuel cells: a critical review," Energy & Environmental Science, 5(10), pp. 8824-8847.

[90] Li, H., Tang, Y., Wang, Z., Shi, Z., Wu, S., Song, D., Zhang, J., Fatih, K., Zhang, J., Wang, H., Liu, Z., Abouatallah, R., and Mazza, A., 2008, "A review of water flooding issues in the proton exchange membrane fuel cell," Journal of Power Sources, 178(1), pp. 103-117.

[91] Wagner, W., and Pruss, A., 2002, "The IAPWS Formulation 1995 for the Thermodynamic Properties of Ordinary Water Substance for General and Scientific Use," Journal of Physical and Chemical Reference Data, 31(2), pp. 387-535.

[92] Bazylak, A., 2009, "Liquid water visualization in PEM fuel cells: A review," International Journal of Hydrogen Energy, 34(9), pp. 3845-3857.

[93] Tsushima, S., and Hirai, S., 2011, "In situ diagnostics for water transport in proton exchange membrane fuel cells," Progress in Energy and Combustion Science, 37(2), pp. 204-220.

[94] Fimrite, J., Struchtrup, H., and Djilali, N., 2005, "Transport Phenomena in Polymer Electrolyte Membranes: I. Modeling Framework," Journal of The Electrochemical Society, 152(9), pp. A1804-A1814.

[95] Wu, H., Li, X., and Berg, P., 2009, "On the modeling of water transport in polymer electrolyte membrane fuel cells," Electrochimica Acta, 54(27), pp. 6913-6927.

[96] Nasef, M. M., and Aly, A. A., 2012, "Water and charge transport models in proton exchange membranes: An overview," Desalination, 287(0), pp. 238-246.

[97] Jiao, K., and Li, X., 2011, "Water transport in polymer electrolyte membrane fuel cells," Progress in Energy and Combustion Science, 37(3), pp. 221-291.

[98] Pivovar, B. S., and Kim, Y. S., 2007, "The membrane-electrode interface in PEFCs," Journal of the Electrochemical Society, 154(8), pp. B739-B744.

[99] Kreuer, K.-D., Rabenau, A., and Weppner, W., 1982, "Vehicle Mechanism, A New Model for the Interpretation of the Conductivity of Fast Proton Conductors," Angewandte Chemie International Edition in English, 21(3), pp. 208-209.

[100] Agmon, N., 1995, "The Grotthuss mechanism," Chemical Physics Letters, 244(5–6), pp. 456-462.

[101] Husar, A., Higier, A., and Liu, H., 2008, "In situ measurements of water transfer due to different mechanisms in a proton exchange membrane fuel cell," Journal of Power Sources, 183(1), pp. 240-246.

[102] Büchi, F. N., Wakizoe, M., and Srinivasan, S., 1996, "Microelectrode Investigation of Oxygen Permeation in Perfluorinated Proton Exchange Membranes with Different Equivalent Weights," Journal of The Electrochemical Society, 143(3), pp. 927-932.

[103] Bernardi, D. M., and Verbrugge, M. W., 1992, "A Mathematical Model of the Solid-Polymer-Electrolyte Fuel Cell," Journal of The Electrochemical Society, 139(9), pp. 2477-2491.

[104] Kim, S., and Mench, M. M., 2009, "Investigation of temperature-driven water transport in polymer electrolyte fuel cell: Thermo-osmosis in membranes," Journal of Membrane Science, 328(1–2), pp. 113-120.

[105] Zaffou, R., Yi, J. S., Kunz, H. R., and Fenton, J. M., 2006, "Temperature-Driven Water Transport Through Membrane Electrode Assembly of Proton Exchange Membrane Fuel Cells," Electrochemical and Solid-State Letters, 9(9), pp. A418-A422.

[106] Weber, A. Z., and Newman, J., 2006, "Coupled Thermal and Water Management in Polymer Electrolyte Fuel Cells," Journal of The Electrochemical Society, 153(12), pp. A2205-A2214.

[107] Weber, A. Z., and Hickner, M. A., 2008, "Modeling and high-resolution-imaging studies of water-content profiles in a polymer-electrolyte-fuel-cell membrane-electrode assembly," Electrochimica Acta, 53(26), pp. 7668-7674.

[108] Khandelwal, M., Lee, S., and Mench, M. M., 2009, "Model to Predict Temperature and Capillary Pressure Driven Water Transport in PEFCs After Shutdown," Journal of The Electrochemical Society, 156(6), pp. B703-B715.

[109] Kang, J., and Kim, J., 2010, "Membrane electrode assembly degradation by dry/wet gas on a PEM fuel cell," International Journal of Hydrogen Energy, 35(23), pp. 13125-13130.

[110] Huang, X., Solasi, R., Zou, Y., Feshler, M., Reifsnider, K., Condit, D., Burlatsky, S., and Madden, T., 2006, "Mechanical endurance of polymer electrolyte membrane and PEM fuel cell durability," Journal of Polymer Science Part B: Polymer Physics, 44(16), pp. 2346-2357.

[111] Kusoglu, A., Karlsson, A. M., Santare, M. H., Cleghorn, S., and Johnson, W. B., 2007, "Mechanical behavior of fuel cell membranes under humidity cycles and effect of swelling anisotropy on the fatigue stresses," Journal of Power Sources, 170(2), pp. 345-358.

[112] Chen, C., and Fuller, T. F., 2009, "The effect of humidity on the degradation of Nafion® membrane," Polymer Degradation and Stability, 94(9), pp. 1436-1447.

[113] Sethuraman, V. A., Weidner, J. W., Haug, A. T., and Protsailo, L. V., 2008, "Durability of Perfluorosulfonic Acid and Hydrocarbon Membranes: Effect of Humidity and Temperature," Journal of The Electrochemical Society, 155(2), pp. B119-B124.

[114] Yousfi-Steiner, N., Moçotéguy, P., Candusso, D., and Hissel, D., 2009, "A review on polymer electrolyte membrane fuel cell catalyst degradation and starvation issues: Causes, consequences and diagnostic for mitigation," Journal of Power Sources, 194(1), pp. 130-145.

[115] Thounthong, P., Davat, B., Rael, S., and Sethakul, P., 2009, "Fuel starvation," Industry Applications Magazine, IEEE, 15(4), pp. 52-59.

[116] Kang, J., Jung, D. W., Park, S., Lee, J.-H., Ko, J., and Kim, J., 2010, "Accelerated test analysis of reversal potential caused by fuel starvation during PEMFCs operation," International Journal of Hydrogen Energy, 35(8), pp. 3727-3735.

[117] Kim, L., Chung, C. G., Sung, Y. W., and Chung, J. S., 2008, "Dissolution and migration of platinum after long-term operation of a polymer electrolyte fuel cell under various conditions," Journal of Power Sources, 183(2), pp. 524-532.

[118] Taniguchi, A., Akita, T., Yasuda, K., and Miyazaki, Y., 2008, "Analysis of degradation in PEMFC caused by cell reversal during air starvation," International Journal of Hydrogen Energy, 33(9), pp. 2323-2329.

[119] Ahmed, S., Aitani, A., Rahman, F., Al-Dawood, A., and Al-Muhaish, F., 2009, "Decomposition of hydrocarbons to hydrogen and carbon," Applied Catalysis A: General, 359(1–2), pp. 1-24.

[120] Abbas, H. F., and Wan Daud, W. M. A., 2010, "Hydrogen production by methane decomposition: A review," International Journal of Hydrogen Energy, 35(3), pp. 1160-1190.

[121] Currao, A., 2007, "Photoelectrochemical Water Splitting," CHIMIA International Journal for Chemistry, 61(12), pp. 815-819.

[122] Rosen, M. A., 2010, "Advances in hydrogen production by thermochemical water decomposition: A review," Energy, 35(2), pp. 1068-1076.

[123] Laguna-Bercero, M. A., 2012, "Recent advances in high temperature electrolysis using solid oxide fuel cells: A review," Journal of Power Sources, 203(0), pp. 4-16.

[124] Aricò, A. S., Siracusano, S., Briguglio, N., Baglio, V., Blasi, A., and Antonucci, V., 2013, "Polymer electrolyte membrane water electrolysis: status of technologies and potential applications in combination with renewable power sources," Journal of Applied Electrochemistry, 43(2), pp. 107-118.

[125] Tanksale, A., Beltramini, J. N., and Lu, G. M., 2010, "A review of catalytic hydrogen production processes from biomass," Renewable and Sustainable Energy Reviews, 14(1), pp. 166-182.

[126] Levin, D. B., and Chahine, R., 2010, "Challenges for renewable hydrogen production from biomass," International Journal of Hydrogen Energy, 35(10), pp. 4962-4969.

[127] Kruse, O., and Hankamer, B., 2010, "Microalgal hydrogen production," Current Opinion in Biotechnology, 21(3), pp. 238-243.

[128] Keskin, T., Abo-Hashesh, M., and Hallenbeck, P. C., 2011, "Photofermentative hydrogen production from wastes," Bioresource Technology, 102(18), pp. 8557-8568.

[129] Holladay, J. D., Hu, J., King, D. L., and Wang, Y., 2009, "An overview of hydrogen production technologies," Catalysis Today, 139(4), pp. 244-260.

[130] Ursua, A., Gandia, L. M., and Sanchis, P., 2012, "Hydrogen Production From Water Electrolysis: Current Status and Future Trends," Proceedings of the Ieee, 100(2), pp. 410-426.

[131] Onozaki, M., Watanabe, K., Hashimoto, T., Saegusa, H., and Katayama, Y., 2006, "Hydrogen production by the partial oxidation and steam reforming of tar from hot coke oven gas," Fuel, 85(2), pp. 143-149.

[132] Galvita, V., Schröder, T., Munder, B., and Sundmacher, K., 2008, "Production of hydrogen with low COx-content for PEM fuel cells by cyclic water gas shift reactor," International Journal of Hydrogen Energy, 33(4), pp. 1354-1360.

[133] Besancon, B. M., Hasanov, V., Imbault-Lastapis, R., Benesch, R., Barrio, M., and Mølnvik, M. J., 2009, "Hydrogen quality from decarbonized fossil fuels to fuel cells," International Journal of Hydrogen Energy, 34(5), pp. 2350-2360.

[134] Mendes, D., Tosti, S., Borgognoni, F., Mendes, A., and Madeira, L. M., 2010, "Integrated analysis of a membrane-based process for hydrogen production from ethanol steam reforming," Catalysis Today, 156(3–4), pp. 107-117.

[135] Jang, J.-Y., Huang, Y.-X., and Cheng, C.-H., 2010, "The effects of geometric and operating conditions on the hydrogen production performance of a micro-methanol steam reformer," Chemical Engineering Science, 65(20), pp. 5495-5506.

[136] Song, T., Wu, J., Shen, L., and Xiao, J., 2012, "Experimental investigation on hydrogen production from biomass gasification in interconnected fluidized beds," Biomass and Bioenergy, 36(0), pp. 258-267.

[137] Muradov, N., 2003, "Emission-free fuel reformers for mobile and portable fuel cell applications," Journal of Power Sources, 118(1–2), pp. 320-324.

[138] Zamel, N., and Li, X., 2011, "Effect of contaminants on polymer electrolyte membrane fuel cells," Progress in Energy and Combustion Science, 37(3), pp. 292-329.

[139] Cheng, X., Shi, Z., Glass, N., Zhang, L., Zhang, J. J., Song, D. T., Liu, Z. S., Wang, H. J., and Shen, J., 2007, "A review of PEM hydrogen fuel cell contamination: Impacts, mechanisms, and mitigation," Journal of Power Sources, 165(2), pp. 739-756.

[140] Stonehart, P., and Ross, P. N., 1975, "The Commonality of Surface Processes in Electrocatalysis and Gas-Phase Heterogeneous Catalysis," Catalysis Reviews, 12(1), pp. 1-35.

[141] Gilman, S., 1964, "The Mechanism of Electrochemical Oxidation of Carbon Monoxide and Methanol on Platinum. II. The “Reactant-Pair” Mechanism for Electrochemical Oxidation of Carbon Monoxide and Methanol1," The Journal of Physical Chemistry, 68(1), pp. 70-80.

[142] Vogel, W., Lundquist, L., Ross, P., and Stonehart, P., 1975, "Reaction pathways and poisons—II: The rate controlling step for electrochemical oxidation of hydrogen on Pt in acid and poisoning of the reaction by CO," Electrochimica Acta, 20(1), pp. 79-93.

[143] Santra, A. K., and Goodman, D. W., 2002, "Catalytic oxidation of CO by platinum group metals: from ultrahigh vacuum to elevated pressures," Electrochimica Acta, 47(22–23), pp. 3595-3609.

[144] Hashimasa, Y., Matsuda, Y., and Akai, M., 2010, "Effects of Platinum Loading on PEFC Power Generation Performance Deterioration by Carbon Monoxide in Hydrogen Fuel," ECS Transactions, 26(1), pp. 131-142.

[145] Ehteshami, S. M. M., and Chan, S. H., 2013, "A review of electrocatalysts with enhanced CO tolerance and stability for polymer electrolyte membarane fuel cells," Electrochimica Acta, 93(0), pp. 334-345.

[146] Angelo, M., St-Pierre, J., Bethune, K., and Rocheleau, R., 2011, "Gas Chromatography Study of Reactions of Carbon Monoxide at Different Operating Temperatures within a PEMFC," ECS Transactions, 35(32), pp. 167-178.

[147] Jiménez, S., Soler, J., Valenzuela, R. X., and Daza, L., 2005, "Assessment of the performance of a PEMFC in the presence of CO," Journal of Power Sources, 151(0), pp. 69-73.

[148] Wang, W., 2009, "The effect of internal air bleed on CO poisoning in a proton exchange membrane fuel cell," Journal of Power Sources, 191(2), pp. 400-406.

[149] Zhang, J. Z., Hongsirikarn, K., and Goodwin Jr, J. G., 2011, "The effect of low concentrations of CO on H2 adsorption and activation on Pt/C: Part 2—In the presence of H2O vapor," Journal of Power Sources, 196(15), pp. 6186-6195.

[150] Murthy, M., Esayian, M., Lee, W.-k., and Zee, J. W. V., 2003, "The Effect of Temperature and Pressure on the Performance of a PEMFC Exposed to Transient CO Concentrations," Journal of the Electrochemical Society, 150(1), pp. A29-A34.

[151] Tingelöf, T., Hedström, L., Holmström, N., Alvfors, P., and Lindbergh, G., 2008, "The influence of CO2, CO and air bleed on the current distribution of a polymer electrolyte fuel cell," International Journal of Hydrogen Energy, 33(8), pp. 2064-2072.

[152] Chung, C.-C., Chen, C.-H., and Weng, D.-Z., 2009, "Development of an air bleeding technique and specific duration to improve the CO tolerance of proton-exchange membrane fuel cells," Applied Thermal Engineering, 29(11–12), pp. 2518-2526.

[153] Angelo, M., Bethune, K., and Rocheleau, R., 2010, "The Impact of sub ppm Carbon Monoxide and ppm Level CO/Toluene and Methylcyclohexane/CO Mixtures on PEMFC Performance and Durability," ECS Transactions, 28(23), pp. 169-181.

# Chapter II

# Chapter 2 - Segmented PEMFC - A review[1]

## 2.1. Abstract

A complex interaction of many design, assembling and operating parameters as well as the properties of the materials used in the construction of polymer electrolyte membrane fuel cells (PEMFC) result in an uneven electrochemical performance over the MEA active area. For more than one decade, segmented PEMFC (SFC) have been used to study the factors responsible for that uneven performance. This paper reviews relevant literature related to SFC published since 1998 focusing on the three most important SFC design techniques: (1) printed circuit board, (2) resistors network and (3) Hall effect sensors. First, the three techniques are described and fundamental considerations for its design, construction and electrochemical characterization are provided. After that, the effect of most important parameters on the current density distribution is highlighted. Finally, representative results combining current density distribution measurements with other analytical techniques for spatial analysis are presented.

[1] The content of this chapter is adapted from: Pérez, L. C., Brandão, L., Sousa, J. M., and Mendes, A., 2011, "Segmented polymer electrolyte membrane fuel cells - A review," Renewable and Sustainable Energy Reviews, 15(1), pp. 169-185.

## 2.2. Introduction

In order to accelerate the sluggish transition from R&D to full scale commercialization of polymer electrolyte membrane fuel cells (PEMFC) [1], efforts are still focused in overpassing delicate issues related to the hydrogen production and storage [2,3] and the development of hydrogen delivery infrastructure [4]. In the same way, recent publications highlight the need of cost reduction and further understanding of PEMFC systems regarding their degradation mechanisms and durability, water and thermal management, bipolar plates design and materials, catalyst load reduction and CO tolerance as well as the materials of the membrane-electrode assembly MEA [5,6,7]. To further understand PEMFC systems, a detailed analysis of the influence of main parameters on its performance and the development and combination of different *in-situ* analytical methods is fundamental.

On the one hand, it is relatively well documented that PEMFC performance is affected by a complex interaction of many design, assembling and operating parameters as well as by the properties and microstructure of materials used on their construction. Design and assembling parameters include: i) flow field geometry and ii) clamping pressure. Operating parameters include: i) species relative humidity, partial pressure and flow rate, ii) temperature and iii) total pressure. Finally, issues related to materials include: i) properties and ii) microstructure of materials, mainly at the MEA level. On the other hand, it has been pointed out by several authors that the most important implication of this complex interaction is an uneven electrochemical response of the MEA active area, the same that may lead to low reactants and electrocatalyst utilization, reducing the overall efficiency and accelerating aging [8, 9, 10, 11].

In the last decade, segmented PEMFC (SFC) have proven to be an excellent *in situ* diagnostic tool to study the factors responsible for the uneven electrochemical response of the MEA active area. A SFC is similar to an ordinary fuel cell with the exception that one of the electrodes is divided into smaller electrodes, each of which can be interrogated for current, voltage and resistance, independently of the others

[12]. In this work, the SFC definition embraces the PEMFC that permit the study of electrochemical phenomena (e.g. current, voltage or impedance) and/or monitoring different parameters (e.g. gaseous species composition, water accumulation or temperature) at a specific location of the MEA (a segment) so that a distributed performance analysis can be performed.

Segmentation of a PEMFC involves accurate division of pertinent PEMFC components, namely the current collectors (CC), the bipolar plates (BP) or the gas diffusion layers (GDL). The distributed analysis and/or monitoring of different parameters is achieved with the individual characterization of the segments. Concerning the use of segmented and non-segmented PEMFC components, the different approaches proposed for SFC design, construction and electrochemical characterization can be divided in invasive, sub-divided in three main categories, and non-invasive. The SFC classification adopted in this work is schematically shown in Figure 2.1.

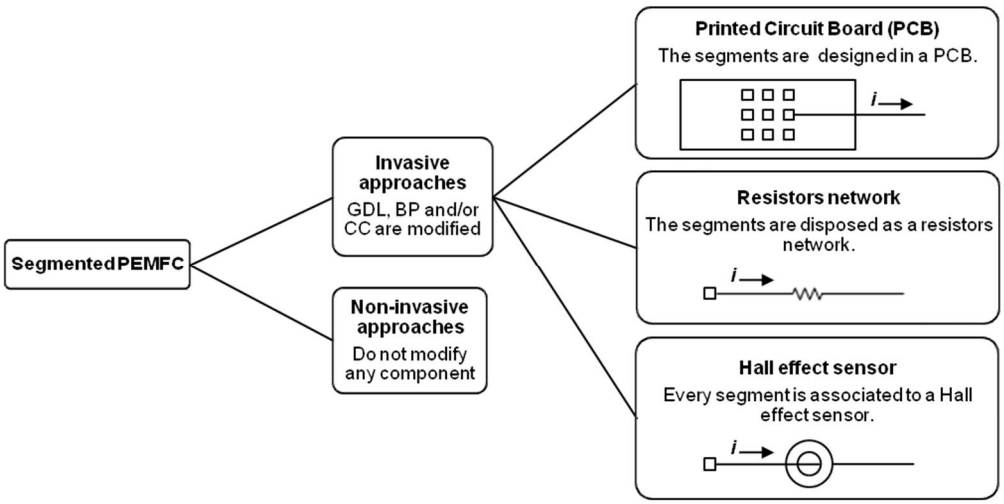


Figure 2.1. Main approaches used for design, construction and electrochemical characterization of SFC.

To the date, very few reviews described how SFC are used to perform discrete *in situ* electrochemical analysis [13] and physico-chemical characterization [14]. Yuan *et al.* [13] analyzed the application of electrochemical impedance spectroscopy (EIS) to

PEMFC research and highlighted the most representative works that perform local EIS measurements using SFC. Wu *et al.* [14] reviewed some approaches to measure local quantities such as temperature and current density. Wang [15] categorized the fundamental mathematical models that describe the physicochemical phenomena of PEMFC systems and stated that SFC can provide the experimental data required to validate them.

This Chapter targets: i) providing fundamental understanding of the design and characterization techniques of SFC ii) to discuss the influence of the most important design, assembling and operating parameters as well as the materials properties on the current density distribution (CDD) of SFC and iii) present the analytical techniques that have been combined with SFC since 1998.

## 2.3. Segmented PEMFC techniques

### 2.3.1. Main invasive approaches

The most frequently used invasive techniques for design, construction and electrochemical characterization of SFC can be classified into three categories: printed circuit board (PCB), resistors network and Hall effect sensors. These invasive techniques require segmentation of one or both of the following components: the CC, the BP and the GDL. There is no need to segment the membrane as it is ionically but not electrically connected to the GDL [16]. The three main techniques have been used at the German Aerospace Center (DLR) for both PEMFC and direct methanol fuel cells (DMFC) [1] characterization, a brief discussion of the advantages and disadvantages of each one was reported elsewhere [24]. It is noteworthy that SFC with different MEA active areas and number of segments have been studied using these techniques. The MEA active area is related to the power density of the cell while the number of segments is related to the resolution desired for the measurements. Small SFC with 1 $cm^2$ [17], 3 $cm^2$ [18], 5 $cm^2$ [19] and large with 370 $cm^2$ [9] and 578 $cm^2$ [20] MEA active area have been reported. The number of

segments ranged between 3 [21] and 196 [22]. Table 1 summarizes the main characteristics of the SFC and the invasive technique used.

Table 1 - References of studies divided by active area, number of segments and SFC invasive technique.

| | Cell Active area ($cm^2$) | | | | Number of segments | | |
|---|---|---|---|---|---|---|---|
| | 1 -22.5 | 25 - 56 | 100 - 130 | 200 - 578 | 3 - 16 | 18 - 49 | 81 - 196 |
| Printed Circuit Board (PCB) | [11, 18, 73, 93, 19, 26, 61, 107, 113] | [10, 25, 27, 55, 114] | [8, 115,56] | | [19, 26, 27, 55, 56, 61, 73, 93, 113, 114] | [8, 11, 18, 115, 107] | [10, 25] |
| Resistors network | [16, 28, 30, 32, 44, 50, 51, 60, 45, 80] | [29, 33, 36, 48, 49, 59, 96, 100, 78, 79, 81, 88, 94, 98, 102. 116, 117] | [31, 35, 37] | [9, 22, 34, 58, 103, 109, 86, 112] | [9, 16, 28, 30, 32, 33, 35, 37, 49, 50, 51, 96, 103, 109, 45, 78, 79, 81, 88, 94, 98, 102, 112] | [29, 31, 34, 36, 44, 48, 59, 100, 80, 86, 116, 117] | [22, 58, 60] |
| Hall effect sensors | | [46, 47, 52, 74, 53] | [12, 54, 92] | [20, 21, 40, 41, 57, 62, 75, 76, 77] | [12, 21, 40, 41, 46, 47, 52, 57, 62, 74, 75, 76, 77, 92] | [20, 53] | [54] |

The strategies used to segment the fuel cell components are described in detail in section 2.2, while some solutions to perform the local electrochemical measurements are given in section 2.3. Fundamental considerations on design and electrochemical characterization of SFC are presented in section 2.4. Below, the three most important invasive techniques are described in detail.

*Printed circuit board (PCB)*

The PCB technique for electrochemical characterization of SFC was introduced by Cleghorn *et al*. [21]. The basic idea behind this technique is to replace one or both CC with a PCB. Using PCB manufacturing techniques, a segmented current collector can be designed on a thin, flat surface providing electrically isolated paths for individual current/voltage measurement. The PCB is then placed between the flow field and the end plate, minimizing the local influence of the PCB on the thermal and electrical conductivity of the components while eliminating its interaction with the water evolution and transport inside the cell. The PCB substrates are epoxy-fiber glass [10, 24] or polytetrafluoroethylene PTFE [25]. To facilitate the connection of the SFC to the measurement unit, the PCB can be plated-through-hole (PTH) [8, 26]. The segments of the PCB are usually gold coated to avoid corrosion and minimize contact resistance. The reader is referred to [23] to deepen in PCB technology.

Interestingly, this technique offers the possibility to incorporate single straight [26], single [24] and multiple channel [10, 8] serpentine flow fields directly on the PCB. With this, the functions of the flow field are integrated in the current collector; less components are needed to assembly the cell and the current is measured nearer the reaction site as the PCB is in direct contact with the GDL. These characteristics allow the insertion of the PCB between intermediate cells of PEMFC stacks [24]. In single cells, when one current collector is replaced by a PCB the other can remain unaltered so that the PCB can be placed between the anodic [8, 27] or cathodic [10, 26] bipolar plate and the end plate. When the PCB is placed at the anode, the cathode is available for complementary studies concerning water management [25]. The electrode where the PCB is placed does not affect significantly the CDD measurements [19]. An exploded view of a SFC incorporating a PCB as anodic current collector is shown in Figure 2.2.

Company S++ (Germany) [111] offers three solutions for obtaining the CDD using the PCB technique: one oriented to large fuel cells and stacks, one with improved resolution capabilities (1152 segments) and the last with the flow fields incorporated directly on the PCB.

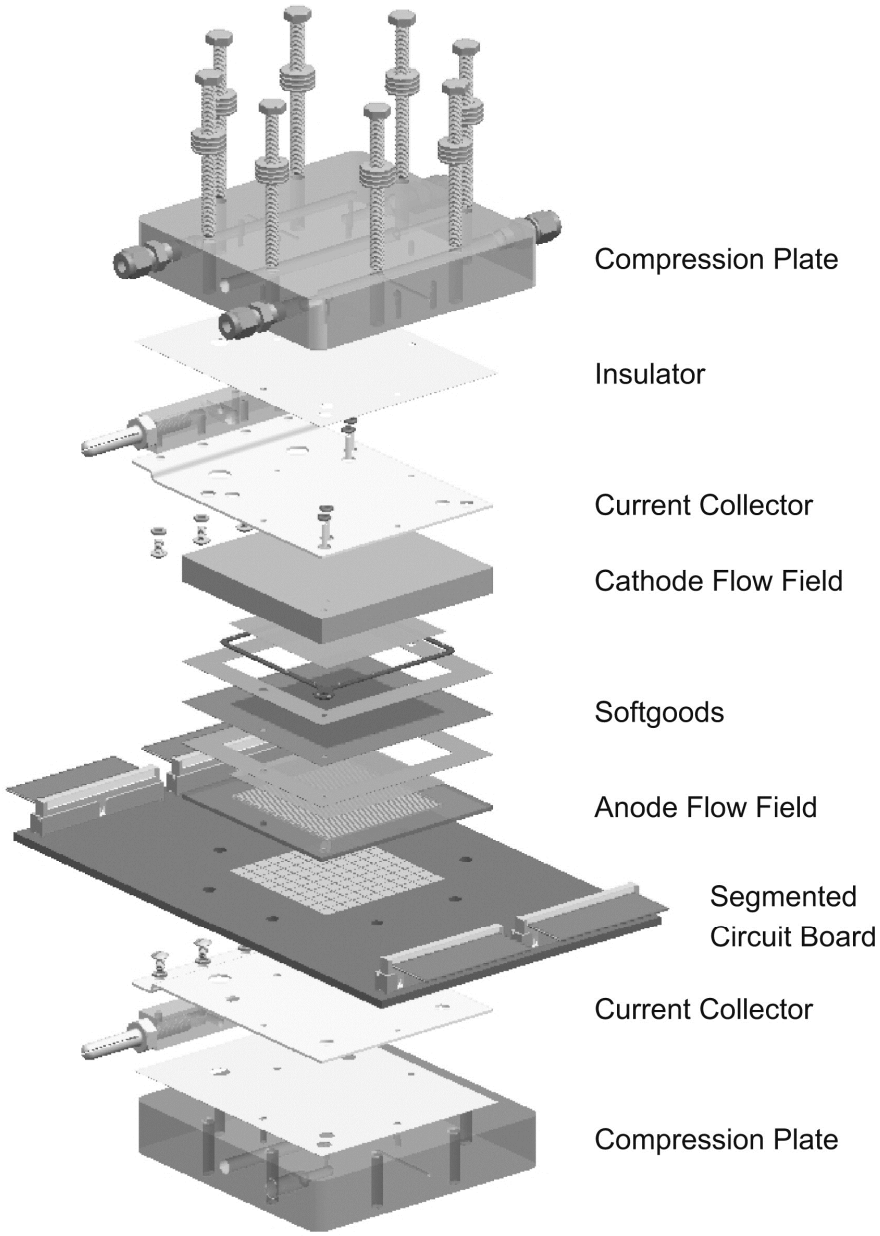


Figure 2.2. Exploded view of a segmented fuel cell assembly using the PCB approach. From Ref. [25] with permission.

*Resistors network*

The principles of the resistors network technique were introduced by Stumper *et al*. [29] who developed two methodologies to measure the CDD in operating PEMFC. The first one, the subcells approach, consists of punching out several circular pieces of the GDL, replacing them with smaller, electrically isolated pieces with the same characteristics, the subcells. In this form, the current density could be measured independently at specific regions of the cell. The second methodology involves the use of a current mapping plate formed by 121 identical graphite cylinders equally distributed over a hexagonal area that matches the MEA active area. The graphite cylinders were packed and placed between the flow field and the end plate, creating a passive resistor network that assisted the CDD measurements.

Generically, in the resistors network approach, the anodic, the cathodic or both BP of a PEMFC is/are divided into electrically isolated segments of the same shape, forming a resistors network that incorporate a portion of the flow field. The electrochemical characterization of the SFC can then be made in two ways: passively or actively. The passive method involves the connection of a "precision", "high resolution" or "shunt" resistor in series with every resistor of the network so that the current density of each segment can be calculated from the voltage drop over the precision resistor. The nominal value of the precision resistors used in SFC characterization is 0.1 Ω [29, 30, 31], 0.012 Ω [32] or 0.01 Ω [33]. The resistors network can be arranged in a segmented current collector, permitting the use of unaltered BP and GDL [37]. A detailed explanation of the measurement principles for the passive method is given by Morimoto *et al.* [28]. Figure 2.3 schematizes a segmented fuel cell using the resistors network technique and passive method for characterization. The cell has a segmented bipolar plate and gas diffusion layer at the anode and a precision resistor connected in series to each segment.

The active method involves direct connection of the resistors network to the measurement unit, eliminating the use of the precision resistors [16, 35, 45, 49, 59, 60]. In this case, the current flowing through each resistor of the network is read directly by the measurement unit.

Company Helmbold Messtechnik (Germany) [118] has developed a SFC with 196 segments and 244 $cm^2$ active area using a segmented graphite plate as cathode.

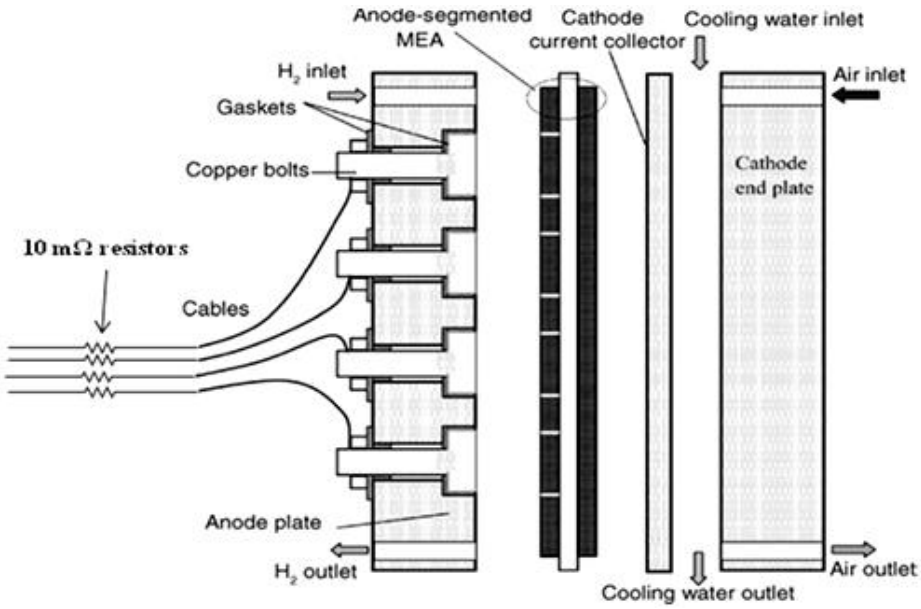


Figure 2.3. Schematic of a segmented fuel cell using the resistors network approach and passive method for characterization. Adapted from Ref. [33] with permission.

*Hall effect sensors*

The fundamentals of this technique were introduced by Wieser *et al.* [20]. This technique involves the association of one Hall effect sensor to every single electrically isolated segment of the segmented cell. A Hall effect sensor is a current transducer with four terminals: two for the connections to a source of current and two for the measurement of voltage across it [38]. Hall effect sensors work under the Hall effect principle, which states that when a conductor that carries current is placed into a magnetic field, a voltage is generated perpendicular to both the current and the field [39]. When a Hall effect sensor is used in a SFC, the density of the magnetic flux passing through the Hall element determines the output voltage of the sensor, which is proportional to the current generated by the segment. Two Hall effect sensors topologies, namely open loop [12] and closed loop [40] have been used for

SFC characterization. According to Geiger *et al.* [47] the closed loop Hall effect sensors are more accurate, more linear and easier to calibrate due to its lower sensitivity to changes in temperature. Interestingly, closed loop Hall effect sensors have been successfully used to measure the CDD at the outermost cells of a two and three cells PEMFC stacks [41]. Figure 2.4 schematizes the location of the Hall effect sensors integrated in the stack.

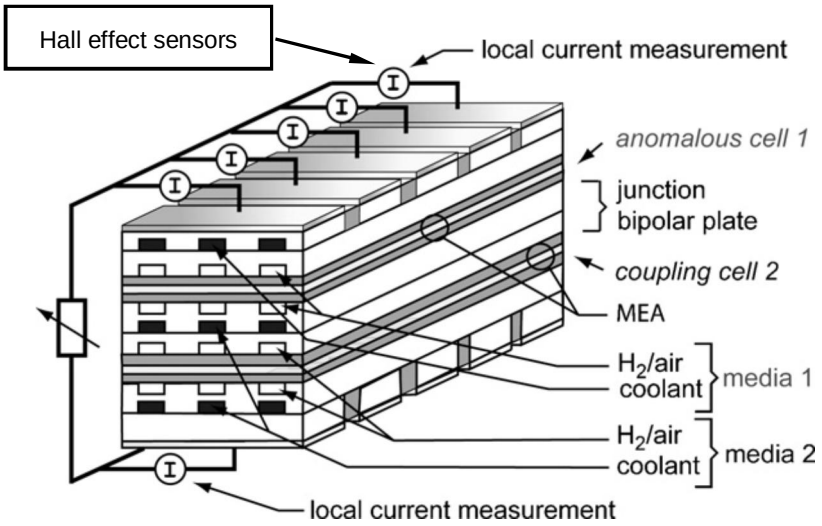


Figure 2.4. Simplified scheme of a two-cell (1 + 1) stack with independent media supplies and location of Hall effect sensors at the stack periphery. Adapted from Ref. [41] with permission.

### 2.3.2. Components segmentation

Early efforts to modify pertinent components of PEMFC in order to obtain distributed electrochemical information were made by Rieke and Vanderborgh in the late 1980´s [42]. Using modified photolithographic techniques, they created an array of microelectrodes placed directly on a perfluorosulfonic acid membrane in order to map the voltage and current distribution at the anode of a PEMFC. These authors highlighted for the first time the correlation between the spatially heterogeneous hydration of the membrane and the CDD. Another early work was presented by Vermeijlen *et al.* [43] who determined the potential distribution in an anodic gas diffusion layer made of carbon paper. Those authors used 25 small electrical contacts mounted on a perforated acrylic (Perspex®) support that was pressed against the

carbon paper. These authors computed the CDD along the carbon paper, concluding that the ohmic resistance of the carbon paper can play a major role in current and overpotential distribution of PEMFC.

More recent SFC designs incorporate different strategies to segment the GDL, the BP or the CC. The strategies presented below can help to design and construct SFC that use any of the three techniques previously introduced.

*GDL segmentation*

The GDL can be totally or partially segmented in a SFC. With its partial or total segmentation, some authors have tried to minimize the electrical interaction between segments at the GDL level, so that more accurate measurements can be obtained. Total segmentation of the GDL is achieved by using silicone [9, 12], Teflon® [8] or Teflon®/silicone [51] gaskets as a frame to accurately hot-press rectangular pieces of GDL over the membrane. A scheme of a totally segmented gas diffusion layer is presented in figure 2.5a Hakenjos *et al.* [44] reported the only study using a partially segmented gas diffusion layer. It was prepared by cutting out 0.2 mm wide gaps from a Toray carbon paper gas diffusion layer, as seen in Figure 2.5b As a result, the ohmic resistance between adjacent segments increased up to 0.5 Ω.

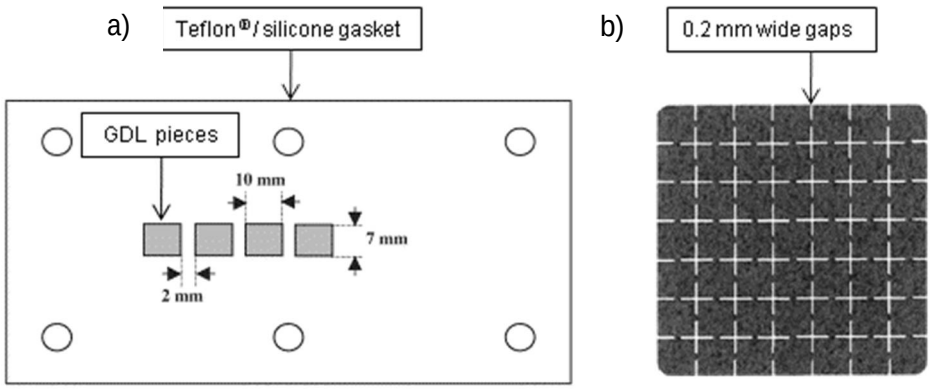


Figure 2.5. a ) scheme of a totally and b) picture of partially segmented GDL for use in SFC. From Ref. [51] (left) and [44] (right) with permission.

*BP and CC segmentation*

Segmented BP suitable for SFC studies can be manufactured directly from a graphite block using computerized numerical control techniques (CNC) and a bonding agent, which is usually an epoxy resin that provides good electrical insulation and mechanical stability [27, 46]. The manufacturing process involves the following steps [27, 46]: 1) the segments are partially milled, 2) the gaps are filled with resin, 3) once the resin is cured, the opposite face of the plate is milled so the segments are electrically isolated, 4) both sides of the BP are polished and 5) the flow field is machined. The most important manufacturing steps are schematically illustrated in Figure 2.6 for a bipolar plate with 9 segments. A similar strategy was presented by Geiger *et al.* [47] who first glued three graphite bars with a two-component epoxy adhesive. After the epoxy adhesive was cured, the glued plate was milled perpendicular to the bonding surface and reunited following the same procedure as before. Finally, the flow field was machined.

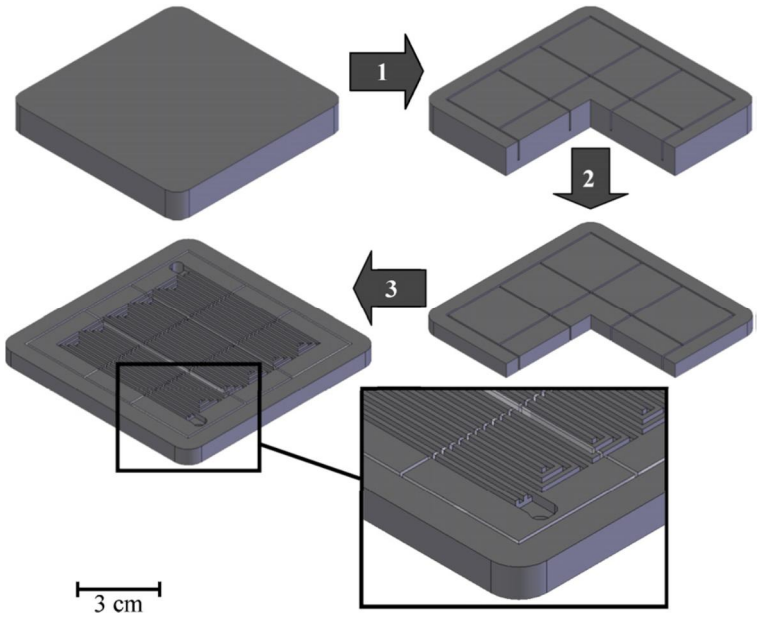


Figure 2.6. Illustration of the manufacturing process of a segmented flow field plate made of graphite. From Ref. [27] with permission.

The BP can also be segmented by embedding conductive blocks with the shape of a prism, normally quadrangular, into a non-conductive polymeric frame. After that, the

flow field can be machined. A picture of a segmented bipolar plate with 16 titanium-coated stainless steel blocks (segments) inserted in a polyoxymethylene frame is schematically shown in Figure 2.7. Non-conductive materials used as frames include polysulfone [18, 35, 48], polycarbonate [30, 31, 49, 50], acrylic [9, 51], polyoxymethylene [52], polyetherimide [12], poly(methyl methacrylate) [53], bakelite [54] and organic glass [40]. Conductive materials embedded in the polymeric frames are copper [35, 37], graphite [9, 12, 18, 40, 48, 49, 51, 54] and stainless steel [30, 50, 52]. In order to prevent corrosion and reduce contact resistance, the conductive blocks are usually coated with gold [35, 37, 49] or titanium [52]. Direct current collection is then obtained by attaching copper wires [30, 35], gold wires [53], coated with silver copper sticks [40], stainless steel pins [50] and copper blocks [54] to the conductive prisms. Alternatively, copper bolts can be inserted in a block of the same material and then electrically isolated using plastic gaskets [33]. To prevent reactants leakage, epoxy [12, 52] and bakelite resins [54] can be used.

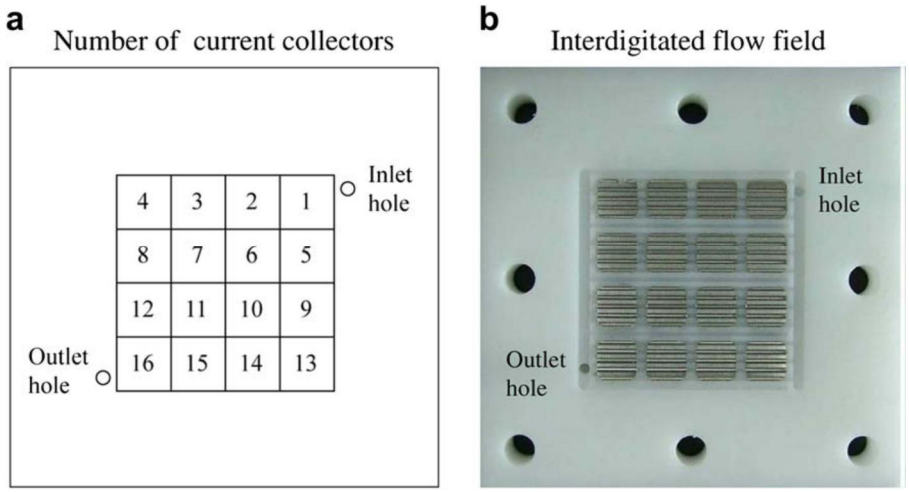


Figure 2.7. To the left, location of the current collection segments. To the right, segmented bipolar plate fabricated by inserting conductive prism-shaped blocks (silver gray blocks) into a non-conductive polymeric frame (in white). From Ref. [52] with permission.

The integration of segmented BP with similar characteristics than the ones used in real stacks has also been reported. Büchi *et al.* [57] developed the so called "semi-segmented plate" concept. The plate consists of three elements: i) a pressure molded flow field made of a graphite-polymer mixture with high specific resistivity ($\rho$) ≈ 25

$m\Omega \cdot cm^{-1}$), ii) highly conductive segments of sintered graphite glued to the flow field with $\rho \approx 1\ m\Omega \cdot cm^{-1}$) and iii) individual metal current collectors. The "semi-segmented plate" has the same electrical, fluid dynamic and thermal properties as the BP used in PEMFC stacks with up to 125 cells.

An interesting contribution was made by Ghosh *et al.* [34] who refined the current mapping plate concept. The plate was made of expanded graphite with 20 segments and isolated copper wires attached for current collection. Furthermore, the plate was sandwiched between two semi-segmented and two unaltered plates, forming a five-layer CDD measuring device with a thickness of 3 mm that can be integrated in PEMFC stacks.

It is noteworthy that Noponen *et al.* [29] incorporated a segmented current collector in a free breathing PEMFC. In a free-breathing or open cathode PEMFC, natural convection is the driving force for oxidant distribution along the cathode GDL as it is open to the atmosphere. A polyvinyl chloride (PVC) block served as electrical insulator of the 48 cathode gold-plated stainless steel current collectors. Every current collector (positioned orthogonally to the end plate surface) had a screw to adjust height and assure good electrical contact with the GDL. An aluminum endplate was attached to the PVC block to provide mechanical stability. Figure 2.8 shows details of this segmented current collector.

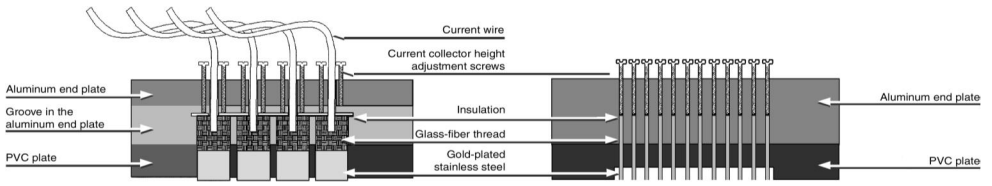


Figure 2.8. Cross-sections from the segmented cathode flow-field plate. The left one is the vertical and the right one is the horizontal cut. From Ref. [29] with permission.

### 2.3.3. Local current/voltage measurement

To obtain relevant electrochemical information of a segmented cell it is important to measure the current, voltage, high frequency resistance (HFR) and/or electrochemical impedance spectroscopy (EIS) of each segment. It is important to

mention the efforts made by some research groups aiming to compensate the voltage drop across the segments when using the PCB and the resistors network approach for CDD measurements.

Kulikovsky *et al.* [18] plugged the PCB of their SFC to a measurement unit that incorporates a shunt resistor and an amplifier to convert the current into a voltage signal. The unit included a circuit for voltage drop compensation across the PCB paths and shunt resistor, providing in this way equal potential to all segments. A system for active voltage drop compensation using a PCB was developed by Sauer *et al.* [11]. The system included the connection of the segments to a voltage source and a transistor in series with a shunt resistor. Santiago *et al.* [27] proposed another solution to measure the current and voltage in a PCB with voltage drop compensation. Each path of the PCB permitted the connection of the segments to individual low impedance (0.18 mΩ) closed loop Hall effect sensors. The current measured by the Hall effect sensors was then converted to a potential by connecting the former to individual precision resistors of 1 kΩ.

Concerning the resistors network technique, Siroma *et al.* [60] reported the use of a data logger and a 100 channel zero-shunt current/voltage converter to obtain the current and minimize voltage drop through the segments. Tabe *et al.* [31] reported another strategy, these authors connected variable resistances to each segment, so that their individual resistance could be calibrated and the difference in contact resistance compensated. At the beginning of the experiments, the overall cell resistance was set to a constant value by adjusting the variable resistances in order to obtain a uniform CDD of 0.5 $A \cdot cm^{-2}$.

The use of Hall effect sensors facilitates the measurement of the CDD, being necessary only a data acquisition (DAQ) unit and a multiplexer as done by Wieser *et al.* [20] and Geiger *et al.* [47].

Complementarily, HFR and EIS measurements can be performed with in-house built measurement systems [46] or commercial Frequency Response Analyzer (FRA) [8, 12, 32, 61]. Companies Zahner-elektrik GmbH & Co. KG (Germany) and Arbin Instruments

(USA) offer multichannel potentiostats/galvanostats to perform both CDD and EIS measurements.

### 2.3.4. Fundamental considerations for SFC design

*Components*

In this section, general recommendations for segmentation of the components are given. First of all, it should be noted that GDL segmentation requires BP and CC segmentation, increasing the complexity of the design and its assembly [40, 49]. To overcome this, partial segmentation of the GDL is a fair option as it reduces electrical interaction between segments and is not as time demanding as total segmentation. Total segmentation of the GDL can lead to misalignment problems between corresponding anodic and cathodic parts of the GDL, the same that can lead to membrane failure due to thinning via chemical degradation and pinhole formation [104].

If the BP are segmented, they must provide uniform and robust mechanical support to the MEA, otherwise the MEA can break down at high current densities (≈1 $A \cdot cm^{-2}$) from the places with poor mechanical support [59]. Gas leakages may appear if segmented the BP are constructed by inserting conductive prisms into a non-conductive polymer frame. The use of epoxy resins is a common practice as it prevents gas leakages and glues the prisms to the frame. It is very important to reduce the electrical resistances of metallic surfaces by coating them with titanium, silver or gold; another option is to insert graphitic foils between them.

It is important to keep the pressure distribution between components as uniform as possible or the segments will have different contact resistances, affecting the measurements. The pressure distribution between surfaces can be checked with pressure sensitive films [12, 36] while uneven contact resistance can be corrected by connecting a variable resistance to every segment as stated above. More sophisticated ways to evaluate the contact resistance variations between segments involve measuring the HFR each segment at two different relative humidity (RH)

conditions with the SFC running on air at the anode and the cathode [53] or using the four wire resistance measurement method to determine their impedance [27].

Regarding the wiring array used to connect the cell to the measurement unit, it must be kept as short as possible to reduce ohmic losses [19].

*Uncertainties associated to the use of SFC*

There are uncertainties related to structural differences between SFC and regular PEMFC. The evaluation of these uncertainties has served to validate the use of SFC as analytical technique and has been focused on two aspects: i) the need of GDL and BP segmentation and ii) the relative error introduced by the auxiliary measurement circuitry system of SFC.

The discussion around the need of GDL and BP segmentation has been focused on how the in-plane and through-plane electrical conductivity of components (i.e. the use of non-segmented GDL along with segmented BP) affect the local electrochemical characterization of the segments. Researchers have evaluated the need of the GDL or the BP segmentation both numerically and experimentally. All the mathematical models used to evaluate numerically the uncertainties aimed to simulate the solid phase potential distribution in repetitive current-collecting elements at different current densities [29, 51, 56].

For example, Noponen *et al.* [29] used 48 electrically isolated pins in direct contact with a non-segmented GDL for direct current collection and observed a difference in performance no greater than 10% between adjacent segments at different experimental conditions. These authors also simulated the effect of using a non-segmented GDL on the current collection of four neighboring segments using the FEMLAB® multiphysics software package. From the simulations, they concluded that current density from each segment can be measured with reasonable accuracy even if the GDL is not segmented as far as the contact resistance differences between the segments and the GDL are minimized. Natarajan and Nguyen [51] evaluated the effect of GDL segmentation in a different form. These authors obtained galvanostatic and potentiostatic polarization curves for each segment using segmented BP and CC.

Segmented and non-segmented GDL were used in the MEA and the results were compared. For both segmented and non-segmented GDL, differences in segment performance were minimal in the galvanostatic tests. The potentiostatic tests showed a minimal difference in performance for each segment when using a segmented GDL. For the non-segmented GDL, on the other hand, the potentiostatic tests showed a significant difference in performance for each segment. Overall cell performances were similar, irrespective of the type of test, potentiostatic or galvanostatic. Finally, it was recommended: i) to segment the GDL along with the BP and the CC as contact resistance variations between the BP and the GDL are negligible, irrespective of the type of test and ii) to perform galvanostatic tests rather than potentiostatic tests if the GDL is non-segmented, as this minimizes differences for each segment performance due to uneven electrical contact resistances between the segments and the GDL.

The need of BP segmentation was discussed by Eckl et al. [56], who evaluated the effect of BP segmentation using a segmented anodic bipolar plate with resistors network and a non-segmented anodic bipolar plate with a PCB as current collector. The cathodic bipolar plate and current collector as well as the GDL remained unaltered in both cases. For the resistors network case, the major parameters causing lateral current spreading (from segment to segment) were found to be the resistance difference of the individual measurement circuits and the current density gradient between neighboring segments. Due to non-segmentation of the bipolar plate, the PCB showed higher lateral current spreading; however, it was proposed by these authors that the use of a PCB along with non-segmented BP provide a good alternative for CDD measurements.

The error introduced by the auxiliary measurement circuitry has been evaluated individually for each approach and concerns the use of PCB, resistors network and Hall effect sensors. Regarding the use of PCB, Sauer *et al.* [11] used an empirical formula to calculate the relative error in current measurements introduced by their PCB with active voltage drop compensation. The cell was operated galvanostatically; it had a non-segmented GDL and segmented anodic bipolar plate and current

collector. The relative error of the current measurement was less than 6.5%. Concerning the use of precision resistors, Noponen *et al.* [59] and Liu *et al.* [33] used non-segmented and segmented GDL respectively. In both studies, only the anodic flow field and current collector were segmented. Relative errors in the range 1-2% were found in both cases. With respect to Hall effect sensors, Wieser *et al.* [20] used a segmented anodic and a regular cathodic bipolar plate. The GDL remained unaltered. After measuring the lateral currents at the GDL, they computed a relative error below 5% for the current gradient between neighboring segments. Due to calibration of the Hall effect sensors used, Geiger *et al.* [47] and Santis [62] reported relative errors within 1% and between 0.17-0.5%, respectively.

### 2.3.5. Other invasive approaches

This section describes how the local electrochemical behavior of operating PEMFC can be studied using different segmentation strategies and analytical techniques than the ones listed before. Sun *et al.* [68] developed a current measurement gasket technique. The gasket was fabricated of an epoxy resin and glass cloth substrate. On one side of the gasket, 23 gold-plated copper rectangles were outlined in such a way that those surfaces matched exactly the 23 single channel flow field ribs of the cathode. Once assembled, the current collection portions were in direct contact with the cathodic gas diffusion layer. Both the anodic and cathodic BP suffered no modifications. The gasket adapted for CDD measurements is shown in Figure 2.9.

Some research groups have focused on increasing the resolution of CDD measurements. A methodology to measure the current under the gas channel and under the rib of a flow field was reported by Wang and Liu [67]. Three MEA with a regular anode and a differently arranged cathode were assembled. The first cathodic GDL was loaded with catalyst only at the regions above the gas channels, the second was loaded at the region above the single rib and the third was fully covered with catalyst. The resolution of measurements was further increased by Freunberger *et al.* [17] and Büchi and Reum [65] from the Paul Scherrer Institute. These authors reported local current density and local membrane resistance measurements with

sub-millimeter resolution using a laboratory PEMFC with 1.3 $cm^2$ active area. The measurement methodology is explained in a report by Freunberger *et al.* [66].

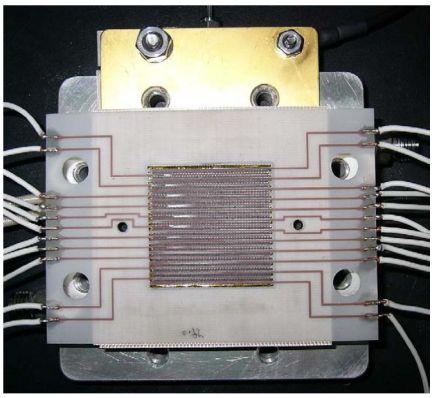

Figure 2.9. Picture showing the location of the current distribution measurement gasket. From Ref. [68] with permission.

The indirect determination of the CDD has been achieved in different ways. Wilkinson *et al.* [69] calculated the CDD along the channel of a Ballard Mk V single PEMFC from local temperature distribution measurements. Seventeen K-type thermocouples of 0.254 mm diameter were embedded in different locations of the anode flow field. Heat generation due to the exothermic reaction of hydrogen oxidation was correlated to the temperature of each thermocouple. Another way to indirectly estimate the CDD was reported by Araki *et al.* [32]. These authors used a gas chromatograph (GC) to measure the gas composition of reactants along a cathode with eight gas sampling ports. The CDD was calculated from the decreased flow rate of $H_2$ and $O_2$ along the flow field. Alternatively, Candusso *et al.* [63] and Sailler *et al.* [64] used one-axe and two-axe sensitive magnetic field sensors, respectively, to measure the instantaneous magnetic field as close as possible to the MEA. The CDD was then calculated using the Maxwell´s equations.

### 2.3.6. Non-invasive approaches

The non-invasive approaches for local electrochemical characterization of operating PEMFC present the particularity that no physical modifications are made to any of the components involved in the fuel cell assembly. Non-invasive techniques are

supported by sophisticated magnetic field measurement devices. Claycomb *et al.* [70] employed high temperature superconducting (HTS) and low temperature superconducting (LTS) direct current Superconductive Quantum Interference Devices (SQUID) and flux gate magnetometers to obtain spatial magnetic field maps of an operating PEMFC. SQUID are magnetic flux-to-voltage transducers often used in non-destructive and non-invasive analysis of materials [71]. Hauer *et al.* [72] introduced a magnetic inducted tomography technique to indirectly measure the CDD. Two 3D magnetic field sensors were used for the readings. One sensor scanned the upper while the other scanned the lower part of the cell. The experimental set-up allowed four-axis scan measurements, creating a CDD map of the fuel cell.

## 2.4. Parameters influence on current density distribution

The simplest way to study the distributed electrochemical performance over the MEA active area is to measure the CDD. In this section, the effect of relevant design, assembling and operating parameters as well as the use of different MEA materials on CDD is discussed. To analyze the effect of one parameter, researchers have kept constant the others. Table 2 summarizes the parameters studied using SFC.

The CDD profiles have been graphically presented in several forms, for example: as a surface on which the current density is represented as discrete sections of the MEA active area [54, 55, 86], as a trend line on which the current density is presented as a function of the fractional distance from the inlet of the cell [109, 113] and as a trend line on which the current density is presented as a function of every segment of the cell [33, 48, 75].

Despite its importance, few authors have developed strategies for homogenizing the CDD. Santis *et al.* [119] tried to achieve this goal by using cathodic GDL with different Pt catalyst loading gradients along the air flow field channels. The anodic and cathodic GDL had an average Pt loading of 0.6 $mg \cdot cm^{-2}$. Below, the effect of each parameter on the CDD is discussed in detail.

Table 2 - References analyzing parameters that influence the current density distribution using SFC.

| Parameter | References |
|---|---|
| Design/assembly | |
| Flow field geometry | [96, 31, 19, 59, 80, 52, 97] |
| Clamping pressure | [9, 31, 20] |
| Operating | |
| Reactants relative humidity | [8, 9, 10, 28, 21, 113, 73, 25, 117, 59, 37, 79, 33, 45, 102, 103, 86, 49, 50, 81, 54, 57, 52, 77] |
| Reactants flow rate | [8, 100, 41, 28, 31, 21, 73, 116, 36, 117, 48, 98, 44, 59, 32, 79, 33, 45, 109, 34, 86, 88, 49, 30, 91, 22, 35, 57, 46, 120, 75, 76, 52, 77, 53, 40, 77] |
| Operating pressure | [33, 34, 86, 88, 68, 85, 67] |
| Contaminant species (CO, $CO_2$ and $NO_2$) | [58, 93, 114, 94, 92, 40, 112] |
| Materials | |
| Membrane thickness | [49, 55] |
| GDL macrostructure | [10, 51, 81] |
| Permeability of the membrane to methanol | [91] |

### 2.4.1. Flow field geometry

In a PEMFC, the flow field geometry determines how the reactants are distributed over the MEA active area. So far, the flow fields considered in SFC studies have been: single channel and multiple channels serpentine flow fields [36, 55, 54, 49, 8, 34]; straight single and multiple (parallel) channels flow fields [26, 18, 50, 53, 48, 25]; flow fields with net/grid geometry [59, 96], interdigitated flow fields [95], self-draining stirred tank reactor (STR) flow fields [80] and biomimic flow fields [52].

Several research groups have aimed to compare different flow field geometries using CDD profiles. Hogarth *et al.* [80] compared two cathodic flow fields, a single channel serpentine and an STR. The anodic flow field had a net/grid geometry in both cases. The comparison was done under three low humidity conditions, the first with the anode humidifier temperature ($T_{hum,a}$) equal to the cathode humidifier temperature ($T_{hum,c}$) at 30 °C, the second with $T_{hum,a} = T_{hum,c} = 10$ °C and the third dry. The

temperature of the fuel cell ($T_{cell}$) ranged from 75 to 85 °C. The stoichiometric ratio of hydrogen ($\lambda H_2$) ranged from 1.2 to 4.6 and the stoichiometric ratio of air ($\lambda_{air}$) ranged from 1.9 to 3.3. The STR showed improved overall performance at both the highest (5 - 10% improvement) and the lowest (≈ 25% improvement) RH conditions. Both tests showed higher current densities towards the outlet, nevertheless the single channel serpentine flow field showed very low activity at the cathode inlet in the dry condition. Recently, Hwnag *et al.* [52] evaluated four different cathodic flow fields namely a parallel, a multiple channels serpentine, an interdigitated and a biomimic (square-wave geometry) using CDD measurements. At the anode, a multiple channels serpentine flow field was used. The cell was operated at different conditions: $40 \leq T_{cell} \leq 60$ °C, $T_{hum,a} = 40$ °C, $\lambda_{H2} = 1.5$, $40 \leq T_{hum,c} \leq 70$ °C and $2.5 \leq \lambda_{O2} \leq 3.5$. The CDD was tracked for 45 min. Due to superior mass transfer (diffusion) and water removal capabilities, the multiple channels serpentine flow field showed the most steadily CDD and the highest power density among the cathodic flow fields tested. The comparison of the parallel and the multiple channels serpentine flow field is shown in Figure 2.10.

Hiseh *et al.* [19] developed a comparative study involving interdigitated, multiple channels serpentine, parallel and net/grid geometry flow fields while Zhang *et al.* [97] compared interdigitated and single channel serpentine flow fields. In both studies the anode and cathode had equal flow field geometries during the CDD measurements. These authors observed a more uniform CDD profile for transient ($0 < t < 3$ h) [19] and steady-state [97] operation when using the interdigitated flow field on both electrodes. The last was attributed to the convection-driven mass transfer mechanism of the reactants in this type of flow fields.

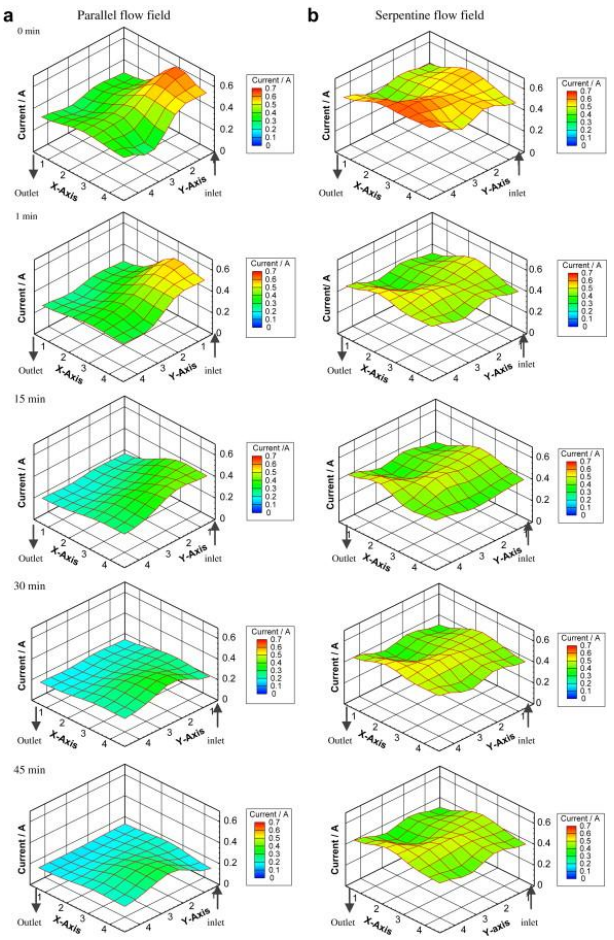


Figure 2.10. Transient developments of the local current distribution, (a) parallel flow field and (b) serpentine flow field, $U$ = 0.5 V, $T_{cell}$ = 40 °C, $\lambda_{H2}$ = 1.5 and $\lambda_{O2}$ = 2.5. From Ref. [52] with permission.

The effect of most relevant flow field geometric parameters (e.g. channel/rib width) on CDD was investigated by Reum *et al.* [110]. Several channel/rib configurations were used in their SFC with increased CDD measurement resolution. It was concluded that a flow field design with wider ribs and smaller channels can lead to higher and more homogeneous performances for a wide range of operating conditions (oxygen fractions above 10%) due to improved water management.

It is accepted that, on a general basis, more uniform CDD profiles are observed when reactants are fed in counter flow mode, that is, when the fuel and oxidant inlet and outlet are located at opposite sites [28, 30, 46, 98].

Concerning DMFC, Gülzow *et al.* [96] compared a net/grid and a single channel serpentine flow field placed at the cathode. A net/grid flow field was used at the anode in both cases. The methanol flow rate ($Q_{met}$) was 20 ml·min$^{-1}$ and had a 1.5 M methanol concentration while the air flow rate ($Q_{air}$) was 600 ml·min$^{-1}$, dry. The anode and cathode pressure was 2.5 and 3.5 bar respectively and $T_{cell}$ = 90 °C. The CDD profile for the serpentine flow field was more homogeneous and showed a low current density zone near the cathode inlet associated to the drying effect of air on the membrane. The net/grid flow field showed high activity at center while the corners were producing almost no current.

### 2.4.2. Clamping pressure

In PEMFC systems, the clamping pressure is related to the tightening torque applied to the bolts located at the endplates. The clamping pressure is equal to the force required to compress the MEA, gaskets, BP and CC so that the pressure between these components is as uniformly distributed as possible and the PEMFC is gas tight. Due to differences in design and materials, every PEMFC system has its own clamping pressure. Using SFC, few groups have investigated the effect of clamping pressure on CDD; nonetheless, this is a parameter that must be taken into account when assembling a single cell or stack. Indeed, a recent study [99] reported that the local mass, charge and heat transfer properties of the GDL can vary significantly due to inhomogeneous compression caused by the flow field geometry of the BP over the MEA. Tabe *et al.* [31] analyzed how two different clamping pressures (0.6 and 1.2 MPa) affected the CDD at $T_{hum,a}$ = $T_{hum,c}$ = 40 °C and $T_{cell}$ = 50 °C and for $\lambda_{H2}$ = 1.3 and $\lambda_{O2}$ = 1.4. The CDD was measured 240 s after starting the experiments. The CDD was higher for 0.6 MPa because of the lower mass transfer resistance of the GDL. On the other hand, the higher clamping pressure exhibited a more uniform CDD due to a more uniform contact pressure between the GDL and the BP.

### 2.4.3. Relative humidity of reactants

In technical fuel cells, gradients in reactant RH are unavoidable along the flow fields [82]. The RH of reactants plays a key role in keeping a correct level of hydration of

the membrane and strongly influences the water transport mechanisms, namely the electro-osmotic drag (from anode to cathode) and the back-diffusion (from cathode to anode) of water [83]. Generally, as reactants are fed at lower saturation states, the membrane will not achieve a good hydration level near the inlet, increasing the local membrane resistance. On the other hand, if reactants are oversaturated, too much water will be present near the outlet leading to GDL pore blocking (flooding).

Cleghorn *et al.* [8] studied the effect of increasing the anode RH on CDD and local HFR for a SFC with multiple channels serpentine flow fields at $T_{cell} = T_{hum,c} = 80$ °C, $Q_{air} = 5000$ ml·min$^{-1}$ and hydrogen flow rate ($Q_{H2}$) of 700 ml·min$^{-1}$. Three RH conditions were considered for the anode, $T_{hum,a} = 80$ °C and $T_{hum,a} = 100$ °C and dry condition. The oversaturated condition showed highest, more homogeneous current density and the lowest, more homogeneous HFR. The other cases showed an increase in current density and a decrease in HFR towards the outlet, with a better performance for the saturated condition. Sun *et al.* [84] analyzed the effect of increasing the anode RH for: i) dry cathode feed and ii) saturated cathode feed. For the first case $T_{cell} = 59.85$ °C and for the second $T_{cell} = 69.85$ °C. For the first case, $Q_{H2} = 250$ ml·min$^{-1}$ and $Q_{air} = 700$ ml·min$^{-1}$, for the second, $Q_{H2} = 200$ ml·min$^{-1}$ and $Q_{air} = 600$ ml·min$^{-1}$. Each run lasted 6.5 h and the $T_{hum,a}$ was gradually increased from $39.85 \leq T_{hum,a} \leq 89.85$ °C starting at non-humidified conditions. For the first case (dry cathode feed), and even at oversaturated conditions of the anode, the membrane never reached a fully hydrated state and the local current density increased towards the outlet. For the second case (saturated cathode feed), the cell showed a steadily decrease in current densities from the inlet to the outlet accentuated at anode oversaturated conditions as a result of flooding.

Noponen *et al.* [59] studied the effect of feeding pure oxygen with two different RH. These authors considered a segmented cell with an anodic net/grid geometry flow field and a cathodic special flow field with multiple inlets and outlets. For the studies, $T_{hum,a} = T_{cell} = 60$ °C, $\lambda_{H2} = 3.4$ and $\lambda_{O2} = 5.5$. The $T_{hum,c} = 60$ °C for the high humidity and $T_{hum,c} = 40$ °C for the low RH conditions. The high RH condition showed a more uniform CDD. The low RH condition showed a slight increase in current density

towards the cell outlet attributed to improved proton conductivity and a dryer state of the polymer near the inlet. Yoshioka *et al.* [37] performed CDD measurements at various fuel and oxidant stoichiometries for $T_{cell}$ = 75 °C and $T_{hum,a}$ = $T_{hum,c}$ = 65 °C. Hydrogen and air stoichiometries ranged between 1.25 and 2.5. The CDD profiles obtained are shown in Figure 2.11. It is observed that under low RH conditions the local current density depends only on the stoichiometry of air. These authors concluded that the region with higher current density for $\lambda_{H2}$ = 1.3 and $\lambda_{O2}$ = 2.5, tend to move upwards the flow field gas channel for long-term (250 h) operating regimes. Similar results have been reported by other research groups [8, 57, 108].

Yoon *et al.* [54] analyzed the flooding effect on CDD. A saturated and two oversaturated conditions (≈ 300% RH and ≈ 600% RH) were tested for both the anode and cathode at $T_{cell}$ = 27 °C, $\lambda_{H2}$ = 1.25 and $\lambda_{O2}$ = 2.5. They concluded that the flooding process begins at the outlet and progressively moves towards the inlet of the cell.

Reum *et al.* [82] used their segmented cell with sub-millimeter resolution to measure the CDD under the ribs and under gas channels of the flow field at different RH conditions. For the experiments, $T_{cell}$ = 70 °C, $\lambda_{H2}$ = 23 and *RH* = 40%. The cathode was fed with air ($\lambda_{air}$ = 10) and oxygen ($\lambda_{O2}$ = 46) for *RH* between 0 and 100%. Higher current densities and lower ohmic resistances were observed under the gas channels of the flow field at higher RH and were attributed to the fact that the gas channels area has lower mass transport restrictions compared to the flow field ribs. They also found that the local membrane resistance changes mainly under the gas channel as a result of the limited membrane humidification under the rib covered zones.

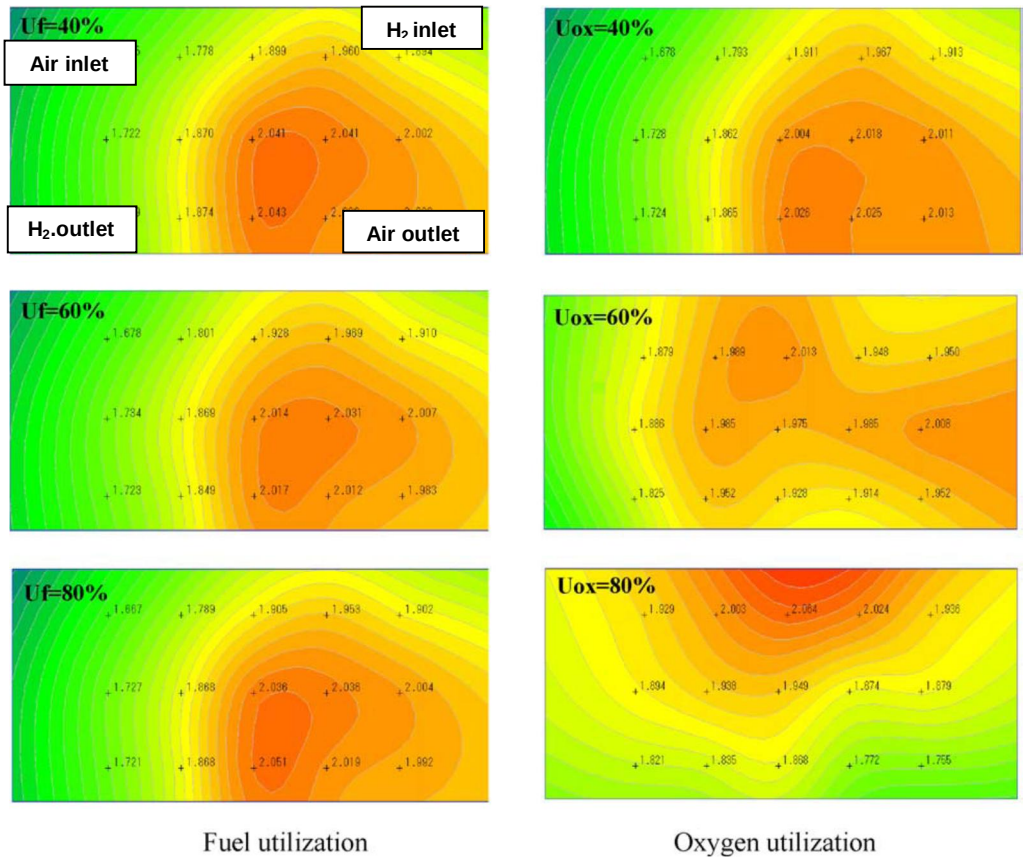


Figure 2.11. Current distributions at different gas utilizations. Left figures—the influence of fuel utilization at a constant oxygen utilization of 40%. Right figures—the influence of oxygen utilization at a constant fuel utilization of 75%. Average current density is set at 0.25 A·cm$^{-2}$. The temperatures are kept at a constant of 75 °C by circulation of coolant. Dew points of gases are kept at a constant of 65 °C. Adapted from Ref. [37] with permission.

### 2.4.4. Reactants flow rate

CDD measurements can provide information about specific zones of the cell where reactants are insufficient (fuel or oxidant starvation). In PEMFC, the performance is extremely sensitive to cathode stoichiometry due to relatively sluggish oxygen reduction reaction (ORR) kinetics and mass transport [36]. At the same time, operating the anode under low stoichiometric conditions may originate fuel starvation, resulting in carbon corrosion. The oxygen produced in the water oxidation reaction can then react with the hydrogen producing excessive local heat that degrades the catalyst [87]. The responsible mechanisms for depletion of the

reactants along the flow field channels are: upstream consumption, which leads to an scarcity of reactants downstream, blockage of the flow field channel, inadequate water removal from the flow field channels and restricted access of reactants to the electrode due to poorly designed flow fields [73].

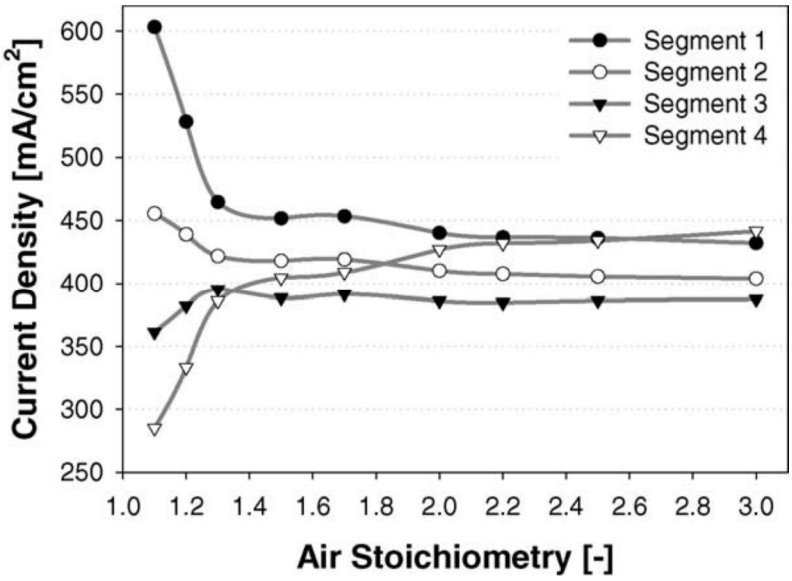


Figure 2.12. Deviation of current density from average current density in the segments 1–4 as function of total cell current. Cell operated in constant flow mode with gas flows rates corresponding to $\lambda_{H2}$ = 2 and $\lambda_{air}$ = 1.5 @ 80 A total cell current (400 mA·cm$^{-2}$). $T_{cell} = T_{hum,a} = T_{hum,c}$ = 70 °C. From Ref. [57] with permission.

Natarajan and Nguyen [45] studied the effect of hydrogen starvation in a straight single channel segmented cell with five segments (organized as a horizontal row) at $T_{cell} \approx$ 30 °C, $T_{hum,a}$ = 40 °C, $T_{hum,c}$ = 30 °C, $Q_{H2}$= 5.1 ml·min$^{-1}$ and oxygen flow rate ($Q_{O2}$) of 19 ml·min$^{-1}$. Current density was tracked during 30 min for 0.70, 0.60 and 0.55 V. When segments were at 0.70 V, hydrogen was in excess for the reaction and current densities were stable for all segments. For 0.6 V, starvation effects were observed in segments four and five as more than 70% of the hydrogen was consumed at the three first segments. Finally, at 0.55 V the starvation effects were observed in segments three, four and five, with the last two generating almost no current.

Büchi *et al.* [57] operated a segmented cell of technical relevance (200 cm$^2$ cell active area) at different oxidant stoichiometries 1.1 $\leq \lambda_{air} \leq$ 3. Other operating conditions

were $\lambda_{H2} = 2$, $T_{cell} = T_{hum,a} = T_{hum,c} = 70$ °C. Galvanostatic tests were performed at a current density ≈ 400 mA·cm$^{-2}$. It was observed that at low stoichiometries, $1.1 \leq \lambda_{air} \leq 1.5$, the first two segments were producing most of the current due to oxidant depletion along the flow field path. At higher stoichiometries, $\lambda_{air} > 1.5$, the CDD became relatively homogeneous. These results are shown in Figure 2.12 where segment one is located at the inlet and segment four at the outlet of the cell. Other authors have observed relatively homogeneous CDD at $\lambda_{air} \geq 2.9$ [8] and $\lambda_{air} \geq 2$ [28]. Both the fuel [40, 80] and oxidant [53, 68, 73] starvation condition have further been studied leading to similar results.

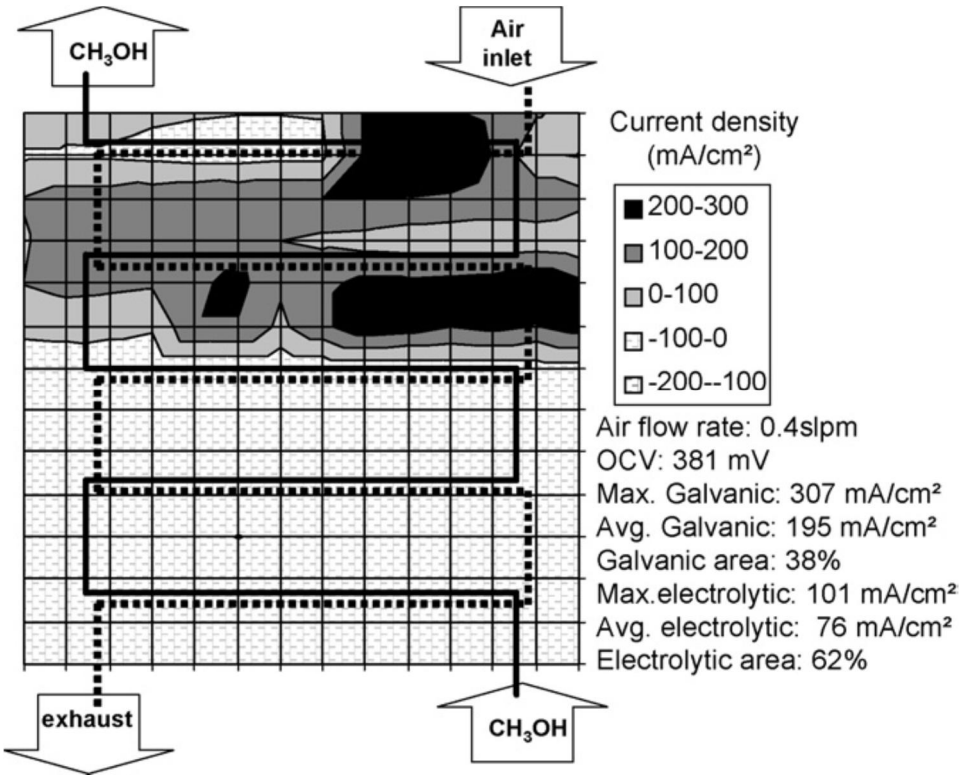


Figure 2.13. Local current densities with air supply of 0.4 L·min$^{-1}$ at OCV; anode mass flow rate 17 kg·h$^{-1}$; methanol concentration 1M. From Ref. [22] with permission.

Concerning DMFC, to study the effect of low oxidant stoichiometry on the CDD has served to confirm the bifunctional operating regime (BFR) of this type of cell proposed by Ye *et al.* [89] and Ye and Zhao [90]. In this way, it has been found by several authors that the number of current generating (galvanic) zones tends to

increase along with the oxidant stoichiometry, reducing the current consuming, hydrogen generating (electrolytic) zones [11, 18]. Dohle *et al.* [22] investigated the BFR of DMFC for $T_{cell}$ = 70 °C and a methanol mass flow rate of 17 kg·h$^{-1}$ with 1 M concentration. Different air flow rates were used ranging between 0 ≤ $Q_{air}$ ≤ 2000 ml·min$^{-1}$. The CDD was measured at OCV conditions and the location of the hydrogen generating zones was highlighted. More electrolytic zones and higher internal currents were observed at lower $Q_{air}$. Figure 2.13 shows the CDD profile for $Q_{air}$ = 400 ml·min$^{-1}$, which represents the case with maximum internal currents (12 A) reported by these authors.

### 2.4.5. Operating pressure

According to the Nernst equation, improvements in PEMFC performance can be achieved at higher operating pressures [127]. However, in real fuel cell systems exist a trade-off as operating a PEMFC at low (≈ ambient) pressures reduces the parasitic power losses due to fans or compressors. The effect of operating pressure on CDD was studied by Liu *et al.* [33] at different air ($P_{air}$) and $H_2$ ($P_{H2}$) inlet pressures of the reactants. The operating parameters were $T_{cell}$ = $T_{hum,a}$ = $T_{hum,c}$ = 75 °C, $\lambda_{H2}$ = $\lambda_{O2}$ = 2; $P_{air}$ = $P_{H2}$ = 2 bar for the first run and $P_{air}$ = $P_{H2}$ = 3 bar for the second. As expected, the overall performance was slightly lower at $P_{air}$ = $P_{H2}$ = 2 bar. For the lower operating pressure, the CDD profile was progressively more uneven at higher current densities, decreasing from inlet to outlet. The last was attributed to: i) flooding, as more water (≈ 50%) was brought into the cell and ii) reduced oxygen partial pressure along the flow field channel. Similar studies were performed by Ghosh *et al.* [34] and Sun *et al.* [68]. In both cases, increasing the pressure of reactants led to a performance increase in the segments closer to the inlet and to a performance decrease towards the outlet. These authors demonstrated that operating a SFC at higher pressures may not be advantageous as it can lead to a poorer performance of the downstream zones of the flow field.

### 2.4.6. Contaminant species

If PEMFC systems are operated on hydrogen obtained from reformed hydrocarbons (e.g. methane) or alcohols (e.g. methanol), small amounts of CO will be present. In the same way it is accepted that the concentration of CO must not exceed 10 ppm for low temperature operation (<90 °C), otherwise the PEMFC performance will suffer important losses due to poisoning of the Pt electrocatalyst [83].

For some researchers, it has been of interest to study the effect of incorporating small amounts (<100 ppm) of CO, $CO_2$ and $NO_2$ on the hydrogen feed and analyze its effect on the CDD. The addition of these species aims to understand how the deactivation processes of Pt-based catalysts are spatially distributed over the MEA active area as they can be directly related to a decrease in local current density [92]. Tingelöf *et al.* [94] performed CDD measurements in a segmented cell operated on a reformate mix composed by 50% $H_2$, 40% $CO_2$ and 10% $N_2$ at two different CO concentration levels, 10 and 80 ppm. These authors also evaluated the efficiency of air bleeding for CO poisoning mitigation and the CO and $CO_2$ tolerance on Pt-C and PtRu-C catalysts. During the tests, reactants were fed with 100% RH, $\lambda_{H2} = 1.5$, $\lambda_{O2} = 2.4$, $T_{cell} = 60$ °C and ambient pressure. Independently of the catalyst, it took ≈ 60 min for the CDD to reach a steady state when 10 ppm of CO were added to the reformate mix. It was also observed that $CO_2$ does not affect significantly the CDD. To recover from lower CDD profiles, an air bleed level of approximately 0.5% for each 10 ppm of CO was needed during potentiostatic tests at 680 mV - Figure 2.14. Concerning the catalysts, it was found that the CO adsorbed more strongly onto the Pt-C than onto the PtRu-C catalyst. The last effect was strengthened when the cell was operated in potentiostatic mode due to the impossibility of the anodic polarization to reach the required potential for CO oxidation. A similar study was presented by Stumper *et al.* [58] who, operating the segmented cell under very similar conditions, needed approximately 1% of oxygen to recover the previous voltage of the cell after introducing a reformate containing 40 ppm of CO.

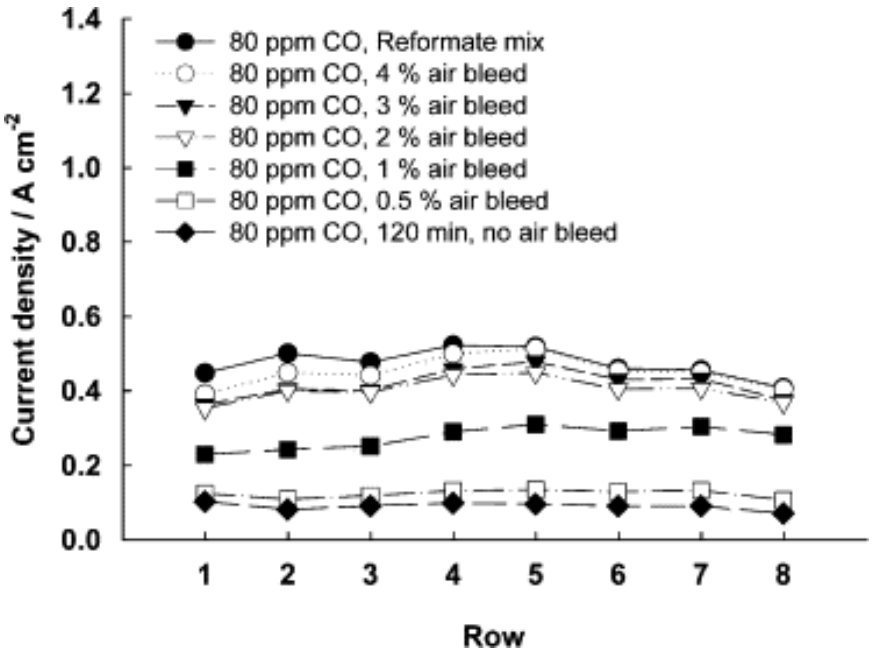


Figure 2.14. Potentiostatic (680 mV) current distribution steady-state of Pt-Ru/C for different levels of air in 80 ppm CO, 50% H2, 40% CO2 and 10% N2 (reformate mix). Stoichiometry cathode 2.4, anode 1.5. Cell temperature 60 °C. RH 100%. Pressure ambient. From Ref. [94] with permission.

St-Pierre *et al.* [112] studied the effect of $NO_2$ on the CDD. For operating conditions: $\lambda_{H2} = 1.6$, $\lambda_{O2} = 2$, $65 \leq T_{cell} \leq 75$ °C and $T_{hum,a} = T_{hum,c} = 72$ °C, the hydrogen gaseous stream was poisoned with 0.01, 0.1 and 0.75 ppm of $NO_2$. It was noted that the CDD varied less than 5% after 55.8 h of operation. The voltage was monitored during the same period time and showed an average decrease of ≈ 40mV. Those authors observed two different trends for the $NO_2$ contamination process, a linear decay in early stages (with an increased slope at higher $NO_2$ concentration levels) followed by a steady-state value reached for a long operating time.

### 2.4.7. Membranes and GDL

In this section is discussed the effect of using membranes or GDL of different types and characteristics on the CDD profile. There are, though, very few studies reporting on this subject. Weng *et al.* [49] studied the transient evolution of the CDD using

Nafion® 112 (thickness = 50.8 µm) and Nafion® 117 (thickness = 175 µm) membranes operated under low RH conditions. The tests involved the use of E-Tek 250-W electrodes. $H_2$ and air were supplied at three RH conditions, 100%, 50% and dry, $\lambda_{H2} = 1.2$, $\lambda_{air} = 2$ and $T_{cell} = 50$ °C. These authors concluded that the Nafion® 112 membrane is more suitable for low RH conditions due to better proton conductivity and more uniform performance at any position of the multiple channels serpentine flow fields. When operated under low RH conditions, Nafion® 117 membrane showed uneven performances along the flow field. Recently, the author of this thesis [55] performed CDD measurements using two different membranes, namely a Nafion® 112 and Fumapen® F-950 both with ≈50 µm thick and similar proton conductivities ≈0.1 S $cm^{-1}$. Similar CDD profiles were obtained for both membranes with current densities between 240 and 390 mA per segment (≈ 1.56 $cm^2$ area) for the Nafion® 112 and between 170 and 375 mA per segment for the Fumapen® F-940. The cell was operated at $T_{cell} = 30$ °C, $Q_{H2} = 200$ ml $min^{-1}$, $Q_{air} = 1500$ ml·$min^{-1}$, dry hydrogen and 95% RH of air. The low current density at the inlet (segment 1, 1) was associated to the drying effect of hydrogen. The low current density towards the outlet was attributed to the lack of hydrogen (starvation effect) as most of the hydrogen was being consumed in the middle segments of the cell. The CDD profiles for both membranes are shown in Figure 2.15.

Hicks *et al.* [10] investigated the effect of three different GDL on the CDD. The GDL selected were made of flexible non-woven, rigid non-woven paper and flexible woven materials, all of them were not segmented. Two air flow rates, 200 and 500 ml·$min^{-1}$, were applied. Other parameters were: $Q_{H2} = 200$ ml·$min^{-1}$, $RH = 90\%$ for both gases and $T_{cell} = 75$ °C. Multiple channels serpentine flow fields were used. The GDL made of rigid non-woven paper showed the most uniform CDD. The rigid non-woven paper and the flexible woven showed very similar and more uniform CDD for the higher air flow rate case. These authors concluded that the impact of GDL on the CDD profile of a SFC is less important than the effect of air flow rate.

a) Nafion® 112

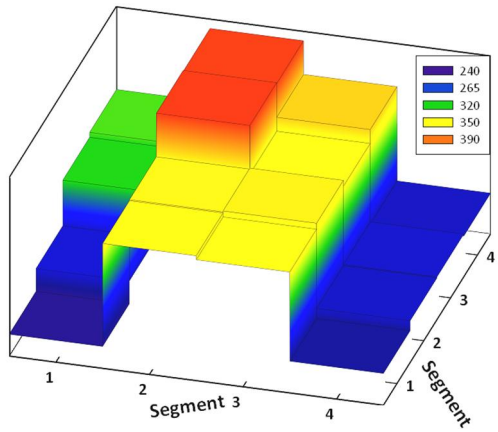


b) Fumapen® F-950

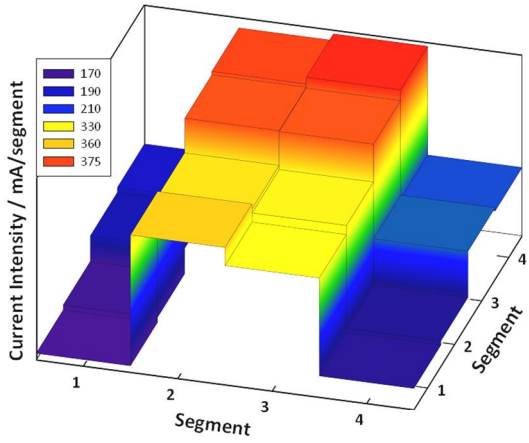


Figure 2.15. Current density distribution profiles for two different MEAs. GDL: ElectroChem® 0.5 mg·cm$^{-2}$ (10% wt. Pt/C). Current density distribution taken at $V_{cell}$=638 mV. Counter flow feeding with $H_2$ inlet at coordinate (1, 1) and outlet at (4, 4). Anode: $H_2$, $Q$ = 200 ml·min$^{-1}$, $P$ = 1.25 bar, dry. Cathode: Air, $Q$ = 1500 ml·min$^{-1}$, $P$ = 1 bar, $RH$ = 95%. $T_{cell}$ = 30 °C

Regarding DMFC, Saarinen *et al.* [91] performed CDD measurements in order to compare two membranes with similar conductivity and different permeation rates to methanol namely, a poly(vinylidene fluoride)-graft-poly(styrene sulfonic acid) (PVDF-g-PSSA) and a Nafion® 117 membrane. The conductivity was 4.5 and 5 S·m$^{-1}$ respectively, while the methanol permeation rate was higher (not specified) for the former. The DMFC was free-breathing type and the MEA was assembled with

commercial electrodes in both cases. For the experiments, 30 ≤$T_{cell}$ ≤ 70 °C, 0.198 ≤$Q_{met}$≤ 7.8 ml·min$^{-1}$ and methanol concentration ranged between 0.5 and 10 M. For methanol concentrations above 3 M more uneven CDD profiles were observed; that was attributed to higher methanol crossover rates. The maximum power densities were observed for the 1 M methanol concentration on both membranes, with no remarkable changes at higher flow rates. However, lower power densities (20-50% less) were observed for the PVDF-g-PSSA membrane.

## 2.5. Integrated analytical techniques

As mentioned before, the simplest way to study the distributed electrochemical performance over the MEA active area is to measure the CDD. Nonetheless, complementary analytical techniques that permit the distributed measurement of gas composition analysis, water accumulation, temperature, HFR and EIS have been successfully integrated in SFC, allowing researchers to obtain further understanding of PEMFC systems.

Table 3 - References using complementary analytical techniques in SFC for distributed analysis.

| Experimental technique | | References |
|---|---|---|
| Gas composition analysis ($H_2$, $O_2$, $H_2O$) | | [101, 32, 78, 79, 102, 21, 50,] |
| Water accumulation | Direct liquid water visualization techniques | [31, 19, 44, 80] |
| | Neutron radiography | [115, 25, 74, 107] |
| Temperature distribution | | 10, 11, 16, 44, 80, 53, 69, 64] |
| HFR | | 8, 25, 28, 32, 48, 53, 59, 78, 79, 80 81 |
| EIS | | 46, 49, 61, 73, 74, 75, 76, 77 |

The importance of combining CDD measurements with the analytical techniques presented in this section relies on the fact that the performance of PEMFC is hardly influenced by the complex interaction of the parameters previously mentioned. Table 3 summarizes the analytical techniques that have been combined with CDD measurements.

It is important to highlight that, the integration of distributed HFR and EIS was first reported by Cleghorn et al [8] and Brett *et al.* [61] using the PCB technique. As it is beyond the scope of this work only the combination of local EIS with a water accumulation technique is presented below.

### 2.5.1. Gaseous species distribution

The measurement of local gaseous species along the flow field channels of SFC provides important information about the concentration of reactant species and water vapor inside the cell (e.g. to track the oxygen depletion and water formation along the channels). Mench and Wang from the Pennsylvania State University used gas chromatography to measure the steady-state [102] and real-time [78, 79] distribution of $H_2$, $O_2$, $N_2$ and water vapor in a SFC. To do that, 16 extraction ports (8 per electrode) equally spaced along the serpentine flow field of single channel were created. The extraction ports were connected to a GC for analysis during steady state operation. In a similar form, the extraction ports were connected to a real-time gas analyzer for transient analyses. The sampling flow rate needed for this analyzer was less than 3% of the flowing stream in the channel. In a following report [50], these authors calculated local values of the net water transport coefficient across the membrane ($\alpha$). The coefficient was calculated from CDD measurement and local molar fraction of water in the anode. Figure 2.16 depicts the different values obtained for $\alpha$; positive values mean a net transport of water from the anode to the cathode. In other words, positive values of $\alpha$ mean that the electro-osmotic drag (EOD) of water is the dominant water transport mechanism across the membrane while negative values mean that the water back diffusion dominates over the EOD.

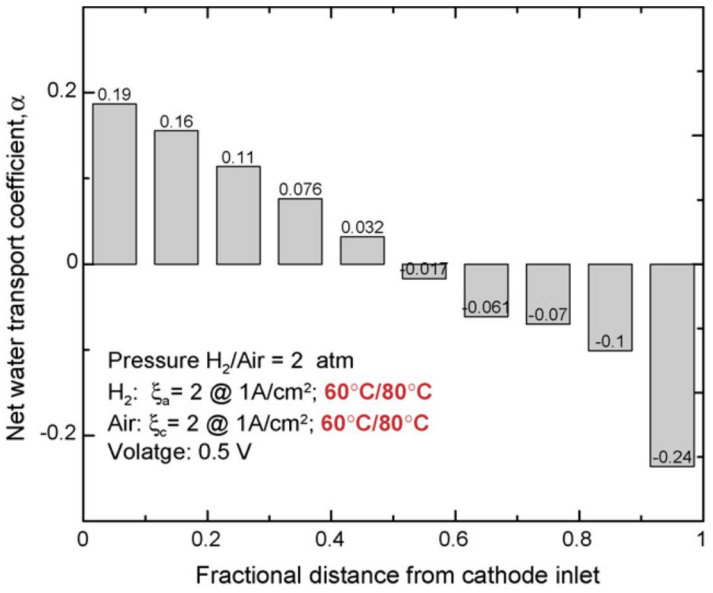


Figure 2.16. Net water transport coefficient profile for the humidifier temperature of 60 °C in both anode and cathode. The cell temperature is 80 °C. From Ref. [50] with permission.

Nishikawa *et al.* [21] performed local RH and CDD measurements in cell with three segments. RH was measured by drilling six 1 mm diameter holes in the cathodic flow field. To each of these six holes it was then connected a RH probe. The operating conditions were: $T_{cell} = T_{hum,a} = 80$ °C and $40 \leq T_{hum,c} \leq 70$ °C. For $T_{hum,c} = 40$ °C the *RH* of air at the inlet was 30%. However, from the RH measurements it was observed a gradual increase up to 70% towards the outlet, highlighting the large difference that can appear even at relatively small current densities ($\approx 0.150$ mA·cm$^{-2}$). The CDD measurements started at $T_{hum,c} = 70$ °C which gradually decreased to $T_{hum,c} = 40$ °C. The results were in accordance with the local RH measurements showing an increasingly better performance for the downstream segment when $T_{hum,c} = 40$ °C and the local RH difference between the inlet and the outlet was larger.

### 2.5.2. Condensed water accumulation

To correlate the liquid water distribution with the local electrochemical performance segmented cells, it is important to use tools that allow researchers to have an idea about the actual liquid water accumulation state at the gas channels, mainly at the cathode. The easiest way to monitor the water accumulation is by disassembling the

SFC after a certain period of operation [19]; however, this technique is time consuming and not quantitative. The direct observation of condensed water accumulation at the gas channels of operating SFC can be achieved by using transparent materials for pertinent PEMFC components. Then, a coupled charge device (CCD) camera [44, 80] or a digital camera [31, 53] can be used to observe the water accumulation inside the flow fields.

Neutron radiography (NR) is a sophisticated technique to visualize the distribution of water in PEMFC. A review of the use of NR for water visualization in PEMFC was recently presented by Mukundan and Borup [106]. When implemented in SFC, the materials used in the cell must have improved neutron transparency [25]. Schneider *et al.* [74] performed simultaneous local EIS and NR in a 29.2 $cm^2$ active area PEMFC operating on pure $H_2$ and $O_2$. Three technical modifications were made to ensure high neutron transparency, i) the endplates were fabricated of 3 cm thick gold plated aluminum blocks, ii) the cathode current collector was built in anodized aluminum plate and iii) graphite flow fields thickness was reduced to 2 mm for the anode and 3 mm for the segmented cathode to minimize attenuation of the neutron beam by this material.

Figure 2.17 depicts the main results obtained. It was observed that under low humidity conditions, simultaneous severe drying zones at the inlet and flooded zones at the outlet can appear when operating a PEMFC in co-flow mode. This has also been reported by other authors in counter flow mode [37]. The combination of NR and CDD measurements showed a partially flooded transition zone between undersaturated and completely flooded parts of the cell. From the local EIS measurements it was concluded that near the inlet, poor interfacial kinetics due to drying of the ionomer at the catalyst layer of the electrodes might exceed the impact of increased membrane resistance.

Recently, Schröder *et al.* [107] performed for the first time NR and CDD measurements DMFC. These authors concluded that it is possible to correlate the production of water and $CO_2$ at the cathode of DMFC using NR and CDD distribution measurements.

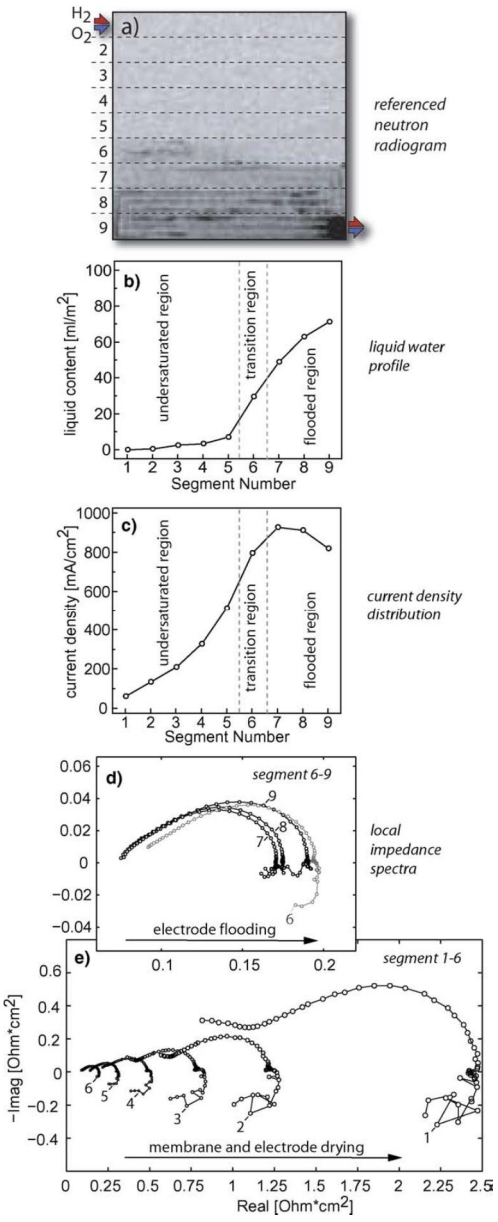


Figure 2.17. Results in co-flow mode: $T_{cell}$ = 70 °C, $I_{cell}$ = 14.6 A, $A_{cell}$ =29.2 cm$^2$, $\lambda_{H2}$ = $\lambda_{O2}$ = 1.5, $RH_{H2}$= 40%, dry $O_2$, $f_{mod}$ = 10 mHz to 10 kHz, Nafion® 112 membrane, ETEK ELAT V3.1 electrodes, 250 µm PTFE gaskets (numbers denote segment). From Ref. [74] with permission.

### 2.5.3. Temperature distribution

By mapping the temperature distribution along the MEA active area, it is possible to locate the zones with higher electrochemical activity as the local heat generation increases with current density according to Joule´s laws [105]. Hakenjos *et al.* [44] performed temperature distribution measurements by placing a zinc selenide window (transparent to infrared and visible light) immediately after the cathodic flow field. The temperature distribution measurements were performed with an infrared camera. The operating conditions were $250 \leq Q_{air} \leq 750$ ml·min$^{-1}$, $T_{cell} = T_{hum,c} = 23$ °C and $Q_{H2} = 100$ ml·min$^{-1}$, dry. At the highest air flow rate, no liquid water was observed, in this case it was verified a direct correspondence between local temperature and local current densities. On the contrary, these authors observed areas with higher temperature and lower current density in flooded zones of the cell at lower air flow rates (250 and 500 ml·min$^{-1}$). In these cases, the condensed water led to lower current densities by hindering the gas transport through the porous media of the GDL and covering the catalyst active sites. The higher temperatures in flooded zones were attributed to the water condensation enthalpy.

Maranzana *et al.* [53], measured the local temperature using 20 thermocouples (one per segment) inserted into a rib channel at different positions of the cathode flow field. They observed a rise in temperature near the inlet when hydrogen was fed to the cell at OCV condition. The rise was attributed to internal currents of nominal value up to 0.4 A·cm$^{-2}$ generated by the simultaneous oxidation of hydrogen and residual oxygen (present in the flow field before hydrogen being fed to the cell) at the anode - Figure 2.18.

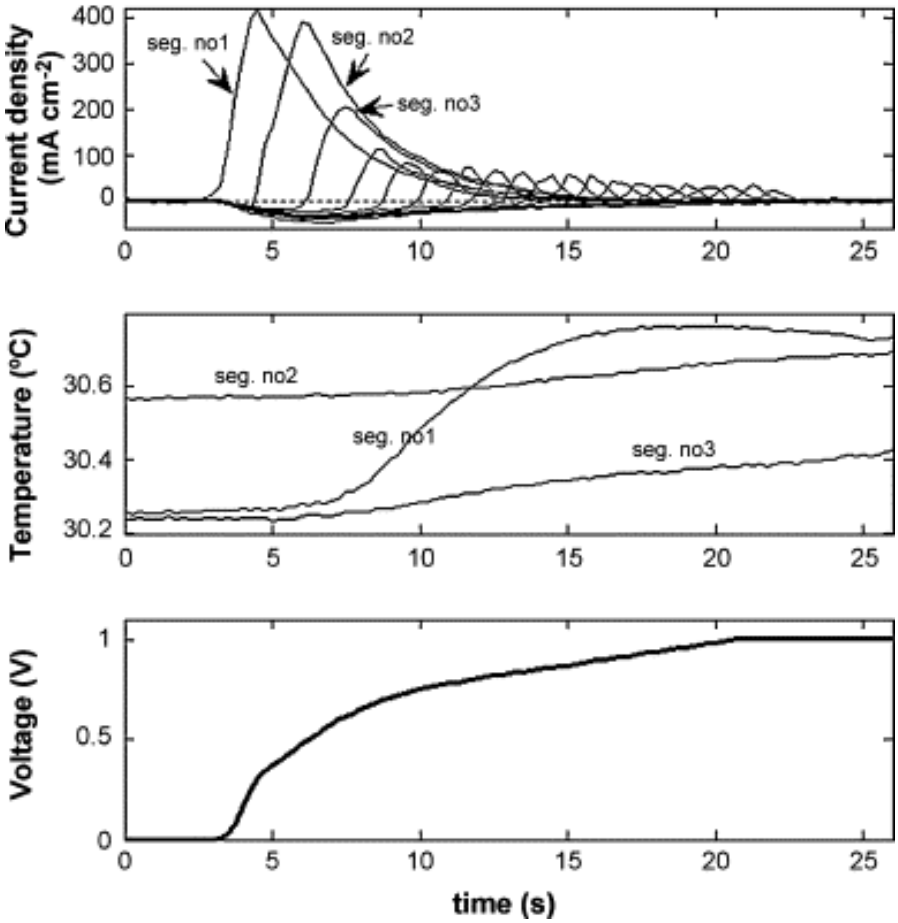


Figure 2.18. Voltage rise and evolutions of local temperatures and current densities when hydrogen is introduced in an anode full of air (fuel cell at open circuit). From Ref. [53] with permission.

## 2.6. High temperature SFC

As stated in Chapter 1, high temperature PEMFC (HT-PEMFC) operate in a temperature range between 120-200 °C. Some efforts have been done in order to analyze the distributed performance of HT-PEMFC. Lobato et al. [122] inserted a sensor plate at the back of the cathode flow field to measure the current density distribution in HT-PEMFC with different flow fields. The plate consisted of a PCB with embedded current sensors. The cell was operated at 125 °C and four different flow field geometries tested: four step serpentine, net/grid, multiple channels parallel and

interdigitated. Those authors suggested that that flow fields with net/grid geometries could be used when working at high temperature without expecting lower performance. Boaventura et al. [123] used a segmented of the resistors network approach with a segmented anode in order to study the influence of CO (1.5% and 3%) on the current density distribution at 160 °C and 180 °C. The anode flow field has net/grid geometry. It was found that CO causes a performance loss, which is worsened for higher CO concentrations and current densities and for lower temperatures. Those authors observed that introducing CO results in a heterogeneous behavior across the MEA, which is aggravated by the increase of CO concentration and global current density.

## 2.7. Conclusions

The performance of PEMFC is uneven over the MEA active area and depends on a complex interaction of various design, assembling and operating parameters as well as on the properties and microstructure of the materials used. To the date, SFC have proven to be an excellent diagnostic tool that permits further understanding of the local electrochemical performance in single cells and stacks.

SFC can be classified accordingly to common structural concepts in: printed circuit board, resistors network and Hall effect sensors. The Hall effect sensors technique can be considered as the most accurate for local electrochemical characterization, due to the possibility of calibration of these current sensing devices, followed by the resistors network and the PCB. The accuracy of the electrochemical measurements can be improved significantly by segmenting the GDL, the BP and the CC. The PCB technique is the most suitable for use in middle cells of PEMFC stacks as it offers the possibility of incorporating the segmented flow fields of adjacent cells.

CDD measurements have been crucial to understand the effect of flow field geometry, clamping pressure, reactants relative humidity and flow rate, operating pressure, contaminant species, membrane thickness and GDL on the performance of PEMFC. Despite its importance concerning fuel cells durability, there is a lack of literature describing suitable strategies to homogenize the CDD in PEMFC systems.

Regarding DMFC, CDD measurements have been especially important to confirm the simultaneous existence of electrolytic and galvanic operating regions showed by this type of cell at low oxidant stoichiometric rates.

The integration of various analytical techniques that allow: i) $H_2$, $O_2$, $N_2$ and $H_2O$ distribution determination, ii) condensed water distribution evaluation, iii) temperature distribution and iv) local high frequency resistance (HFR) and local electrochemical impedance spectroscopy (EIS) analysis have been reported. These techniques provide important information that complements the CDD measurements.

PEMFC *in situ* diagnostic methods need to be improved and standardized as they should play a key role in the massive commercialization of PEMFC systems. In this way, SFC can be used to optimize PEMFC systems as they provide fast and reliable *in situ* measurements that allow to evaluate how the interaction of different parameters affect the local performance and degradation. Furthermore, SFC have been used with HT-PEMFC components and operating conditions to study the effect of flow field geometry and CO on the CDD of this type of cells.

Present applications of SFC include the diagnosis of PEMFC components manufacturing defects of [120] and the study of PEMFC distributed startup at sub-zero temperatures [121].

## 2.7. Acknowledgments

Luis C. Pérez is grateful to FCT for his PhD grant reference SFRH/BD/44684/2008. Lúcia Brandão is also thankful to FCT for her post-doc grant (SFRH/BPD/41233/2007). Financial support by FCT through the project PTDC/EQU-EQU/70574/2006 is also acknowledged.

## 2.8. References

[1] L. Carrette, K.A. Friedrich, U. Stimming, Chemphyschem 1 (2000) 162-193.

[2] J.D. Holladay, J. Hu, D.L. King, Y. Wang, Catal. Today 139 (2009) 244-260.

[3] E. David, J. of Mater. Process. Technolog. 162-163 (2005) 169-177.

[4] P. Agnolucci, Int. J. of Hydrogen Energy 32 (2007) 3526-3544.

[5] J.-H. Wee, Renew. and Sustain. Energy Rev. 11 (2007) 1720-1738.

[6] S. G. Kandlikar, Z. Lu, J. of Fuel Cell Sci. and Technol. 6 (2009) 044001.

[7] Bruijn F., PEM Fuel Cells for Transport Applications: State of the Art and Challenges, in: L.T. Handoko, R.T.S. Masbah (Eds.), AIP, 2009, pp. 3-12.

[8] S.J.C. Cleghorn, C.R. Derouin, M.S. Wilson, S. Gottesfeld, J. of Appl. Electrochem. 28 (1998) 663-672.

[9] N. Rajalakshmi, M. Raja, K.S. Dhathathreyan, J. of Power Sources 112 (2002) 331-336.

[10] M. Hicks, K. Kropp, A. Schmoeckel, R. Atanasoski, ECS Trans. 1 (2006) 605-612.

[11] D.U. Sauer, T. Sanders, B. Fricke, T. Baumhöfer, K. Wippermann, A.A. Kulikovsky, H. Schmitz, J. Mergel, J. of Power Sources 176 (2008) 477-483.

[12] G. Bender, M.S. Wilson, T.A. Zawodzinski, J. of Power Sources 123 (2003) 163-171.

[13] X. Z. Yuan, H. J. Wang, J. C. Sun, J. J. Zhang, Int. J. of Hydrogen Energy, 32 (2007) 4365-4380.

[14] J.F. Wu, X.Z. Yuan, H.J. Wang, M. Blanco, J.J. Martin, J.J. Zhang, Int. J. of Hydrogen Energy 33 (2008) 1747-1757.

[15] C.-Y. Wang, Chem. Rev. 104 (2004) 4727-4766.

[16] A.M. Abdullah, T. Okajima, A.M. Mohammad, F. Kitamura, T. Ohsaka, J. of Power Sources 172 (2007) 209-214.

[17] S.A. Freunberger, M. Reum, A. Wokaun, F.N. Büchi, Electrochem. Commun. 8 (2006) 1435-1438.

[18] A.A. Kulikovsky, H. SchrnitZ, K. Wippermann, J. Mergel, B. Fricke, T. Sanders, D.U. Sauer, Electrochem. Commun. 8 (2006) 754-760.

[19] S.S. Hsieh, Y.J. Huang, J. of Power Sources 183 (2008) 193-204.

[20] C. Wieser, A. Helmbold, E. Gulzow, J. of Appl. Electrochem. 30 (2000) 803-807.

[21] H. Nishikawa, R. Kurihara, S. Sukemori, T. Sugawara, H. Kobayasi, S. Abe, T. Aoki, Y. Ogami, A. Matsunaga, J. of Power Sources 155 (2006) 213-218.

[22] H. Dohle, J. Mergel, P.C. Ghosh, Electrochimica Acta 52 (2007) 6060-6067.

[23] J. LaDou, Int. J. of Hyg. and Environ. Health 209 (2006) 211-219.

[24] M. Schulze, E. Gulzow, S. Schonbauer, T. Knori, R. Reissner, J. of Power Sources 173 (2007) 19-27.

[25] J.J. Gagliardo, J.P. Owejan, T.A. Trabold, T.W. Tighe, Nucl. Instrum. and Methods in Phys. Res. Sect. A: Accel., Spectrom., Detect. and Assoc. Equip. 605 (2009) 115-118.

[26] D.J.L. Brett, S. Atkins, N.P. Brandon, V. Vesovic, N. Vasileiadis, A.R. Kucernak, Electrochem. Commun. 3 (2001) 628-632.

[27] D.G. Strickland, S. Litster, J.G. Santiago, J. of Power Sources 174 (2007) 272-281.

[28] Y. Morimoto, T. Suzuki and H. Yamada, Electrochem. Soc. Proc. Volume 2002-31 248-256.

[29] M. Noponen, T. Mennola, M. Mikkola, T. Hottinen, P. Lund, J. of Power Sources 106 (2002) 304-312.

[30] J. Benziger, J.E. Chia, E. Kimball, I.G. Kevrekidis, J. of the Electrochem. Soc. 154 (2007) B835-B844.

[31] Y. Tabe, K. Kikuta, T. Chikahisa, M. Kozakai, J. of Power Sources 193 (2009) 416-424.

[32] T. Araki, H. Koori, T. Taniuchi, K. Onda, J. of Power Sources 152 (2005) 60-66.

[33] Z. Liu, Z. Mao, B. Wu, L. Wang, V.M. Schmidt, J. of Power Sources 141 (2005) 205-210.

[34] P.C. Ghosh, T. Wuster, H. Dohle, N. Kimiaie, J. Mergel, D. Stolten, J. of Power Sources 154 (2006) 184-191.

[35] F. Ay, A. Ata, H. Dohle, T. Sener, H. Gorgun, J. of Power Sources 167 (2007) 391-397.

[36] M.M. Mench, C.Y. Wang, M. Ishikawa, J. of the Electrochem. Soc. 150 (2003) A1052-A1059.

[37] S. Yoshioka, A. Yoshimura, H. Fukumoto, O. Hiroi, H. Yoshiyasu, J. of Power Sources 144 (2005) 146-151.

[38] Bansal R., Fundamentals of engineering electromagnetics, Taylor & Francis Group, Florida, 2006.

[39] http://content.honeywell.com/sensing/prodinfo/solidstate/technical/chapter2.pdf retrieved on February 2010.

[40] D. Liang, Q. Shen, M. Hou, Z. Shao, B. Yi, J. of Power Sources 194 (2009) 847-853.

[41] M. Santis, S.A. Freunberger, M. Papra, A. Wokaun, F.N. Büchi, J. of Power Sources 161 (2006) 1076-1083.

[42] P.C. Rieke, N.E. Vanderborgh, J. of the Electrochem. Soc. 134 (1987) 1099-1104.

[43] J.J.T.T. Vermeijlen, L.J.J. Janssen, A.J. Geurts, G.C. Haastrecht, J. of Appl. Electrochem. 25 (1995) 1122-1127.

[44] A. Hakenjos, H. Muenter, U. Wittstadt, C. Hebling, J. of Power Sources 131 (2004) 213-216.

[45] D. Natarajan, T. Van Nguyen, Aiche J. 51 (2005) 2587-2598.

[46] I.A. Schneider, H. Kuhn, A. Wokaun, G.G. Scherer, J. of the Electrochemical Society 152 (2005) A2092-A2103.

[47] A.B. Geiger, R. Eckl, A. Wokaun, G.G. Scherer, J. of the Electrochem. Soc. 151 (2004) A394-A398.

[48] A. Hakenjos, K. Tüber, J.O. Schumacher, C. Hebling, Fuel Cells 4 (2004) 185-189.

[49] F.B. Weng, B.S. Jou, C.W. Li, A. Su, S.H. Chan, J. of Power Sources 181 (2008) 251-258.

[50] G.Q. Lu, F.Q. Liu, C.Y. Wang, J. of Power Sources 164 (2007) 134-140.

[51] D. Natarajan, T. Van Nguyen, J. of Power Sources 135 (2004) 95-109.

[52] J.J. Hwnag, W.R. Chang, R.G. Peng, P.Y. Chen, A. Su, Int. J. of Hydrogen Energy 33 (2008) 5718-5727.

[53] G. Maranzana, O. Lottin, T. Colinart, S. Chupin, S. Didierjean, J. of Power Sources 180 (2008) 748-754.

[54] Y.G. Yoon, W.Y. Lee, T.H. Yang, G.G. Park, C.S. Kim, J. of Power Sources 118 (2003) 193-199.

[55] Martínez, L. C., Brandão, L., Sousa, J. M., Mendes, A., "PEMFC study using a segmented fuel cell", HYCELTEC 2009 – II Iberian Symposium on Hydrogen, Fuel Cells and Advanced Batteries, Vila Real, Portugal, 13-17 Setembro de 2009, ref. P19-SA

[56] R. Eckl, R. Grinzinger, W. Lehnert, J. of Power Sources 154 (2006) 171-179.

[57] F.N. Büchi, A.B. Geiger, R.P. Neto, J. of Power Sources 145 (2005) 62-67.

[58] J. Stumper, S.A. Campbell, D.P. Wilkinson, M.C. Johnson, M. Davis, Electrochimica Acta 43 (1998) 3773-3783.

[59] M. Noponen, J. Ihonen, A. Lundblad, G. Lindbergh, J. of Appl. Electrochem. 34 (2004) 255-262.

[60] Z. Siroma, N. Fujiwara, T. Loroi, S. Yamazaki, H. Senoh, K. Yasuda, K. Tanimoto, J. of Power Sources 172 (2007) 155-162.

[61] D.J.L. Brett, S. Atkins, N.P. Brandon, V. Vesovic, N. Vasileiadis, A. Kucernak, Electrochem. and Solid State Lett. 6 (2003) A63-A66.

[62] M. V. Santis, Investigations of Current Density Inhomogeneities in Polymer Electrolyte Fuel Cells, PhD thesis, Swiss Federal Institute of Technology Zurich, 2006

[63] D. Candusso, J.P. Poirot-Crouvezier, B. Bador, E. Rullière, R. Soulier, J.Y. Voyant, Eur. Phys. J. Appl. Phys. 25 (2004) 67-74.

[64] S. Sailler, S. Rosini, M.A. Chaib, J.Y. Voyant, Y. Bultel, F. Druart, P. Ozil, J. of Appl. Electrochem. 37 (2007) 161-171.

[65] N.B. Felix, R. Mathias, Meas. Sci. and Technol. 19 (2008) 085702.

[66] S.A. Freunberger, M. Reum, J. Evertz, A. Wokaun, F.N. Buchi, J. of the Electrochem. Soc. 153 (2006) A2158-A2165.

[67] L. Wang, H. Liu, J. of Power Sources 180 (2008) 365-372.

[68] H. Sun, G. Zhang, L.-J. Guo, H. Liu, J. of Power Sources 158 (2006) 326-332.

[69] M. Wilkinson, M. Blanco, E. Gu, J.J. Martin, D.P. Wilkinson, J.J. Zhang, H. Wang, Electrochem. and Solid State Lett. 9 (2006) A507-A511.

[70] J.R. Claycomb, A. Brazdeikis, M. Le, R.A. Yarbrough, G. Gogoshin, J.H. Miller, Appl. Superconductivity, IEEE Transactions on 13 (2003) 211-214.

[71] H. Yang, J. Chen, S. Wang, C. Chen, J. Jeng, J. Chen, C. Wu, S. Liao, H. Horng, Tamkang J. of Sci. and Eng., 6 (2003) 9-18.

[72] K.H. Hauer, R. Potthast, T. Wuster, D. Stolten, J. of Power Sources 143 (2005) 67-74.

[73] D.J.L. Brett, S. Atkins, N.P. Brandon, N. Vasileiadis, V. Vesovic, A.R. Kucernak, J. of Power Sources 172 (2007) 2-13.

[74] I.A. Schneider, D. Kramer, A. Wokaun, G.G. Scherer, Electrochem. Commun. 7 (2005) 1393-1397.

[75] I.A. Schneider, S.A. Freunberger, D. Kramer, A. Wokaun, G.G. Scherer, J. of the Electrochem. Soc. 154 (2007) B383-B388.

[76] I.A. Schneider, D. Kramer, A. Wokaun, G.G. Scherer, J. of the Electrochem. Soc. 154 (2007) B770-B782.

[77] S.A. Freunberger, I.A. Schneider, P.-C. Sui, A. Wokaun, N. Djilali, F.N. Buchi, J. of the Electrochem. Soc. 155 (2008) B704-B714.

[78] Q. Dong, J. Kull, M.M. Mench, J. of Power Sources 139 (2005) 106-114.

[79] Q. Dong, M.M. Mench, S. Cleghorn, U. Beuscher, J. of the Electrochem. Soc. 152 (2005) A2114-A2122.

[80] W.H.J. Hogarth, J. Steiner, J.B. Benziger, A. Hakenjos, J. of Power Sources 164 (2007) 464-471.

[81] N. Holmstrom, J. Ihonen, A. Lundblad, G. Lindbergh, Fuel Cells 7 (2007) 306-313.

[82] M. Reum, S.A. Freunberger, A. Wokaun, F.N. Buchi, J. of the Electrochem. Soc. 156 (2009) B301-B310.

[83] J. Larmaine, A. Dicks, Fuel cell systems explained, 2nd ed., West Sussex (2003).

[84] H. Sun, G. Zhang, L.-J. Guo, S. Dehua, H. Liu, J. of Power Sources 168 (2007) 400-407.

[85] H. Sun, G. Zhang, L. Guo, H. Liu, Int. J. of Hydrogen Energy 34 (2009) 5529-5536.

[86] P.C. Ghosh, T. Wuster, H. Dohle, N. Kimiaie, J. Mergel, D. Stolten, J. of Fuel Cell Sci. and Technol. 3 (2006) 351-357.

[87] A. Taniguchi, T. Akita, K. Yasuda, Y. Miyazaki, J. of Power Sources 130 (2004) 42-49.

[88] Z.X. Liu, L.Z. Yang, Z.Q. Mao, W.L. Zhuge, Y.J. Zhang, L.S. Wang, J. of Power Sources 157 (2006) 166-176.

[89] Q. Ye, T.S. Zhao, H. Yang, J. Prabhuram, Electrochem. and Solid-State Lett. 8 (2005) A52-A54.

[90] Q. Ye, T.S. Zhao, J. of the Electrochem. Soc. 152 (2005) A2238-A2245.

[91] V. Saarinen, O. Himanen, T. Kallio, G. Sundholm, K. Kontturi, J. of Power Sources 163 (2007) 768-776.

[92] G. Bender, T. Zawodsinski, Electrochem. Soc. Proc. Volume 2002-31 212-218.

[93] D.J.L. Brett, S. Atkins, N.P. Brandon, V. Vesovic, N. Vasileiadis, A.R. Kucernak, J. of Power Sources 133 (2004) 205-213.

[94] T. Tingelöf, L. Hedström, N. Holmström, P. Alvfors, G. Lindbergh, Int. J. of Hydrogen Energy 33 (2008) 2064-2072.

[95] G. Zhang, B. Ma, D. Shang, L. Guo, H. Sun, H. Liu, ECS Trans. 11 (2007) 1545-1552.

[96] E. Gülzow, T. Kaz, R. Reissner, H. Sander, L. Schilling, M. v.Bradke, J. of Power Sources 105 (2002) 261-266.

[97] G.S. Zhang, L.J. Guo, B. Ma, H.T. Liu, J. of Power Sources 188 (2009) 213-219.

[98] T. Mennola, M. Noponen, T. Kallio, M. Mikkola, T. Hottinen, J. of Appl. Electrochem. 34 (2004) 31-36.

[99] I. Nitta, T. Hottinen, O. Himanen, M. Mikkola, J. of Power Sources 171 (2007) 26-36.

[100] M.M. Mench, C.Y. Wang, J. of the Electrochem. Soc. 150 (2003) A79-A85.

[101] M.M. Mench, Q.L. Dong, C.Y. Wang, J. of Power Sources 124 (2003) 90-98.

[102] X.G. Yang, N. Burke, C.Y. Wang, K. Tajiri, K. Shinohara, J. of the Electrochem. Soc. 152 (2005) A759-A766.

[103] E. Stumper, M. Lohr, S. Hamada, J. of Power Sources 143 (2005) 150-157.

[104] B. Sompalli, B.A. Litteer, W. Gu, H.A. Gasteiger, J. of the Electrochem. Soc. 154 (2007) B1349-B1357.

[105] M.H. Wang, H. Guo, C.F. Ma, J. of Power Sources 157 (2006) 181-187.

[106] R. Mukundan, R.L. Borup, Fuel Cells 9 (2009) 499-505.

[107] A. Schröder, K. Wippermann, J. Mergel, W. Lehnert, D. Stolten, T. Sanders, T. Baumhöfer, D.U. Sauer, I. Manke, N. Kardjilov, A. Hilger, J. Schloesser, J. Banhart, C. Hartnig, Electrochem. Comm. 11 (2009) 1606-1609.

[108] D. Natarajan, T. Van Nguyen, Aiche J. 51 (2005) 2599-2608.

[109] P. Berg, K. Promislow, J. Stumper, B. Wetton, J. of Fuel Cell Sci. and Technol. 2 (2005) 111-120.

[110] M. Reum, A. Wokaun, F.N. Büchi, J. of the Electrochem. Soc. 156 (2009) B1225-B1231.

[111] http://www.splusplus.com/ retrieved on February 2010

[112] J. St-Pierre, N. Jia, R. Rahmani, J. of the Electrochem. Soc. 155 (2008) B315-B320.

[113] A.A. Kulikovsky, A. Kucemak, A.A. Kornyshev, Electrochimica Acta 50 (2005) 1323-1333.

[114] D.J.L. Brett, P. Aguiar, N.P. Brandon, A.R. Kucernak, Int. J. of Hydrogen Energy 32 (2007) 863-871.

[115] C. Hartnig, I. Manke, N. Kardjilov, A. Hilger, M. Grünerbel, J. Kaczerowski, J. Banhart, W. Lehnert, J. of Power Sources 176 (2008) 452-459.

[116] M. Noponen, T. Hottinen, T. Mennola, M. Mikkola, P. Lund, J. of Appl. Electrochem. 32 (2002) 1081-1089.

[117] T. Hottinen, M. Noponen, T. Mennola, O. Himanen, M. Mikkola, P. Lund, J. of Appl. Electrochem. 33 (2003) 265-271.

[118] http://helmbold-messtechnik.de/ retrieved on February 2010

[119] M. Santis, S.A. Freunberger, A. Reiner, F.N. Büchi, Electrochimica Acta 51 (2006) 5383-5393.

[120] G. Bender, T.V. Reshetenko, H. Dinh, M. Ulsh, R. Rocheleau, ECS Meet. Abstr. 802 (2008) 944.

[121] T. Colinart, F.N. Buchi, ECS Meet. Abstr. 902 (2009) 1015.

[122] J. Lobato, P. Cañizares, M.A. Rodrigo, F.J. Pinar, D. Úbeda, J. Power Sources, 196 (2011) 4209-4217.

[123] M. Boaventura, H. Sander, K.A. Friedrich, A. Mendes, Electrochimica Acta, 56 (2011) 9467-9475.

# Chapter III

# Chapter III - Water management studies[2]

## 3.1. Abstract

Adequate water management is crucial to increase stability and durability of Polymer Electrolyte Membrane Fuel Cells. In this paper, a test rig suitable for water balance and nitrogen crossover studies was built around a hydrogen-air segmented cell and used to indirectly assess flooding or drying conditions in specific zones of the active cell area. In particular, the anode of the segmented cell was operated in recirculation mode with continuous water removal. Current density distribution diagrams were obtained for different anode operating parameters, namely, the recirculated gas flow rate, anode pressure and time between purges. Water accumulation at the electrodes was assessed from current density distribution diagrams and confirmed using water balance and flow-patterns calculations. It was concluded that lower recirculation flow rates led to flooding due to decreased water removal capabilities at the anode. For higher recirculation flow rates, drying was observed in one zone of the cell but homogeneous current density distribution in the other. Finally, the use of partially segment bipolar plates was proposed to increase the in-plane electrical resistance between adjacent segments. The partial segmentation increased the segment to segment in-plane electrical resistance between 14% and 21% and decreased the through-plane to in-plane resistance ratio by 17%.

[2] The content of this chapter is adapted from: Pérez, L. C., Ihonen, J., Sousa, J. M., and Mendes, A., 2013, "Use of Segmented Cell Operated in Hydrogen Recirculation Mode to Detect Water Accumulation in PEMFC," Fuel Cells, 13(2), pp. 203-216.

## 3.2. Introduction

The implementation of adequate water management strategies is crucial to increase the stability and durability of Polymer Electrolyte Membrane Fuel Cells (PEMFCs) [1]. At PEMFCs operating temperatures, normally below 80 °C, water may coexist in gas and liquid phase in different components of the cell such as the catalyst layers (CLs), the gas diffusion layers (GDLs), the microporous layers (MPLs) and the gas flow channels.

On the one hand, the accumulation of liquid water restricts the availability of reactants at the electrodes, leading to an immediate loss of performance and degradation of the CLs in the long-term [2]. The blockage of the reactants' distribution paths due to liquid water accumulation is generically referred to as flooding [1]. However, differences in the geometric scale and structure of the components, which lead to different water transport mechanisms [3] within them, have made required specifying whether water accumulation occurs at the CLs, GDLs and MPLs or at the gas flow channels. The terms "clogging" [4] and "plugging" [5] have been used to describe water accumulation in the gas flow channels, while the term flooding has been used to describe water accumulation at the CLs, GDLs or MPLs. On the other hand, once the proton conductivity of the membrane depends on its water content [6], the water removal mechanisms are relevant to prevent the membrane drying [7].

Due to the possibility of local flooding and drying conditions occurring simultaneously [8], it is important to study the spatial distribution of water along the active cell area. By investigating the spatial distribution of water, it is possible to identify the water transport mechanisms dominating different zones of the cell. Water distribution can be studied using different *in situ* techniques, namely, neutron radiography [9] and synchrotron X-ray imaging [10], which involves equipment not widely available; transparent cells [11], that are useful to study water in the flow fields; soft X-ray microscopy [12], which need substitution of PEMFC components; and magnetic

resonance [13], which may lead to problems controlling the PEMFC operating conditions.

Two recent review articles reported the water transport mechanisms [3] and *in situ* experimental diagnostics [14] concerning PEMFC research. Both articles suggested that experimental capabilities have been overpassed by numerical approaches, paving the way to refine existing experimental techniques. In recent years, segmented PEMFCs (SFC) have been used to study the effect of different parameters on the distributed performance of single cells and stacks. In Chapter 2 [15] a literature review article addressing the SFC approaches, the effect of different parameters on the current density distribution (CDD) and complementary analytical techniques coupled to different SFC setups. That paper highlighted how local flooding or drying zones of the membrane-electrode assembly's (MEA) active area can be indirectly assessed from the spatial distribution of the electrochemical activity depicted on CDD diagrams.

In the present study, a segmented PEMFC with a technically-relevant fuel delivery configuration is used to indirectly assess flooding or drying zones of the MEA. Particularly, the anode of the segmented PEMFC is operated in recirculation mode [16] with continuous anode water removal, similar to actual residential [17] and automotive [18] PEMFC systems. The segmented PEMFC is assembled with partially segmented bipolar plates (BPs) to reduce current spreading [19] between segments. Further, the segmented PEMFC is tested on an experimental test rig suitable for water balance [20] and nitrogen crossover and accumulation [21] studies that is properly described and documented.

## 3.3. Experimental

### 3.3.1. Test rig for studying water balance, nitrogen crossover and distributed performance

Figure 3.1 shows a schematic of the test rig. The anode was fed with high purity hydrogen (amount of impurities: $H_2O$ < 3 ppm, $O_2$ < 2 ppm and hydrocarbons < 0.5 ppm). A pressure regulator (IR4000 series, Parker, USA) was used to keep the anode

pressure at a previously defined value. The pressure regulator was always open to keep the anode pressure constant and to allow “fresh” hydrogen to be fed from the bottle. A pressure transducer (PMP4000 series, GE, USA) monitored the pressure at the anode outlet.

Water was removed immediately after the anode exit to prevent condensation inside the instruments placed downstream. The anode exhaust gas was passed through a water trap consisting of a metal cylinder filled with a zeolite (Z10-02ND, Zeochem®, Switzerland) that was permanently immersed in a water-ice mixture; the zeolite was characterized by Ferreira *et al.* [22]. The ice was covered with raw salt, and the temperature was monitored using a portable digital thermometer equipped with a type K thermocouple; the temperature of the water-ice mixture was close to -1 °C. A solenoid valve (SV) (256 Series, ASCO®, USA) was used to purge the anode loop. A metering valve (M series, Swagelok, USA) was placed after the SV to keep constant the amount of gas purged [5].

To measure the hydrogen concentration inside the anode loop and to be able to perform nitrogen crossover studies, a hydrogen process sensor (HPM-100, Applied Sensor, Sweden) was placed downstream from the water trap. The flow rate of the recirculated gas was monitored continuously using a mass flow meter (EL-FLOW®, Bronkhorst, The Netherlands), which was placed after the hydrogen sensor. The dew point and temperature of the recirculated gas were measured downstream from the mass flow meter using a suitable probe (HMP110, Vaisala, Finland).

The anode gas was recirculated using a double diaphragm pump (Model N 86, KNF, Germany) and controlled by regulating its input voltage (0 V to 5 V). A gas filter (FW series, Swagelok, USA) was placed at the outlet of the diaphragm pump to minimize the flow rate oscillations.

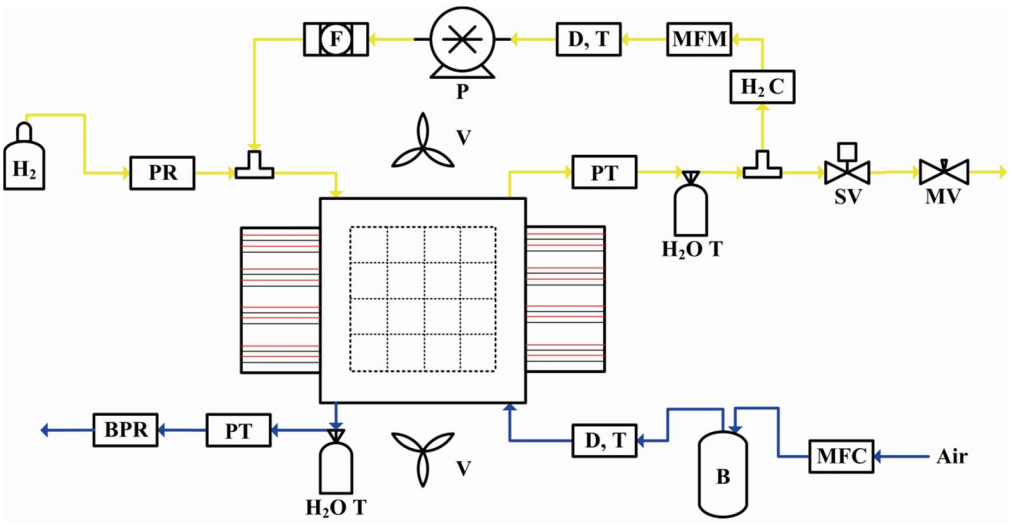


Figure 3.1. Scheme of the experimental test rig for water balance and nitrogen crossover studies. PR: pressure regulator; PT: pressure transducer; H2O T: water trap; SV: solenoid valve; MV: metering valve; H2 C: hydrogen concentration sensor; MFM: mass flow meter; D, T: dew point and temperature probe; P: recirculation pump; F: filter; MFC: mass flow controller; B: bubbler; BPR: Back pressure regulator; V: ventilator.

The cathode was fed with compressed air. The mass flow rate of air was controlled using a mass flow controller (EL-FLOW®, Bronkhorst, The Netherlands). A bubbling-type humidifier was used to regulate the dew point of air and set the desired relative humidity at the cathode. The dew point and temperature of the air at the cathode inlet were monitored with a suitable probe (HMP110, Vaisala, Finland). The cathode exhaust gas stream was also passed through a water trap consisting of a cylindrical vessel containing an inner serpentine which was connected in series with a cylinder filled with the same zeolite as the anode; the vessel was immersed in a water-ice mixture covered with raw salt. The cathode pressure was regulated using a pressure regulator (KLF series, Swagelok, USA) and monitored with a pressure transducer (PMP4000 series, GE, USA).

The mass flow controllers, pressure transducers and mass flow meters, were calibrated before the measurements. The hydrogen sensor was calibrated using dry hydrogen-nitrogen mixtures. Flexible heating cables were wrapped around the gas lines to prevent condensation.

An in-house written program implemented in Labview® was used to control the reactants' mass flow rates, the recirculation pump, the periodicity and duration of purges and the temperature of the gas lines. Moreover, the program was also used to monitor the anode and cathode pressures, the hydrogen concentration in the anode loop and the dew point and temperature of gases in the anode loop and cathode inlet.

### 3.3.2 Segmented PEMFC with partially segmented bipolar plates

The segmented cell (S++, Germany) had an active area of 25 $cm^2$ and was designed according to the Printed Circuit Board (PCB) concept introduced by Cleghorn *et al.* [23]. Nonetheless, the one reported here incorporates partially segmented anode and cathode BPs instead of a totally segmented anode bipolar plate with one PCB and a non-segmented cathode bipolar plate. The BPs (Graphite store, USA) were made from two isomolded and isotropic graphite blocks with 10.16 mm length x 10.16 mm width x 3.175 mm thickness and with a thermal conductivity of 83 $W \cdot m^{-1} \cdot K^{-1}$ (provided by manufacturer). Four-channel serpentine flow fields were machined on one side of each BP using computer numerical control (Tecnogial Lda, Portugal). The final dimensions of the BPs were 64 mm long x 64 mm wide x 2 mm thick while the channel dimensions were ca. 370 mm long x 1 mm wide x 1 mm thick. Partial segmentation of the BPs was achieved using computer numerical control (Tecnogial Lda, Portugal) to machine 16 square grooves on the flat surface of each BP. The grooves were not totally machined at the flow fields inlets and outlets to keep the cell gas tight. The grooves were 1 mm wide and 0.25 mm thick.

To assembly the SFC, two PCBs were used: one contacting the outer part of the anode and the other contacting the outer part of the cathode bipolar plate. Each printed circuit board was divided into 16 equal segments, which gave an approximate area of 1.56 $cm^2$ per segment. Figure 3.2.a shows the inlet and outlet of the cathode's bipolar plate as well as the area covered by each segment. Figure 3.2.b shows the back part of the anode's bipolar plate, the hydrogen inlet, hydrogen outlet and the partial segmentation. The air inlet is located at segment (4, 4) - (X, Y) and the outlet at segment (1, 1). In turn, the hydrogen inlet is located at segment (1, 4) and

the outlet at segment (4, 1). The electrochemical performance of the cell was assessed with an IM6/e electrochemical workstation connected to a PP 241 potentiostat and a RMUX multiplexer (Zahner®, Germany). Figure 3.3. shows the front and back of one PCB and a schematic of the electrical connection.

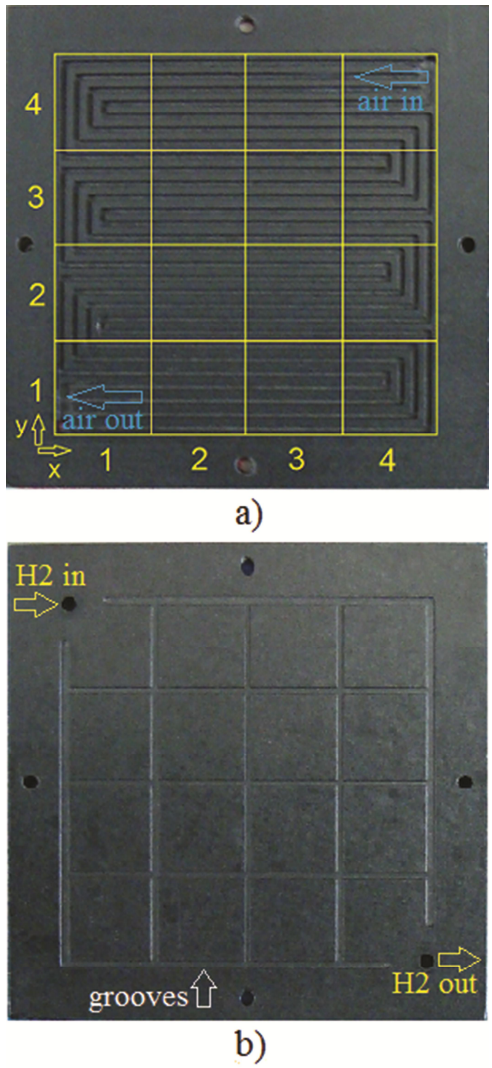


Figure 3.2. a) Cathode bipolar plate with the four-channel serpentine flow field and detailed location of the inlet, outlet and segments. b) Back part of the anode bipolar plate and detailed location of the hydrogen inlet, outlet and grooves.

The temperature of the cell was controlled using a temperature controller (3200 Series, Eurotherm, USA) with heating and cooling capabilities. For heating, four power film resistors model MP-930 (Caddock Electronics, Inc., USA), were evenly distributed and attached to each end-plate. The end-plates were made from a stainless steel block with 80 mm length x 80 mm width x 20 mm thickness. For cooling, two ventilators located ca. 3 cm away from each end-plate were used. The temperature of the cell was measured with a type K thermocouple carefully inserted in the geometric center of the cathode end-plate and as close as possible to the outer surface of the BP.

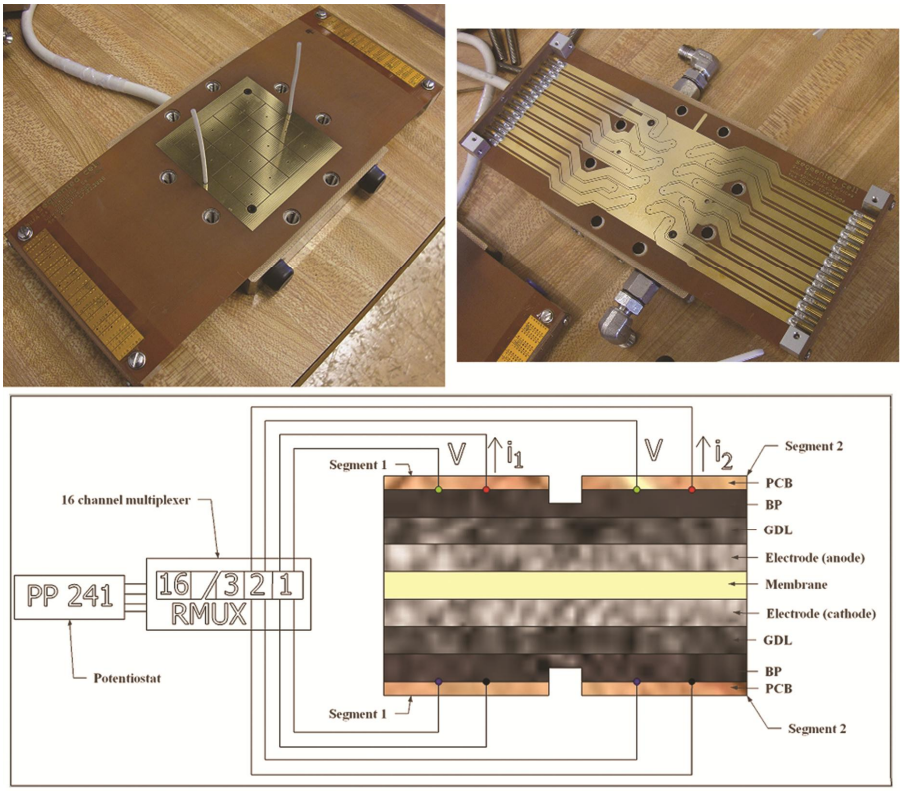


Figure 3.3. Front and back of one printed circuit board (PCB) and electrical connection schematic of the segmented cell incorporating partially segmented bipolar plates.

The SFC was equipped with a commercial catalyst-coated membrane based on an 18 µm thick membrane containing 0.4 mg Pt·cm$^{-2}$ on both the anode and cathode. The GDLs were Sigracet® SGL 35 BC (SGL technologies GmbH, Germany) with 325 µm

thickness. Teflon® gaskets with 225 µm thickness were used. A torque of 2.5 N·m was applied to the bolts to finalize the assembly. The pressure distribution between surfaces was checked using LLLW pressure sensitive film (Fujifilm, Japan).

### 3.3.3. Test protocol

Table 4 summarizes the experimental conditions used. The voltage supplied to the pump relative to maximum possible ($V_{rel}$), the anode pressure ($P_{ano}$) and the time between purges, here defined as a "purge cycle", were varied while the cathode conditions were held constant. The $V_{rel}$ was set to 5.0% and 17.5% and the $P_{ano}$ was set to 0.110 MPa and 0.130 MPa. The purge cycles were 60/1 s and 240/1 s, that is, during the measurements the SV was closed for 60 s or 240 s followed by 1 s open. Experiments #9 and #10 were performed to evaluate the stability of the cell at higher $V_{rel}$. The air volumetric flow rate ($Q_{air}$) was 1132 $cm^3 \cdot min^{-1}$, the cathode pressure ($P_{cat}$) was 0.110 MPa and the cathode dew point ($T_{dew,cat}$) was 57 °C. The cell temperature ($T_{cell}$) was set to 60 °C. The polarization curves were performed in potentiostatic mode starting at open circuit voltage conditions and finishing at 350 mV.

Table 4 - Summary of experimental conditions. The corresponding flow rates are STP (273.15 K and 0.100 MPa).

| Exp. # | Cell | Anode | | | Cathode | | |
|---|---|---|---|---|---|---|---|
| | $T_{cell}$ (°C) | $V_{rel}$ (%) | $P_{ano}$ (MPa) | purge cycle | $Q_{air}$ ($cm^3 \cdot min^{-1}$) | $P_{cat}$ (MPa) | $T_{dew,cat}$ (°C) |
| 1 | 60 | 5.0 | 0.110 | 60/1 | 1132 | 0.110 | 57 |
| 2 | | 17.5 | | 60/1 | | | |
| 3 | | 5.0 | | 240/1 | | | |
| 4 | | 17.5 | | 240/1 | | | |
| 5 | | 5.0 | 0.130 | 60/1 | | | |
| 6 | | 17.5 | | 60/1 | | | |
| 7 | | 5.0 | | 240/1 | | | |
| 8 | | 17.5 | | 240/1 | | | |
| 9 | | 23.5 | 0.110 | 60/1 | | | |
| 10 | | 23.5 | 0.130 | 60/1 | | | |

Regarding the CDD experiments, the fuel cell was operated in potentiostatic mode at 600 mV with the experimental conditions of interest until the hydrogen concentration in the anode loop and the anode dew point stabilized. Then the cell was operated for 30 minutes with the experimental conditions of interest to guarantee steady state conditions for the CDD measurements. After this, the current of each segment was measured sequentially three times, with each sequential set of measurements taking approximately 2 minutes. The current of each segment was averaged and used to create the CDD diagrams.

## 3.4. Results and discussion

### 3.4.1. Increase of in-plane resistance using partially segmented bipolar plates

In SFC research, it may be necessary to physically modify (to segment) components of the assembly such as the GDLs or BPs when using any of the three main invasive approaches proposed so far [15], namely, Printed Circuit Board, Resistors Network or Hall Effect Sensors. The objective of the segmentation is to create the necessary through-plane paths (perpendicular to the MEA) to collect the current from each segment of the cell. However, the anisotropic properties of materials and contact resistance differences at the components interfaces may originate in-plane paths (parallel to the MEA), by which the current would flow and "spread" from one segment to the next. The efforts to estimate the uncertainties associated with in-plane or lateral current spreading in SFC have been summarized by Eckl. *et al.* [19], who estimated a maximum lateral current spreading between 5% to 11.5% for a cell with non-segmented GDLs or BPs but incorporating one PCB at the anode and 2% to 8% for a cell with non-segmented GDLs but segmented anode BP and current collector respectively.

As seen, in order to increase the accuracy and reliability of local electrochemical measurements, it is important to minimize the lateral current spreading at the components level. This can be done by electrically isolating the segments starting at the CLs and finishing at the BPs level. Nonetheless, this complicates the design,

construction and assembly of SFC. For example, one way to achieve total segmentation (i.e., full electrical isolation) of the CL is to incorporate the catalyst in a membrane area corresponding to one segment, then repeating this process for all the segments leaving a constant space between them. If the catalyst is incorporated in the GDL, it is necessary to cut the segments and use a gasket as frame to hot-press them simultaneously on the membrane [24].

Regarding total segmentation of the BPs, two techniques are commonly used. The first is used with graphite bipolar plates and involves five steps [25]: i) partial milling of the segments, ii) filling the gaps with an epoxy resin, iii) once the resin is cured, the opposite face of the plate is milled so the segments are electrically isolated, iv) polishing and v) machining of the flow field. The second technique is based on attaching conductive prism-shaped blocks to a non-conductive rigid frame [26]; after this, the flow field is machined. The main disadvantages of total segmentation of the GDLs and BPs are: i) changed electrochemical, fluid dynamics and thermal properties of the components, meaning less compatibility with actual components used in PEMFC stacks, ii) the possibility of membrane failure due to misalignment of corresponding anode and cathode GDL segments [27] or due to inhomogeneous mechanical support of the GDL to the MEA [28] and iii) gas leaks at the BPs if the resin or other materials are not correctly selected.

Due to the stated disadvantages, it is important to explore alternative techniques to decrease the lateral current spreading at the components level while at the same time avoiding their total segmentation. One technique was developed by Hakenjos *et al.* [29] who introduced the use of partially segmented GDL as alternative to total segmentation of the GDL. As a result, the ohmic resistance increased 0.5 Ω between adjacent segments. In the same way, it would be interesting to analyze the effect of incorporating partially segmented BPs in an SFC; however, this has not been proposed, to the authors' knowledge. Thus, the technique for partial segmentation of the BPs is introduced here as an alternative to total segmentation of these components.

For the partially segmented BPs used here, the increase on the lateral resistance between adjacent segments, $\Delta R_{latn}$ (%), was calculated according to Eq. (1):

$$\Delta R_{latn} = \left( \frac{\gamma \frac{w}{A_n} \cdot 100}{\frac{w}{A_{On}}} \right) - 100 \quad (1)$$

where $\gamma$ is the resistivity of the graphite, $1.39 \cdot 10^{-5}$ Ω·m (provided by the manufacturer), $w$ is the width of the groove (m), $A_n$ is the cross-sectioned area of the BP under the groove after segmentation ($m^2$) and $A_{On}$ is the cross-sectioned area of the BP under the groove before segmentation ($m^2$). It should be highlighted that $w$ is constant, which is not the case for $A_n$, once this area is affected by the relative position of the groove in the flow field, as seen on Figure 3.2. After analyzing the flow field geometry under the grooves for all the segments, four different values for $A_n$, namely, $A_1$, $A_2$, $A_3$ and $A_4$, were identified. With the partial segmentation, $\Delta R_{lat1}$ (corresponding to $A_1$), increased ≈ 14%, $\Delta R_{lat2}$ increased ≈15%, $\Delta R_{lat3}$ increased ≈ 16 % and $\Delta R_{lat4}$ increased ≈ 21%. As seen, the increase in $\Delta R_{latn}$ was modest, implying that the partial segmentation of the BPs may not be really effective for the groove depth of 0.25 mm selected here. Further, the number of ribs and channels under the grooves affect the relative cross sectioned area of the current path to different extents, leading to a non-homogeneous increase in $\Delta R_{latn}$ between horizontally and vertically adjacent segments.

To make the partial segmentation of the BPs more effective, $\Delta R_{latn}$ should be increased. Using Eq. 1 and a groove depth of 0.60 mm, it was estimated that $\Delta R_{latn}$ may increase between 44% and 70%, providing a representative increase in the lateral resistance and not significantly compromising the mechanical strength of the plate. Ultimately, the partial segmentation's effectiveness depends on the gas flow channel geometry, groove geometry, bipolar plate thickness and mechanical strength.

To further analyze the effect of incorporating the partially segmented BPs, the ratio of the through-plane to the in-plane resistance, $R_{tp}/R_{ip}$, was estimated for each segment using different groove depths according to Eq. (2):

$$R_{tp} / R_{ip} = \frac{\gamma \frac{w_{tp}}{A_{tp}}}{\gamma \frac{w}{A_{ip,m}}} \quad (2)$$

where $R_{tp}$ is the through-plane resistance (Ω), $R_{ip}$ is the in-plane resistance (Ω), $w_{tp}$ is the thickness of the bipolar plate (m), $A_{tp}$ is the area of each segment ($m^2$) and $A_{ip,m}$ is the cross sectioned area of the bipolar plate under the groove area ($m^2$) for each groove depth analyzed ($m$ = 0.25 mm, 0.40 mm, 0.50 mm, 0.60 mm and 0.75 mm). For these calculations, $w_{tp}$ was set to 1.5 mm once the thickness of the BPs is not even due to the gas flow channels. The results of the calculations are shown on Figure 3.4. It is observed that when the bipolar plate is not partially segmented (i.e. groove depth zero) the value of $R_{tp}/R_{ip}$ is already low, 0.18. The last is attributed to the larger trough-plane area (segment area) when compared to the in-plane cross sectioned area of the bipolar plate. When the groove depth is 0.25 mm, as in our partially segmented bipolar plates, $R_{tp}/R_{ip}$ = 0.15. This means that the partial segmentation led to a 17% decrease on $R_{tp}/R_{ip}$, which is also quite low, but can be further decreased using deeper grooves as observed on Figure 3.4.

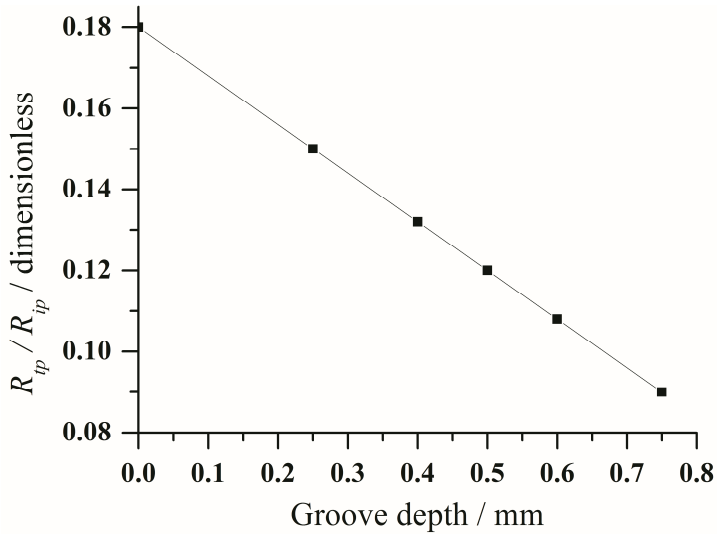


Figure 3.4. Through-plane to in-plane resistance ratio as a function of the groove depth of the partially segmented bipolar plates.

### 3.4.2. Characterization and performance of the cell

#### *3.4.2.1. Anode recirculation loop parameters*

Three important parameters were obtained for the gas stream on the anode recirculation loop: i) flow rate, ii) hydrogen concentration and iii) anode dew point.

First, the gas flow rate was measured using dry hydrogen for the two operating pressures at $T_{cell}$ = 60 °C, without drawing any current from the cell. The results were then plotted as a function $V_{rel}$ and are shown in Figure 3.5. For $V_{rel}$ = 5%, $Q_{H2} \approx 81$ cm$^3$·min$^{-1}$ for $P_{ano}$ = 0.110 MPa and $Q_{H2} \approx 90$ cm$^3$·min$^{-1}$ for $P_{ano}$ = 0.130 MPa. For $V_{rel}$ = 17.5%, $Q_{H2} \approx 230$ cm$^3$·min$^{-1}$ and 244 cm$^3$·min$^{-1}$ at $P_{ano}$ = 0.110 MPa and 0.130 MPa, respectively. Slightly higher recirculation rates were achieved at higher operating pressures; similar behavior was observed with the same type of pumps at stack level [21]. Hydrogen flow rate oscillations were mitigated by inserting a filter at the pump outlet, as recommended elsewhere [30].

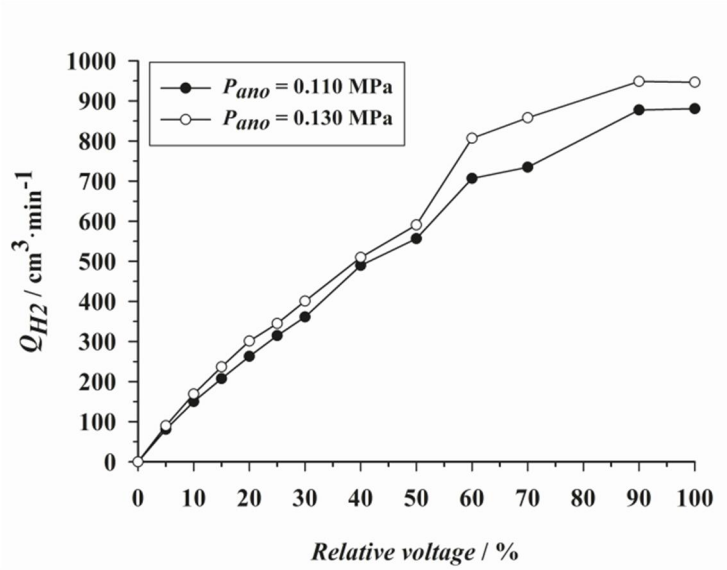


Figure 3.5. Hydrogen flow rate as a function of the voltage supplied to the pump relative to maximum possible. The corresponding flow rates are STP (273.15 K and 0.100 MPa).

The hydrogen concentration, $C_{H2}$ (v/v%), of the recirculated stream was measured to prevent fuel starvation. During operation, nitrogen permeates from the cathode to the anode due to a concentration gradient, decreasing the hydrogen partial pressure along the flow field path [31]. For Experiments #1 to #8, the $C_{H2}$ in the recirculated gas varied between 97.9% and 99.0%. The average hydrogen concentration was 98.0% for experiments at $P_{ano}$ = 0.100 Mpa and 98.9% for experiments at $P_{ano}$ = 0.130 Mpa. This difference may be explained by the higher hydrogen partial pressure when the cell was operated at $P_{ano}$ = 0.130 MPa, assuming that the nitrogen permeation rate was approximately the same. In turn, the average hydrogen concentration was approximately 98.4% for the experiments at 60/1 s and 240/1 s purge cycle. A lower hydrogen concentration would be expected for the 240/1 s purge cycle due to more nitrogen build-up at the anode; however, the difference would be so low for the time scale [32] that it could not be measured accurately with the hydrogen sensor. From the average values obtained for the hydrogen concentration of all experiments and Ref. [21], it was concluded that nitrogen crossover effects were negligible for the experiments performed here.

Also, the dew point of the recirculated gas was constantly measured to evaluate the effectiveness of the anode water trap. During start-up of Experiments #1 to #8, $T_{dew,ano}$ varied between 10 °C and 0 °C; however, for the polarization curves and CDD experiments, $T_{dew,ano}$ stabilized around -10 °C at the anode inlet, corresponding to a water vapor pressure of approximately 300 Pa. The higher relative humidity during start-up should be related to the water that condensed at the anode flow field after shutdown.

### *3.4.2.2. Polarization curves*

Figure 3.6 shows the polarization curves for Experiments #1 to #10. In general, the performance of the cell was low due to the use of dry hydrogen and a non-optimized anode humidification approach. The equipment available for anode humidification was a bubbling-type humidifier. This device would not provide constant humidification to the anode gas stream because the hydrogen flow rate peaks during the 1 s purge step. The anode humidification problem could be overpassed using a membrane-type humidifier [33].

The polarization curves concerning Experiments #1 to #8 show almost the same shape between the open circuit voltage and 600 mV. This may indicate that the activation losses and ohmic losses are similar. Interestingly, between 600 mV and 550 mV a slightly steeper decrease in performance is observed for the experiments with $V_{rel}$ = 5%, indicating that this parameter may affect the transition between the ohmic and mass transport regime of the cell. Below 550 mV, the polarization curves show the non-linear decrease in performance associated with the mass transport regime, where performance losses are dominated by the increased mass transfer resistance to the electrodes.

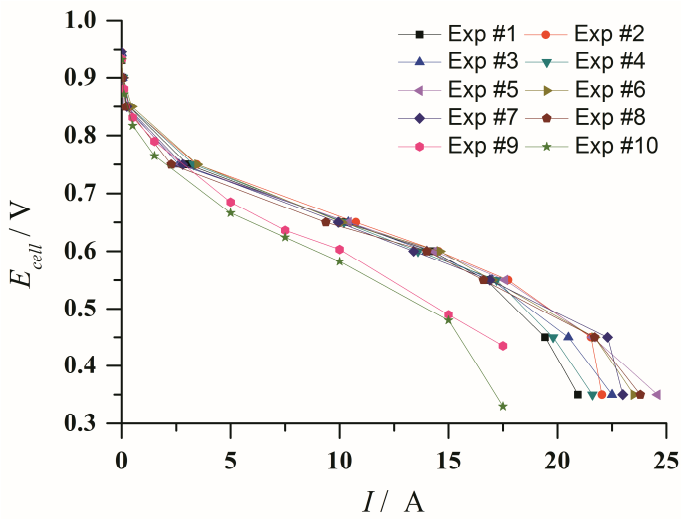


Figure 3.6. Polarization curves for Experiments #1 to #10. Experimental conditions in Table 4.

Figure 3.6 also shows how the results for Experiments #9 and #10, conducted at $V_{rel}$ = 23.5%, clearly show poorer performance when compared to Experiments #1 to #8, conducted at $V_{rel}$ = 5% and $V_{rel}$ = 17.5%. At $V_{rel}$ = 23.5%, the inlet of the cell suffered excessive drying, leading to a divergence in cell performance. The excessive drying was reflected close to the gas inlets on the CDD diagrams of Exps. #9 and #10 and on the fuel cell high frequency resistance obtained by electrochemical impedance spectroscopy (EIS) [34] (not shown here).

### *3.4.2.3. Reactants utilization*

The fuel utilization, $\mu_f$ (%), for Experiments #1 to #8 at 600 mV can be estimated by applying a simple mass balance to the anode:

$$\mu_f = \frac{\dot{n}_{H2,cons}}{\dot{n}_{H2,feed}} \cdot 100 \qquad (3)$$

where $\dot{n}_{H2,cons}$, is the hydrogen consumed (mol·s$^{-1}$) and $\dot{n}_{H2,feed}$ is the total amount of hydrogen introduced to the cell (mol·s$^{-1}$). The hydrogen consumed is calculated from the total current values, $I$ (A), in Figure 3.6 using Faraday's law and assuming 100% coulombic efficiency:

$$\dot{n}_{H2,cons} = \frac{I}{2F} \tag{4}$$

where $F$ is the Faraday constant, 96485.34 C·mol$^{-1}$. In turn, the total amount of hydrogen introduced to the cell is determined by:

$$\dot{n}_{H2,feed} = \dot{n}_{H2,bot} + \dot{n}_{H2,rec} \tag{5}$$

Where $\dot{n}_{H2,bot}$, is the "fresh" hydrogen coming from the bottle (mol·s$^{-1}$), which is equal to the hydrogen consumed, and $\dot{n}_{H2,rec}$ is the recirculated hydrogen molar rate which is obtained from Figure 3.5.

In the same way, the oxidant utilization, $\mu_{ox}$ (%), for experiments #1 to #8 at 600 mV can be estimated from:

$$\mu_{ox} = \frac{\dot{n}_{O2,cons}}{\dot{n}_{O2,feed}} \cdot 100 \tag{6}$$

where $\dot{n}_{O2,cons}$ is the oxygen consumed (mol·s$^{-1}$) and $\dot{n}_{O2,feed}$ is the total amount of oxygen introduced to cell (mol·s$^{-1}$), obtained from Table 4. The oxygen consumed is calculated from the total current values in Figure 3.6 using Faraday's law, assuming a molar fraction ($X_{O2}$) of 0.21 for the oxygen in air and 100% coulombic efficiency:

$$\dot{n}_{O2,cons} = \frac{I}{4X_{O2}F} \tag{7}$$

Table 5 summarizes the results of section 3.4.2 with the corresponding hydrogen and oxygen stoichiometric ratios which were calculated from the reciprocal of the fuel and oxidant utilizations respectively.

Table 5 - Parameters obtained from the characterization of the anode loop and evaluation of the SFC performance for Experiments #1 to #8. The corresponding flow rates are STP (273.15 K and 0.100 MPa). Note: n.a. stands for no applicable since the stoichiometry is dimensionless.

| Exp. # | $Q_{H2,rec}$ ($cm^3 \cdot min^{-1}$) | $C_{H2}$ (%) | $T_{dew,ano}$ (K) | $I$ (A) | $Q_{H2,bot}$ ($cm^3 \cdot min^{-1}$) | $\mu_f$ ( %) | $\lambda_{H2}$ (n.a.) | $\mu_{ox}$ ( %) | $\lambda_{O2}$ (n.a.) |
|---|---|---|---|---|---|---|---|---|---|
| 1 | 81 | 98.0 | 263 | 14.2 | 108 | 57.1 | 1.7 | 22.7 | 4.4 |
| 2 | 230 | 98.1 | | 14.5 | 110 | 32.4 | 3.1 | 23.2 | 4.3 |
| 3 | 81 | 98.0 | | 14 | 106 | 56.8 | 1.8 | 22.4 | 4.5 |
| 4 | 230 | 97.9 | | 13.6 | 103 | 31.0 | 3.2 | 21.7 | 4.6 |
| 5 | 90 | 98.9 | | 14.3 | 108 | 54.7 | 1.8 | 22.9 | 4.4 |
| 6 | 244 | 98.9 | | 14.6 | 111 | 31.3 | 3.2 | 23.4 | 4.3 |
| 7 | 90 | 98.8 | | 13.4 | 103 | 53.1 | 1.9 | 21.4 | 4.7 |
| 8 | 244 | 99.0 | | 14 | 106 | 30.4 | 3.3 | 22.4 | 4.5 |

### 3.4.3. Current density distribution diagrams

#### *3.4.3.1. Effect of recirculation rate - anode flooding detection*

Figures 3.7 and 3.8 depict the effect of increasing $V_{rel}$ at a cell voltage of 600 mV when $P_{ano}$ = 0.110 MPa (Figure 3.7) and $P_{ano}$ = 0.130 MPa (Figure 3.8). Experiments with $V_{rel}$ = 5% (Figures 3.7 and 3.8, Exps. #1 and #5) show a maximum in current density in row 3, decreasing slightly towards the anode outlet. Experiments with $V_{rel}$ = 17.5% (Figures 3.7 and 3.8, Exps. #2 and #6) show a lower performance at the inlets but quite homogeneous CDD after row 4. This means that lower recirculation flow rates led to a decrease in the current density towards the flow field outlets, while higher recirculation flow rates led to a decrease in the current density close to the flow field inlets. The corresponding numerical values for the current density of each segment are presented in Table 6.

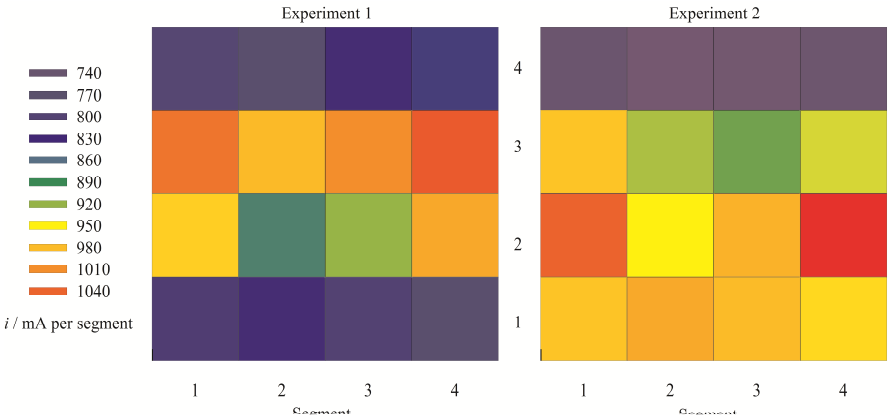


Figure 3.7. Current density distribution diagrams for Experiments #1 ($V_{rel}$ = 5%, $I$ = 14.2 A) and #2 ($V_{rel}$ = 17.5%, $I$ = 14.5 A) and for 600 mV cell voltage. Other experimental conditions are as in Table 4.

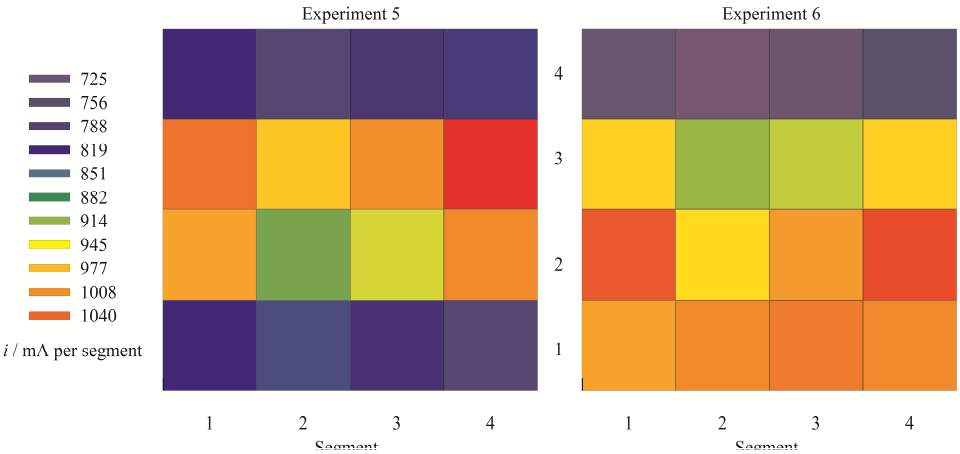


Figure 3.8. Current density distribution diagrams for Experiments #5 ($V_{rel}$ = 5%, $I$ = 14.3 A) and #6 ($V_{rel}$ = 17.5%, $I$ = 14.6 A) and for 600 mV cell voltage. Other experimental conditions are as in Table 4.

To prevent a misleading interpretation of the CDD diagrams, it is important to understand the anode water accumulation mechanisms and find suitable approaches to confirm whether flooding may actually occur during the low recirculation experiments. To do this, two approaches can be taken: the first based on the water balance of the cell [20] and the second based on estimating the type of flow pattern from and empiric flow map suggested by Hussaini and Wang [35]. It is noteworthy the coupling effect of local current density and local temperature, which may affect the local water transport if the temperature gradient along the MEA active area is high.

In the present work, the effect of local temperature on water transport was considered to be negligible for many reasons. First, proper distribution of the heating elements and proper placement of the thermocouple. Even though the sensitivity of the temperature controller was set to one decimal place, no noticeable variation in the temperature was observed during the CDD experiments. Moreover, the thermocouple was inserted in the cathode, which has been reported to be the electrode with higher temperature and uneven temperature distribution gradient [36]. Second, thin (2 mm) BPs and thick (20 mm) end-plates with larger heated area (64 $cm^2$) than the cell active area (25 $cm^2$) were used. Third, during the CDD experiments the average difference between the segments with the highest current density and the lowest current density was $I$ = 290 mA. This low average difference means low influence of the current produced at each segment in the local heat generation and consequent temperature gradient [37]. Fourth, the high cathode flow rate used ($Q_{air}$ = 1132 $cm^3 \cdot min^{-1}$) improved the heat removed by convection, contributing to a more uniform temperature distribution along the MEA active area, as observed elsewhere [29] [38].

Table 6 - Numerical values for the current density of each segment in the current density distribution diagrams of Figures 3.7-3.10. The coordinates correspond to those of the flow fields.

| | | Experiment #1 | | | | Experiment #2 | | | | Experiment #4 | | | |
|---|---|---|---|---|---|---|---|---|---|---|---|---|---|
| Y | 4 | 810 | 795 | 835 | 845 | 760 | 740 | 740 | 755 | 660 | 640 | 630 | 640 |
| | 3 | 1005 | 965 | 990 | 1020 | 960 | 920 | 905 | 930 | 845 | 820 | 800 | 820 |
| | 2 | 955 | 880 | 915 | 975 | 1015 | 940 | 970 | 1040 | 980 | 900 | 930 | 985 |
| | 1 | 820 | 835 | 815 | 795 | 960 | 975 | 965 | 950 | 975 | 1000 | 1020 | 995 |
| | | 1 | 2 | 3 | 4 | 1 | 2 | 3 | 4 | 1 | 2 | 3 | 4 |
| | | X | | | | | | | | | | | |

| | | Experiment #5 | | | | Experiment #6 | | | |
|---|---|---|---|---|---|---|---|---|---|
| Y | 4 | 830 | 800 | 815 | 835 | 750 | 725 | 745 | 775 |
| | 3 | 1005 | 955 | 985 | 1040 | 950 | 910 | 920 | 950 |
| | 2 | 975 | 900 | 925 | 990 | 1020 | 945 | 980 | 1025 |
| | 1 | 830 | 840 | 820 | 800 | 975 | 990 | 1000 | 990 |
| | | 1 | 2 | 3 | 4 | 1 | 2 | 3 | 4 |
| | | X | | | | | | | |

The mechanisms for anode water accumulation have been described by Owejan *et al*. [39] and Lee and Bae [40]. In our case, because dry hydrogen is being fed to the cell, the amount of water collected at the anode water trap (not shown here) clearly indicates that water diffusing from the cathode to the anode is enough to saturate the anode exhaust for the low recirculation experiments. Thus, in order to have water condensation at the anode, first the cathode condition must enable the cathode water vapor pressure to exceed the saturation vapor pressure, reaching the saturation state at the cathode. Then, the amount of water diffusing from cathode to anode must be high enough to saturate the anode exhaust.

The water balance approach can be achieved by analyzing the water mass flow rates inside the cell. Due to the water concentration gradient arising from the use of dry hydrogen, the water fed to the cathode and the water produced at the cathode, it is expected that the dominant water transport mechanism across the membrane is diffusion from the cathode to the anode [3]. To assess the net water mass flow rate between the electrodes it is necessary to know the net water drag coefficient [41], $\alpha$, which is related to the net transport of water from the anode to the cathode and accounts for the electro osmotic drag and diffusion of water from the cathode to the anode. The value of $\alpha$ depends on many factors. In our case, experimental values for $\alpha$ have been reported between -0.21 [42], -0.18 [43] and -0.15 [44] for cells operating in similar conditions, i.e. dry hydrogen and humidified air, and assembled with similar components. It is well known that the net water drag coefficient may be uneven along the MEA active area [45] and may be influenced by the local temperature. Nevertheless, a value of $\alpha$ = -0.18 (this is, the average value of Refs. [42] [43] [44]) was used here to facilitate the water balance analysis. The negative sign of $\alpha$ indicates a net transport of water from the cathode to the anode. It is important to highlight that the water vapor pressure at the anode inlet is negligible, as stated in section 3.4.2.

The water mass flow rate fed by humidification of air at the cathode inlet, $\dot{m}_{H2Oin,cat}$ (kg·s$^{-1}$), the maximum water mass flow rate removed by air in the form of saturated vapor at the cathode outlet, $\dot{m}_{H2Oout,cat}$ (kg·s$^{-1}$), the water mass flow rate produced by

the electrochemical reaction assuming 100% coulombic efficiency, $\dot{m}_{H2O,ele}$ (kg·s$^{-1}$), the net water mass flow rate between the anode and cathode, $\dot{m}_{H2O,ano-cat}$ (kg·s$^{-1}$), and the maximum water mass flow rate that can be removed by the hydrogen in the form of saturated vapor at the anode outlet, $\dot{m}_{H2Oout,ano}$ (kg·s$^{-1}$), were calculated through Eqs. (7) - (11), adapted from [42]:

$$\dot{m}_{H2Oin,cat} = \frac{P_{sat(Tcell)} RH_{cat}}{P_{cat} - P_{sat(Tcell)} RH_{cat}} \left( \frac{1}{\mu_{ox} X_{O2}} \right) \frac{I}{4F} M_{H2O} \tag{8}$$

$$\dot{m}_{H2Oout,cat} = \frac{P_{sat(Tcell)} RH_{cat}}{P_{cat} - P_{sat(Tcell)} RH_{cat}} \left( \frac{1}{\mu_{ox} X_{O2}} - 1 \right) \frac{I}{4F} M_{H2O} \tag{9}$$

$$\dot{m}_{H2O,ele} = \frac{I}{2F} M_{H2O} \tag{10}$$

$$\dot{m}_{H2O,ano-cat} = -\alpha \frac{I}{F} M_{H2O} \tag{11}$$

$$\dot{m}_{H2Oout,ano} = \frac{P_{sat(Tcell)}}{P_{ano} - P_{sat(Tcell)}} \left( \frac{1}{\mu_f} - 1 \right) \frac{I}{2F} M_{H2O} \tag{12}$$

where $P_{sat,(Tcell)}$ (Pa) is the saturation pressure of water vapor at the cell´s operating temperature and pressure, $RH_{cat}$ (%) is the relative humidity of the cathode feed at the inlet (%), $P_{cat}$ (Pa) is the cathode pressure and $M$ is the molecular weight of water, 0.018 kg·mol$^{-1}$. The saturation pressure of water for the air-water vapor and hydrogen-water vapor mixtures was calculated using the formula proposed by Wagner and Pruss [49].

Table 7 summarizes the results of the water balance calculations. It can be seen that $\dot{m}_{H2O,ano-cat}$ is smaller than $\dot{m}_{H2Oout,ano}$ in all low recirculation experiments ($V_{rel}$ = 5%: Exps. #1, #3, #5 and #7). In these cases, the negative values for $\dot{m}_{H2O,ano-cat} - \dot{m}_{H2Oout,ano}$ imply that water diffusing from the cathode tends to

accumulate in the cell. The CDD diagrams indicate that close to the inlets there is a net water transport from the cathode to the anode as long as the anode has a lower relative humidity. Going down in the flow field channels, the water concentration gradient between the electrodes decreases and water starts condensing on both electrodes as the saturation pressure of water vapor is reached. The latter happens at the cathode, where water is continuously produced and the relative humidity is high and at the anode, where hydrogen is continuously consumed and no more water can be removed in vapor form.

Interestingly, Table 7 also shows that $\dot{m}_{H2Oout,ano}$ surpasses $\dot{m}_{H2O,ano-cat}$ in all high recirculation experiments ($V_{rel}$ = 17.5%: Exps. #2, #4, #6 and #8). In these cases, the positive values for $\dot{m}_{H2O,ano-cat} - \dot{m}_{H2Oout,ano}$ imply that water does not tend to accumulate in the cell. The CDD diagrams also indicate that close to the inlets there is a net water transport of water from cathode to the anode; however, the electrochemical activity of row 4 is lower than experiments with $V_{rel}$ = 5%, which may be attributed to drying of the membrane for the experiments with high recirculation. Finally, when going down in the flow field channels for $V_{rel}$ = 17.5%, the water diffusing from the cathode is not enough to saturate the anode and no water condenses.

As stated above, the second approach to gain insight into whether flooding occurs is based on estimating the type of flow pattern from an empiric flow map. Recently, empirical maps have been used to characterize the type of flow patterns in the PEMFC flow fields [46]. The idea is to plot the liquid gas velocity at the outlet as a function of the gas velocity at the inlet of the anode or cathode flow fields, creating a flow map on which different regions correspond to different flow patterns. In order to know the liquid gas velocity at the outlet of the anode or the cathode flow fields, it is important to determine the net water transport in the cell first. The flow patterns for the cathode of an operating PEMFC have been categorized in one single-phase flow and three two-phase flows: droplet flow, film flow and slug flow [35].

Table 7 - Results of the water balance calculations.

| Exp. # | Cathode | | | |
|---|---|---|---|---|
| | $\dot{m}_{H2Oin,cat}$ | $\dot{m}_{H2Oin,ele}$ | $\dot{m}_{H2Oout,cat}$ | $\left(\dot{m}_{H2Oin,cat} + \dot{m}_{H2O,ele}\right) - \dot{m}_{H2Oout,cat}$ |
| | ($kg \cdot 10^{-6} \cdot s$) | | | |
| 1 | 2.71 | 1.33 | 2.94 | 1.10 |
| 2 | 2.71 | 1.35 | 2.93 | 1.13 |
| 3 | 2.74 | 1.31 | 2.96 | 1.09 |
| 4 | 2.72 | 1.27 | 2.95 | 1.04 |
| 5 | 2.73 | 1.34 | 2.96 | 1.11 |
| 6 | 2.73 | 1.36 | 2.95 | 1.14 |
| 7 | 2.74 | 1.25 | 2.97 | 1.02 |
| 8 | 2.74 | 1.31 | 2.96 | 1.09 |
| Exp. # | Anode | | | |
| | $\dot{m}_{H2Oano-cat}$ | $\dot{m}_{H2Oout,ano}$ | $\dot{m}_{H2Oano-cat} - \dot{m}_{H2Oout,ano}$ | Note |
| | ($kg \cdot 10^{-6} \cdot s^{-1}$) | | | |
| 1 | -0.47 | 0.22 | -0.25 | Flooding |
| 2 | -0.48 | 0.63 | 0.15 | No flooding |
| 3 | -0.47 | 0.22 | -0.25 | Flooding |
| 4 | -0.45 | 0.63 | 0.18 | No flooding |
| 5 | -0.48 | 0.20 | -0.28 | Flooding |
| 6 | -0.49 | 0.54 | 0.05 | No flooding |
| 7 | -0.45 | 0.20 | -0.25 | Flooding |
| 8 | -0.47 | 0.54 | 0.07 | No flooding |

From the water balance calculations, flooding can be expected in Experiments #1, #3, #5 and #7, indicating the possibility of a two-phase flow pattern. In contrast, no flooding is expected for Experiments #2, #4, #6 and #8, indicating the possibility of a single-phase flow. To estimate the type of flow pattern, it is necessary to calculate the anode gas velocity, $u_{in,g,ano}$ ($m \cdot s^{-1}$), and the cathode gas velocity, $u_{in,g,cat}$ ($m \cdot s^{-1}$), at the inlet of the respective flow fields and the liquid velocity at the outlet of the anode flow field, $u_{out,l,ano}$ ($m \cdot s^{-1}$), from Eqs. (12) - (14) [47] respectively. These equations assume ideal gas behavior for the inlets, exhaust saturation at the anode

outlet (when applicable) and equal distribution of the fluids on the flow field channels:

$$u_{in,g,ano} = \frac{\dot{m}_{H2,feed}}{\rho_{H2} NA} \tag{13}$$

$$u_{in,g,cat} = \frac{\dot{m}_{air,feed}}{\rho_{air} NA} \tag{14}$$

$$u_{out,l,ano} = \frac{\dot{m}_{H2O,ano-cat} - \dot{m}_{H2Oout,ano}}{\rho_{H2O} NA} \tag{15}$$

where $\dot{m}_{H2,feed}$ (kg·s$^{-1}$) is the mass flow rate of hydrogen at the inlet and is obtained from the volumetric flow rates on Table 5, $\rho_{H2}$ (kg·m$^{-3}$) is the density of hydrogen, $N$ is the number of channels, $A$ (m$^2$) is the cross sectioned area of each channel, $\dot{m}_{air,feed}$ (kg·s$^{-1}$) is the mass flow rate of air at the inlet and is obtained from the volumetric flow rate on Table 4, $\rho_{air}$ (kg·m$^{-3}$) is the density of air and $\rho_{H2O}$ (kg·m$^{-3}$) is the density of water. The liquid velocity at the anode inlet is zero for all cases, as implied from Eq. (14).

Table 8 summarizes the results for the velocity calculations. In all cases, the corresponding gas velocity at the inlet of the cathode flow field is located on the single-phase region of the flow map proposed by Hussaini and Wang [35]. When $V_{rel}$ = 5%, the corresponding gas velocity at the anode inlet and the liquid velocity at the anode outlet is located on the slug flow region of the same flow map. Lastly, when $V_{rel}$ = 17.5%, the corresponding gas velocity at the anode inlet is located on the single-phase region of the same flow map. It is important to highlight that the flow map proposed by Hussaini and Wang [35] is only valid for that specific experimental set-up [46] so actual confirmation of the flow patterns may need implementation of a transparent cell [40] in our set-up. Nevertheless, after performing the water balance analysis, the gas velocity calculations and their interpretation from that flow map helped to further gain insight on the type of flow patterns expected in this study.

Table 8 - Gas and liquid velocities and type of flow pattern. Note: n.a. states for no applicable, there is no liquid phase at the anode outlet.

| Exp. # | Anode | | Type of flow [35] | Cathode | Type of flow [35] | Note |
|---|---|---|---|---|---|---|
| | $u_{in,g,ano}$ ($m \cdot s^{-1}$) | $u_{out,l,ano}$ ($m \cdot 10^{-5} \cdot s^{-1}$) | | $u_{in,g,cat}$ ($m \cdot s^{-1}$) | | |
| 1 | 0.78 | 6.35 | Two-phase | 5.69 | Single phase | Flooding |
| 2 | 1.41 | n.a | Single-phase | | | No flooding |
| 3 | 0.77 | 6.61 | Two-phase | | | Flooding |
| 4 | 1.38 | n.a. | Single-phase | | | No flooding |
| 5 | 0.82 | 7.37 | Two-phase | | | Flooding |
| 6 | 1.46 | n.a. | Single-phase | | | No flooding |
| 7 | 0.80 | 6.35 | Two-phase | | | Flooding |
| 8 | 1.45 | n.a. | Single-phase | | | No flooding |

### *3.4.3.2. Effect of pressure*

Figure 3.9 depicts the effect of increasing the pressure for no flooding experiments #2 ($P_{ano}$ = 0.100 MPa) and #6 ($P_{ano}$ = 0.130 MPa). The slight increase in pressure was related to an increase in performance for most of the segments with both CDD diagrams having similar shapes. The corresponding numerical values for the current density of each segment are presented in Table 6. It was observed that the local performance increased slightly close to the air inlet (row 4) and the zone with better humidification (row 3 and onwards, except for the segment with maximum value). In the experiment with $P_{ano}$ = 0.130 MPa, the current increased a maximum of 40 mA close to the anode outlet but decreased approx. 10 mA in the segments close to the anode inlet.

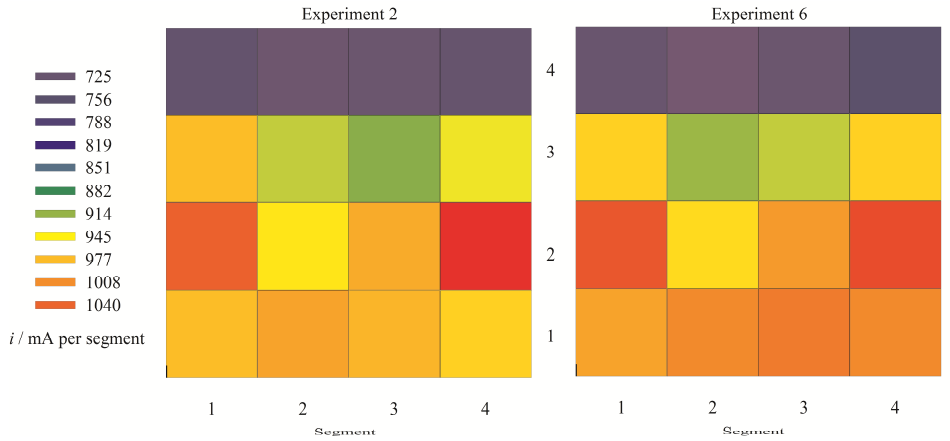


Figure 3.9. Current density distribution diagrams for experiments #2 ($P_{ano}$ = 0.110 MPa, $I$ = 14.5 A) and #6 ($P_{ano}$ = 0.130 MPa, $I$ = 14.6 A) and for 600 mV cell voltage. Other experimental conditions are as in Table 4.

For the case presented here, it would be expected an increase in performance due to a decrease in the ohmic resistance, once the cell was operating in the linear zone of the polarization curve as shown in Figure 3.6. Nevertheless, the fuel cell's high frequency resistance obtained by EIS for both experiments (not presented here) showed almost identical values, suggesting that the membrane resistance was practically the same. In turn, the theoretical increase in the thermodynamic voltage resulting from the increase in pressure was estimated at 3 mV [41]. However, the uneven increase in current at higher operating pressure indicates that the overpotentials were not equally decreased in a segment to segment basis and that actually increased slightly in others. Ultimately, the increase in performance for most of the segments was attributed to the local decrease in activation, permeability and diffusion overpotentials as reported recently by Reshetenko *et al.* [48] for a SFC operating at 60 °C.

### *3.4.3.3. Effect of purge cycle*

Figure 3.10 depicts the effect of purge cycle for no flooding Experiments #2 (purge cycle = 60/1 s) and #4 (purge cycle = 240/1 s). It was observed that increasing the purge cycle led to a less homogeneous CDD. The corresponding numerical values for the current density of each segment are presented in Table 6. This means that

water tends to stagnate in the cell when the time between purges increases. The latter was attributed to the four-fold increase in the amount of water coming from the cathode when the purge cycle was increased from 60/1 s, (0.48 $kg_{H2O} \cdot 10^{-6}$) to 240/1 s (1.92 $kg_{H2O} \cdot 10^{-6}$).

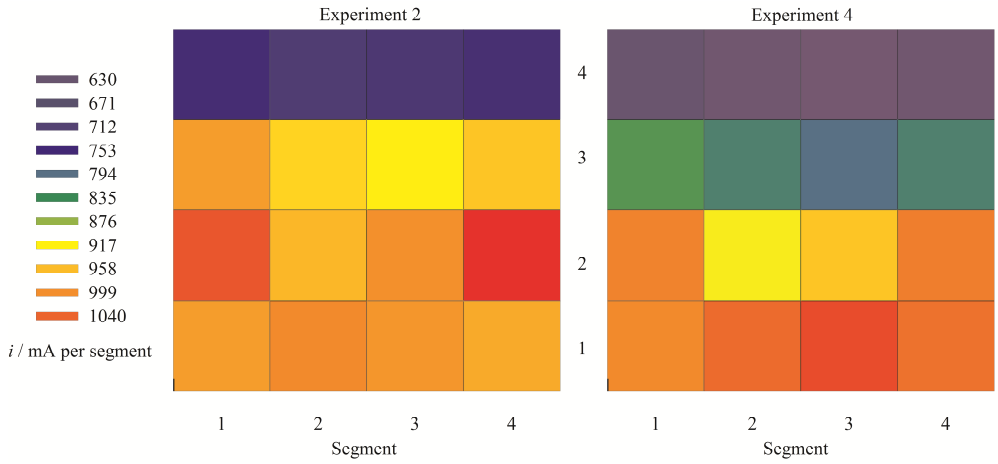


Figure 3.10. Current density distribution diagrams for experiments #2 (purge cycle = 60/1 s, *I* = 14.5 A) and #4 (purge cycle = 240/1 s, *I* = 13.6 A) and for 600 mV cell voltage. Other experimental conditions are as in Table 4.

The main purpose of the purge is to vent the nitrogen accumulated in the anode loop, preventing fuel starvation, and assist in removing the water. With every purge cycle, some hydrogen is also vented along with the nitrogen; because of this there is always a compromise between the waste of hydrogen (if the purge valve is more frequently open) and the possibility of degrading the catalyst layers as a consequence of local fuel starvation (if the purge valve is less frequently open). For the experiments performed here, the purge cycle was not optimized; nevertheless, it was clear that increasing the purge cycle had implications on the water removal capabilities of the anode.

## 3.5. Conclusions

A test bench was built around a segmented PEMFC operated in hydrogen recirculation mode with continuous removal of water. The test bench capabilities include fundamental electrochemical analysis as well as current density distribution,

water balance and nitrogen crossover measurements at the single cell level. Improvements of the test bench include incorporation of a humidification device to the anode recirculation loop, refinement of the purge system regarding the amount of gas purged and incorporation of other ways to trigger the purge (i.e., based on the voltage-drop of the cell or pressure-drop of the anode).

The concept of partially segmented bipolar plates was introduced and applied. With the partial segmentation, the lateral resistance between adjacent segments increased 14% to 21%. The partial segmentation led to a 17% decrease on the through-plane to in in-plane ratio of each segment. It was estimated that the increase in lateral resistance may go up to 44% to 70% while the decrease on the trough-plane to in-plane ratio may go up to 40% if deeper grooves for partial segmentation are used The major advantage of the partially segmented bipolar plates is a decrease in the lateral current spreading while at the same time avoiding their total segmentation. In contrast, the major disadvantage is the decrease in mechanical strength of the bipolar plates.

Representative anode parameters, namely, recirculated gas flow rate, pressure and the time between purges, were varied to analyze their effect on the current density distribution of a segmented PEMFC. Two different current density distribution diagram shapes were observed for the two different gas recirculation flow rates used, $V_{rel}$ = 5%, and $V_{rel}$ = 17.5%. When the gas recirculation rate was lower, a maximum in the current density distribution appeared up in the flow fields, decreasing towards the anode outlet, indicating flooding conditions towards the outlets. When the gas recirculation rate was higher, there was a decrease in performance close to the inlets but homogeneous current density distribution afterwards, indicating drying conditions at the inlets. The anode pressure and time between purges did not change to a great extent the shape of the current density distribution diagrams; however, water and nitrogen accumulation would seriously affect the performance of PEMFC operated in recirculation mode if the time between purges is not optimized.

Two complementary approaches were used to determine the likelihood of flooding in the cell: one based on a water balance analysis and the other based on the empiric flow map proposed by Hussaini and Wang [35]. It was noted that flooding conditions resulted from the impossibility of the anode to remove water diffusing from the cathode, leading to water condensation at the cathode and the anode. In turn, drying conditions resulted from excessive removal of water diffusing from the cathode close to the inlets, nonetheless, the higher flow rates provided more water removal capabilities to the anode, avoiding flooding towards the outlets of the flow fields. The empiric flow map predicted a single-phase flow pattern at the cathode for all experiments. In turn, the empiric flow map predicted a two-phase flow at the anode for the low recirculation experiments and single-phase flow pattern at the anode for the high recirculation experiments.

## 3.6. Acknowledgments

Luis C. Pérez is grateful to FCT for his PhD grant reference SFRH/BD/44684/2008. Financial support by FCT through projects PTDC/EQU-EQU/70574/2006 and PTDC/EQU-EQU/104217/2008 is also acknowledged.

## 3.7. References

[1] M. M. Mench, in *Fuel Cell Engines*, John Wiley & Sons, Inc., 2008, pp. 285-379.

[2] N. Yousfi-Steiner, P. Moçotéguy, D. Candusso, D. Hissel, *Journal of Power Sources* 2009, *194*, 130-145.

[3] K. Jiao, X. Li, *Progress in Energy and Combustion Science* 2011, *37*, 221-291.

[4] S. Ge, C.-Y. Wang, *Journal of the Electrochemical Society* 2007, *154*, B998-B1005.

[5] J. B. Siegel, D. A. Mckay, A. G. Stefanopoulou, D. S. Hussey, D. L. Jacobson, *Journal of the Electrochemical Society* 2008, *155*, B1168-B1178.

[6] J. T. A. Zawodzinski, T. E. Springer, J. Davey, R. Jestel, C. Lopez, J. Valerio, S. Gottesfeld, *Journal of The Electrochemical Society* 1993, *140*, 1981-1985.

[7] S. D. Knights, K. M. Colbow, J. St-Pierre, D. P. Wilkinson, *Journal of Power Sources* 2004, *127*, 127-134.

[8] I. A. Schneider, D. Kramer, A. Wokaun, G. G. Scherer, *Electrochemistry Communications* 2005, *7*, 1393-1397.

[9] R. J. Bellows, M. Y. Lin, M. Arif, A. K. Thompson, D. Jacobson, *Journal of the Electrochemical Society* 1999, *146*, 1099-1103.

[10] I. Manke, C. Hartnig, M. Grunerbel, W. Lehnert, N. Kardjilov, A. Haibel, A. Hilger, J. Banhart, H. Riesemeier, *Applied Physics Letters* 2007, *90*, 174105-174103.

[11] X. G. Yang, F. Y. Zhang, A. L. Lubawy, C. Y. Wang, *Electrochemical and Solid-State Letters* 2004, *7*, A408-A411.

[12] T. Sasabe, S. Tsushima, S. Hirai, K. Minami, K. Yada, *ECS Transactions* 2009, *25*, 513-521.

[13] S. Tsushima, K. Teranishi, S. Hirai, *Electrochemical and Solid-State Letters* 2004, *7*, A269-A272.

[14] S. Tsushima, S. Hirai, *Progress in Energy and Combustion Science* 2011, *37*, 204-220.

[15] L. C. Pérez, L. Brandão, J. M. Sousa, A. Mendes, *Renewable and Sustainable Energy Reviews* 2011, *15*, 169-185.

[16] F. Barbir, in *PEM Fuel Cells*, Academic Press, Burlington, 2005, pp. 115-145.

[17] M. Ferraro, F. Sergi, G. Brunaccini, G. Dispenza, L. Andaloro, V. Antonucci, *Journal of Power Sources* 2009, *193*, 342-348.

[18] J. Marcinkoski, B. D. James, J. A. Kalinoski, W. Podolski, T. Benjamin, J. Kopasz, *Journal of Power Sources* 2011, *196*, 5282-5292.

[19] R. Eckl, R. Grinzinger, W. Lehnert, *Journal of Power Sources* 2006, *154*, 171-179.

[20] W. Dai, H. Wang, X.-Z. Yuan, J. J. Martin, D. Yang, J. Qiao, J. Ma, *International Journal of Hydrogen Energy* 2009, *34*, 9461-9478.

[21] H. Karimäki, L. C. Pérez, K. Nikiforow, T. M. Keränen, J. Viitakangas, J. Ihonen, *International Journal of Hydrogen Energy* 2011, *36*, 10179-10187.

[22] D. Ferreira, R. Magalhães, P. Taveira, A. I. Mendes, *Industrial & Engineering Chemistry Research* 2011, *50*, 10201-10210.

[23] S. J. C. Cleghorn, C. R. Derouin, M. S. Wilson, S. Gottesfeld, *Journal of Applied Electrochemistry* 1998, *28*, 663-672.

[24] D. Natarajan, T. Van Nguyen, *Journal of Power Sources* 2004, *135*, 95-109.

[25] I. A. Schneider, H. Kuhn, A. Wokaun, G. G. Scherer, *Journal of the Electrochemical Society* 2005, *152*, A2092-A2103.

[26] A. Hakenjos, K. Tüber, J. O. Schumacher, C. Hebling, *Fuel Cells* 2004, *4*, 185-189.

[27] B. Sompalli, B. A. Litteer, W. Gu, H. A. Gasteiger, *Journal of the Electrochemical Society* 2007, *154*, B1349-B1357.

[28] M. Noponen, J. Ihonen, A. Lundblad, G. Lindbergh, *Journal of Applied Electrochemistry* 2004, *34*, 255-262.

[29] A. Hakenjos, H. Muenter, U. Wittstadt, C. Hebling, *Journal of Power Sources* 2004, *131*, 213-216.

[30] A. Dimensions, *can be found under www.airdimensions.com/ADISampleDesign.pdf, 2012.*

[31] S. S. Kocha, J. D. L. Yang, J. S. Yi, *Aiche Journal* 2006, *52*, 1916-1925.

[32] C. Mittelsteadt, M. Umbrell, *ECS Meeting Abstracts* 2006, *501*, 770-770.

[33] FC™–Series Humidifiers, *can be found under www.permapure.com/products/humidifiers/fc-series-humidifiers/?ind=fuelcell&prod=676, 2012.*

[34] X. Z. Yuan, H. J. Wang, J. C. Sun, J. J. Zhang, *International Journal of Hydrogen Energy* 2007, *32*, 4365-4380.

[35] I. S. Hussaini, C.-Y. Wang, *Journal of Power Sources* 2009, *187*, 444-451.

[36] H. Lin, T.-F. Cao, L. Chen, Y.-L. He, W.-Q. Tao, *International Journal of Hydrogen Energy* 2012, *37*, 11871-11886.

[37] F. P. Incropera, D. P. DeWitt, (Ed.: I. John Wiley & Sons), 2002, pp. 87-182.

[38] A. Nishimura, K. Shibuya, A. Morimoto, S. Tanaka, M. Hirota, Y. Nakamura, M. Kojima, M. Narita, E. Hu, *Applied Energy* 2012, *90*, 73-79.

[39] J. P. Owejan, J. J. Gagliardo, S. R. Falta, T. A. Trabold, *Journal of the Electrochemical Society* 2009, *156*, B1475-B1483.

[40] D. Lee, J. Bae, *International Journal of Hydrogen Energy* 2012, *37*, 422-435.

[41] M. M. Mench, *Fuel Cell Engines*, John Wiley & Sons, Inc., New Jersey, 2008.

[42] G. J. M. Janssen, M. L. J. Overvelde, *Journal of Power Sources* 2001, *101*, 117-125.

[43] Y. Cai, J. Hu, H. Ma, B. Yi, H. Zhang, *Electrochimica Acta* 2006, *51*, 6361-6366.

[44] T. Kim, S. Lee, H. Park, *International Journal of Hydrogen Energy* 2010, *35*, 8631-8643.

[45] G. Q. Lu, F. Q. Liu, C. Y. Wang, *Journal of Power Sources* 2007, *164*, 134-140.

[46] R. Anderson, L. Zhang, Y. Ding, M. Blanco, X. Bi, D. P. Wilkinson, *Journal of Power Sources* 2010, *195*, 4531-4553.

[47] M. Bruce, Y. Donald, O. Theodore, *Fundamentals of fluid mechanics*, John Wiley & Sons, Danvers, Massachusetts, 2002.

[48] T. V. Reshetenko, G. Bender, K. Bethune, R. Rocheleau, *Electrochimica Acta* 2011, *56*, 8700-8710.

[49] W. Wagner, A. Pruss, Journal of Physical and Chemical Reference Data 2002, 31, 387-535.

# Chapter IV

# Chapter IV - Air bleed optimization studies[3]

## 4.1. Abstract

The use of hydrogen with lower quality than that specified in current regulation is an attractive option for stationary PEMFC power production. In this paper, the effect of CO is mitigated using air bleed levels up to 2% in an $H_2$ PEMFC fed with CO concentrations below 20 ppm. A methodology to optimize the air bleed levels is developed using a novel arrangement of cells coupled to a gas chromatograph. The methodology relies on evaluating the distributed performance of the cell and on determining the CO and $CO_2$ molar flow rates at the anode outlet. Furthermore, the amount of CO adsorbed onto the catalyst and the fraction of catalytic sites covered by CO are estimated. The results show that different parameters, such as the $H_2$ volumetric flow rate, CO concentration and air bleed level, influence both the steady state and dynamics of PEMFCs that operate with low quality hydrogen.

[3] The content of this chapter is adapted from: L.C. Pérez, T. Rajala, J. Ihonen, P. Koski, J.M. Sousa, A. Mendes, "Development of a methodology to optimize the air bleed in PEMFC systems operating with low quality hydrogen". International Journal of Hydrogen Energy, 38 (2013) 16286-16299.

## 4.2. Introduction

Nowadays, Polymer Electrolyte Membrane Fuel Cells (PEMFCs) are being introduced successfully in many niche markets [1, 2]. The main technical problems of PEMFCs have been solved, even if there is still room to improve their durability and reduce costs [3-6].

One of the remaining issues for wider market introduction is the cost of high purity hydrogen ($H_2$). For example, meeting the $H_2$ fuel specifications for road vehicles outlined in current regulation (ISO 14687-2:2012 and SAE J2719) increases the costs of purification and quality assurance since the total amount of impurities must be below 100 ppm. The use of low quality $H_2$ that does not fulfill current regulation would be an attractive option to reduce the operating costs associated with the fuel for specific applications, e.g. stationary power generation. However, this would increase the capital cost of the PEMFC system. That is why understanding the effect of impurities and their mitigation techniques is a key issue to reduce the total cost of ownership [7] of PEMFCs.

Carbon monoxide (CO) has attracted most attention among various impurities such as hydrogen sulfide ($H_2S$), ammonia ($NH_3$) or carbon dioxide ($CO_2$,) for two reasons. First, it is the compound that most often constrains the fuel purification process [8]. Second, CO decreases the performance of PEMFCs as it reduces the active area of the membrane electrode assembly (MEA) due to its preferential adsorption onto the catalytic sites [9]. Furthermore, since the adsorption of CO is not homogeneous along the active area of the MEA, as reported in modeling studies [10, 11] and experimental studies using segmented PEMFCs [12-15], it is important analyzing the spatial distribution of CO within the cell.

Different techniques have been proposed to mitigate the effect of CO in PEMFCs, including: i) development of Pt-based binary or ternary catalysts [16], ii) voltage pulsing [17], iii) triode cell design [18], iv) external air bleed [19] and v) alternative anode configurations with external air bleed [20]. Another way to mitigate the effect

of CO is by increasing the catalyst loading [21], though this approach proportionally increases the catalyst cost.

All the mitigation techniques have pros and cons. For example, Pt-based binary or ternary catalysts enhance CO electrooxidation at lower anode overpotentials. Nonetheless, the most common binary catalyst (Pt-Ru) compromises PEMFC´s durability due to Ru dissolution and migration to the cathode [22, 23]. In turn, ternary catalysts still exhibit problems that concern their preparation and stability [16]. Voltage pulsing [17] and triode cell design [18] rely on alternative electrical circuitry configurations to promote electro oxidation of CO. However, they have only been demonstrated on a laboratory scale.

External air bleed is the most studied CO mitigation technique and relies on feeding $O_2$ (usually air) along with the fuel stream [19]. The external air bleed can be enhanced by impregnating the gas diffusion layer (GDL) with transition metal oxides that catalyze the CO oxidation [20]. Nonetheless, to date there are no commercial GDLs available to perform the latter. Drawbacks of the external air bleed include fuel efficiency reduction, overheating of the anode electrode and accelerated membrane degradation [24].

In addition to external air bleed, there is always some amount of $O_2$ that diffuses from the cathode during PEMFC operation. The latter is called “internal air bleed” and is enhanced with thin membranes and high cathode backpressures [25]. Apart from the drawbacks of the external air bleed, the issues with the internal air bleed relate to the difficulty of optimizing it for different CO concentrations and that $O_2$ may not diffuse uniformly along the MEA active area, which may lead to severe local poisoning of the catalyst.

Table 9 summarizes the most important findings of several external air bleed studies that can be found in the literature [12, 22, 26-33]. In general, the scope of the reviewed manuscripts was PEMFCs for stationary power applications operated between 60 °C and 90 °C with Pt-Ru as the anode catalyst. Within the manuscripts, the $C_{CO}$ and air bleed varied between 10 ppm and 10000 ppm and between 0.5% and 20% respectively. Most of the measurements were done using actual reformate or

simulated reformate gas [12, 22, 28, 29, 31-33], and only few with $H_2$-CO mixtures [26, 27, 30].

The main problem with the results summarized in Table 9 is that they do not provide definitive values or a guideline to estimate the amount of external air bleed needed to mitigate the effect of CO in PEMFCs. Moreover, the advantage of using Pt-Ru (over Pt) is not clearly observed and the CO and $CO_2$ concentrations at the anode exit were not measured. The latter makes it impossible to estimate the conversion of CO to $CO_2$ due to the external air bleed and to identify other sources of $CO_2$ (i.e., crossing over from the cathode) at the anode.

It is important to highlight a recent review paper [34] that addresses the problem of Ru dissolution and its possible solutions. However, external air bleed may still be applicable in PEMFC systems with Pt-Ru as anode catalyst depending on the amount of CO considered in the $H_2$ fuel specification for PEMFC stationary applications (ISO/DIS 14687-3 – enquiry stage).

In this paper, a methodology is introduced to optimize the amount of air bleed in PEMFCs subjected to a continuous feed of CO. The methodology relies on a new arrangement of single cells, which has similarities to a segmented PEMFC [35], and on measuring the CO and $CO_2$ concentrations of the anode exhaust gas with a gas chromatograph (GC). The segmented PEMFC is based on a multisinglecell (MsC) used previously to study novel coatings for bipolar plates [36, 37]. The CO and $CO_2$ molar flow rates are used to determine the amount of CO adsorbed onto the catalyst and the fraction of catalytic sites covered by CO.

The dynamic response of the segmented PEMFC is evaluated for the following scenarios: i) severe CO poisoning, where the CO breakthrough is highlighted, ii) amount of air bleed level needed to recover a desired percentage of original performance after the introduction of CO and iii) the effect of $H_2$ volumetric flow rate on both CO poisoning and air bleed effectiveness.

Table 9 - Summary of literature review on external air bleed levels for PEMFCs.

| $T_{cell}$ (°C) | Anode catalyst and loading | $C_{CO}$ (ppm) | Air bleed (%) | Observations | *Ref.* |
|---|---|---|---|---|---|
| 60 | Pt, 0.6 mg·cm$^{-2}$ and Pt-Ru, 0.6 mg·cm$^{-2}$. | 100 | ≈ 2.5, 5, 7.5, 10, 15 ($O_2$ was used) | 5% and 10% air bleed to recover performance with Pt-Ru and Pt respectively | [26] |
| 70, 90 | Pt-Ru, 0.45 mg·cm$^{-2}$ | 500, 3000, 10000 | 5, 10, 15 | 5% air bleed was enough to recover performance using the lowest $C_{CO}$ | [27] |
| 65 | Pt-Ru, 0.45 mg·cm$^{-2}$ | 25, 52.7, 100 | 2, 4, 6, 8, 10, 15, 20 | 4% air bleeding dosed in 10 s intervals found to be acceptable for the lowest $C_{CO}$ (95% of performance recovered) | [28] |
| 60 | Pt, 0.4 mg·cm$^{-2}$ and Pt-Ru, 0.45 mg·cm$^{-2}$. | 10, 80 | 0,5, 1, 2, 3, 4 | Empirical value of 0.5% air bleed for every 10 ppm of CO independently of the anode catalyst | [12] |
| 60 | Pt-Ru, 0.45 mg·cm$^{-2}$ | 50, 100, 200, 300, 400 | 2 and 4 | The air bleed level needed was 0.25% for 10 ppm CO. | [31] |
| 60 | Pt-Ru, 0.45 mg·cm$^{-2}$ | 10 | 1 | Stable performance of PEMFC stack during 6 h | [29] |
| 65 | Pt, 0.6 mg·cm$^{-2}$ and Pt-Ru, 0.45 mg·cm$^{-2}$. | 10.1, 25, 52.7 | 2, 3, 4, 5, 6, 7, 8 | Optimum air bleed of 4% for the highest $C_{CO}$ and Pt-Ru. 3% air bleed was enough to recover more than 90 % of performance with Pt. | [30] |
| 65 | Pt-Ru, 0.45 mg·cm$^{-2}$ | 53 | 2, 3, 4, 5, 8, 10, 15, 20 | 5% air bleeding was enough to recover 90% of performance. | [32] |
| 75 | Pt-Ru, 0.04 mg·cm$^{-2}$, 0.1 mg·cm$^{-2}$ and 0.28 mg·cm$^{-2}$ | 10, 50, 500 | 1 and 3 | 1% air bleeding showed good stability for lowest catalyst loading and $C_{CO}$. | [22] |
| 65 | Not specified | 10 | 0.8 | Increased mass transport limitations after 11,000 h of tests | [33] |

## 4.3. Experimental

### 4.3.1. The arrangement of cells with similarities to a segmented PEMFC

Four single cells were stacked and their gas distribution configurations disposed so that each cell could be considered one segment of a segmented PEMFC [35]. The intention was that the stack could have a similar behavior than that of a segmented PEMFC with a total area of 100 $cm^2$ divided in four equal segments. Furthermore, the electrical configuration of the stack allows evaluating the performance of each cell simultaneously, as it should be for each segment in a segmented PEMFC.

The similarities between the stack and a segmented PEMFC were achieved by changing the original "in parallel" fuel distribution configuration of the MsC [36] to an "in series" configuration (Figure 4.1). The necessary fuel distribution paths located inside the bipolar plates were blocked so that the outlet of the anode of cell one was connected to the inlet of the anode of cell two and so on until cell four. Regarding the oxidant distribution, none of the paths were blocked, which led to the original "in parallel" configuration. Thereby, all the cathode inlets were connected internally, allowing quite even distribution of the oxidant to each cell and thus minimizing the inhomogeneities due to $O_2$ partial pressure drop.

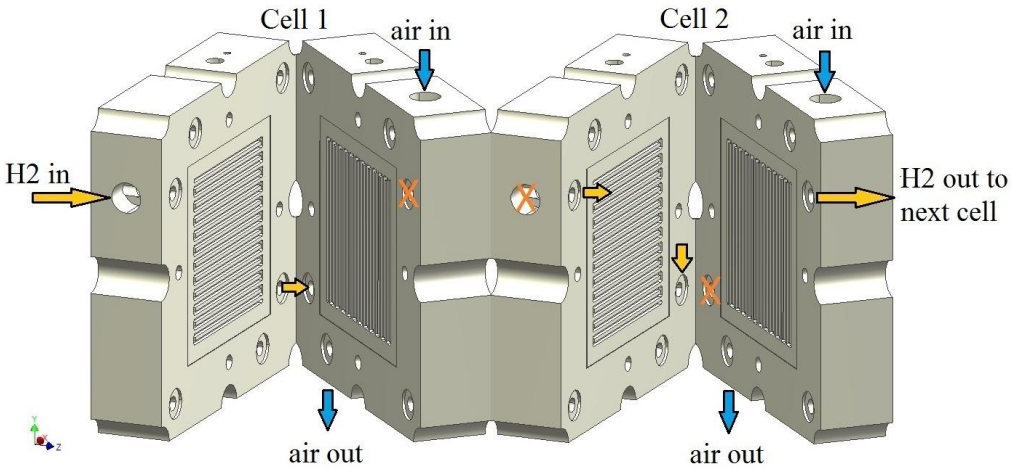


Figure 4.1. Detailed view of the reactants distribution in two cells of the stack. The crosses indicate the internal fuel distribution paths that were blocked so that the anodes were fed "in

series". Since none of the internal oxidant distribution paths were blocked, the cathodes were fed "in parallel".

The single cells comprised commercial MEAs with 25 $cm^2$ active area based on a 35 μm thick reinforced PEM loaded with 0.4 mg $Pt \cdot cm^{-2}$ on the anode and with 0.6 mg $Pt \cdot cm^{-2}$ on the cathode. The gas diffusion layers (Sigracet® SGL 35 BC, SGL technologies, Germany) were 325 μm thick and the gaskets (Model 35 FC-PO100, Freudenberg, Germany) were 350 μm thick. The clamping pressure was regulated using disc springs (Belleville, UK). The bipolar plates comprised single channel serpentine flow fields and were manufactured from graphite blocks (ISEM-3, Svenska Tanso, Sweden) with 88 mm length x 88 mm width x 20 mm thick.

### 4.3.2. Test station, data logging and gas chromatograph analysis

A test station (Arbin Instruments, USA) was used to control the $H_2$ and air volumetric flow rates, humidify the gases, and set the temperature of the MsC. The temperature of the MsC was measured with a K-type thermocouple inserted in the cathode of the second cell and controlled by circulating deionized water through special channels located at the back of the bipolar plates. The test station was also used to perform data logging of flow rates, temperatures, pressures and electric currents. All the mass flow controllers used for the tests were calibrated using a calibrator (Gilian®, Sensidyne, USA).

The anode was fed with $H_2$, a CO-$N_2$ mixture and air as sketched in Figure 4.2. If not otherwise indicated, the anode was fed with high purity $H_2$ (99.999%). CO was taken from a gas bottle (OY Aga Ab, Finland) containing a gas mixture with a concentration of 901 ppm of CO balanced with $N_2$ and fed using a mass flow controller (EL-FLOW®, Bronkhorst, The Netherlands). For the air bleed, synthetic air was produced with a zero air gas generator (Model 76-818, Whatman™, UK) and fed using a mass flow controller (EL-FLOW®, Bronkhorst, The Netherlands). The mass flow controllers for CO and synthetic air were connected to a digital power supply and control box (Series E-7000, Bronkhorst, The Netherlands). Check valves (C series, Swagelok®, USA) were inserted in the $H_2$ and air bleed pipelines to prevent upstream contamination with CO. The pressure drop in the cell was measured using two pressure transducers

(CTE7000 series, Sensor Technics, Germany) one located and the inlet and the other at the outlet of the anode.

The anode exhaust gas management is also depicted in Figure 4.2. The water contained in the exhaust gas was condensed using a heat exchanger. The gas stream was then splitted in two using a tee fitting, one of them was vented after passing through a water trap and the other further dried. A needle valve (Series AS, SMC, Japan) located downstream the tee fitting was used to regulate the flow of the stream of interest or "sample". Then, this sample stream was dried using a membrane module (FC™- Series, Perma Pure LLC, USA). To dry the sample, nitrogen ($N_2$) was passed through a pipe at 80 °C before being fed to the membrane module in counterflow to the sample at a volumetric flow rate of $Q_{N2} = 1$ $dm^3 \cdot min^{-1}$ using a rotameter (UK-040 series, Honsberg, Germany). The pressure was measured before the membrane module using a pressure transducer (Eclipse® series, Honeywell, USA) so it was possible to estimate the volumetric flow rate of the sample from the pressure drop between the anode outlet and this point. The relative humidity of the sample was measured after the membrane module using a relative humidity probe (Humicap 110®, Vaisala, Finland).

The cathode was fed with compressed air that was passed through a set of filters (2000 series, Parker Hannifin Corporation, USA) in order to remove particles, mist and trace compressor oil vapor. The pressure at the cathode inlet was measured using a pressure transducer (CTE7000 series, Sensor Technics, Germany). The cathode exhaust gas was passed through a water trap and vented.

One power supply (EX2020R, TTi, UK), one precision resistor and four loads (LD300, TTi, UK) were used to control the voltage of the cells. With this configuration, the voltage of each single cell (equivalent to one segment) was controlled simultaneously using the power supply while the current of each segment was measured simultaneously with each load. Similar electrical configurations for distributed performance evaluation have been reported by other authors [38, 39].

The CO and $CO_2$ concentrations of the anode exhaust gas were measured using a GC (6890 series, Agilent Technologies, USA) equipped with a flame ionization detector

and a 1.8 m chromatographic packed column (Porapak Q, Agilent Technologies, USA). The oven temperature of the GC was set to 80 °C. The analysis of each gas sample took approximately four minutes so 16 samples were automatically analyzed every hour. The GC was calibrated daily using a gas mixture (OY Aga Ab, Finland) with a concentration of 10.2 ppm of CO and 9.63 ppm of $CO_2$ balanced with He. A Matlab® routine that included integration of the CO and $CO_2$ peaks by a simple trapezoidal algorithm and noise filtering was implemented in order to facilitate analysis of the results.

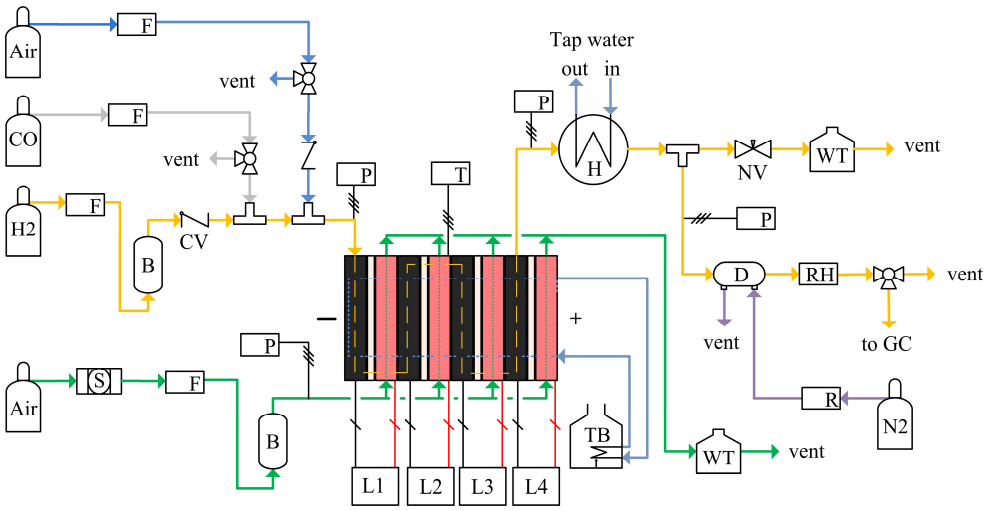


Figure 4.2. Sketch of the experimental setup. F, mass flow controller; B, bubbler; CV, check valve; P, pressure transducer; T, temperature transducer; H, heat exchanger; NV, needle valve, WT, water trap; D, dryer; RH, relative humidity probe: R, rotameter; GC, gas chromatograph; S, separators; L, load and TB, thermostatic bath.

### 4.3.3. Description of the tests procedure

Table 10 gives the operating conditions of the experiments performed. The MsC was operated in potentiostatic mode with constant fuel and oxidant volumetric flow rates. For all the experiments, the molar flow rate of CO at the anode inlet ($\dot{n}_{CO,in}$) was $7.3 \times 10^{-9}$ mol·s$^{-1}$, which is why the concentration of CO at the anode inlet ($C_{CO}$) varied between 13 and 19 ppm. In Experiment #1 the response of the cell to severe CO poisoning and high air bleed was studied. Experiment #2 was performed to determine the necessary air bleed level to recover 75% to 80% of the original performance of the cell by gradually increasing the air bleed. In Experiments #3, #4

and #5 the effect of the $H_2$ volumetric flow rate on both CO adsorption and air bleed effectiveness was analyzed. The MEAs and GDLs were replaced after Experiment #1 due to the severe CO poisoning conducted.

Table 10 - Operating conditions of experiments performed. Hydrogen and air flow rates are STP (273.15 K and 0.100 MPa).

| Exp # | $T_{cell}$ (°C) | $Q_{H2}$ ($cm^3\ min^{-1}$) | $C_{CO}$ (ppm) | $\dot{n}_{CO,in}$ (x $10^{-9}$ mol $s^{-1}$) | Air bleed (%) | $Q_{air}$ ($cm^3\ min^{-1}$) | $RH_{ano}$ $RH_{cat}$ (%) | $P_{ano}$ $P_{cat}$ (MPa) |
|---|---|---|---|---|---|---|---|---|
| 1 | 65 | 620.2 | 16 | 7.3 | 2 | 2489.2 | 100 | ≈ 0.101 |
| 2 | | 635.5 | 15 | | 0.6, 0.8, 1.0, 1.2, 1.4, 1.6 | 2521.8 | | |
| 3 | | 508.4 | 19 | | 0.8, 1.0, 1.2, 1.4 | | | |
| 4 | | 635.5 | 15 | | | | | |
| 5 | | 762.6 | 13 | | | | | |

For Experiments #2 to #5, the cell was stabilized for at least 45 min at $I_{tot} \approx 60$ A, before starting to feed the CO. The air bleed was applied when $I_{tot}$ was between 45 A to 48 A that is, when the current decreased 25% to 20%. Each air bleed step was maintained for 50 min. After the last air bleed value, the CO feed was stopped and the $I_{tot}$ recorded for 15 minutes. Finally, a $N_2$ purge of 15 minutes was implemented. The anode exhaust gas composition was analyzed throughout the tests. All experiments were repeated at least two times and the reproducibility of results was assessed.

### 4.3.4. Addressing the air bleed optimization based on molar flows

In the present study, it was necessary to estimate the molar flow rate of gaseous species entering and leaving the cell in order to achieve an optimized air bleed on a molar flows basis. A molar flow rate analysis approach was adopted rather than a concentrations analysis (ppm) to facilitate the quantification of the reaction processes, as recommended elsewhere [40]. The molar flow rates of $H_2$ fed to the anode, $\dot{n}_{H2}$ (mol $s^{-1}$), and the molar flow rate of oxygen fed to the cathode, $\dot{n}_{O2}$

(mol $s^{-1}$), were calculated from the Faraday's law and assuming 100% coulombic efficiency according to Eqs. 1 and 2:

$$\dot{n}_{H2} = \frac{I_{tot}}{2F} \quad (1)$$

$$\dot{n}_{O2} = \frac{I_{tot}}{4F} \quad (2)$$

where $I_{tot}$ (A) is the total current of the cell and $F$ is the Faraday constant, 96485.34 C $mol^{-1}$. The volumetric flow rate of $H_2$ fed to the anode, $Q_{H2}$ ($cm^3$ $s^{-1}$), and the volumetric flow rate of air fed to the cathode, $Q_{air}$ ($cm^3$ $s^{-1}$), were calculated using Eqs. 3 and 4:

$$Q_{H2} = \dot{n}_{H2} R \frac{T}{P} \lambda_{H2} \quad (3)$$

$$Q_{air} = \frac{\dot{n}_{O2}}{X_{O2}} R \frac{T}{P} \lambda_{O2} \quad (4)$$

where $R$ is the gas constant, 8.314 J $mol^{-1}$ $K^{-1}$, $T$ (K) is the temperature, $P$ (Pa) is the pressure, $\lambda_{H2}$ (dimensionless) is the $H_2$ stoichiometry, $X_{O2}$ is the molar fraction of oxygen in air, assumed to be 0.21, and $\lambda_{O2}$ (dimensionless) is the oxygen stoichiometry.

The concentration of CO at the anode inlet, $C_{CO,in}$ (ppm), and the molar flow rate of CO at the anode inlet, $\dot{n}_{\mathrm{CO},in}$ (mol $s^{-1}$), were calculated using the ideal gas law and the volumetric flow rate of CO at the anode inlet, $Q_{\mathrm{CO},in}$ ($cm^3$ $s^{-1}$), considering the inert balance gas and according to Eqs. 5-9:

$$Q_{in} = Q_{\mathrm{H2}} + Q_{mix} \quad (5)$$

$$Q_{mix} = Q_{\mathrm{N2}} + Q_{\mathrm{CO},in} \quad (6)$$

$$Q_{\mathrm{CO},in} = Q_{in} - Q_{\mathrm{H2}} - Q_{\mathrm{N2}} \quad (7)$$

$$C_{\mathrm{CO},in} = 10^6 \left(1 - \frac{Q_{\mathrm{H2}} + Q_{\mathrm{N2}}}{Q_{in}}\right) \quad (8)$$

$$\dot{n}_{\mathrm{CO},in} = \frac{\frac{Q_{\mathrm{CO},in}}{10^6} \times P}{RT} \quad (9)$$

where $Q_{in}$ ($cm^3\ s^{-1}$) is the sum of the volumetric flow rate of $H_2$ fed to the anode and the volumetric flow rate of the gas mixture containing CO, $Q_{mix}$ ($cm^3\ s^{-1}$) is volumetric flow rate of the gas mixture containing CO balanced with $N_2$ and $Q_{N2}$ ($cm^3\ s^{-1}$) is the volumetric flow rate of $N_2$ in the referred gas mixture.

The volumetric flow rate of air fed to the anode to perform the air bleed, $Q_{AB}$ ($cm^3\ s^{-1}$), was calculated as a percentage of the volumetric flow rate of $H_2$ fed to the anode while the molar flow rate of oxygen fed to the anode to perform the air bleed, $\dot{n}_{O2(AB)}$ (mol $s^{-1}$), was determined using the ideal gas law, Eqs. 10 and 11 respectively:

$$Q_{AB} = \frac{Q_{H2} \times AB\%}{100} \tag{10}$$

$$\dot{n}_{O2(AB)} = \frac{\frac{Q_{AB}}{10^6} \times P}{RT} \tag{11}$$

where *AB*% is the percentage of air bleed.

Finally, the molar flow rate of CO, $\dot{n}_{CO,out}$ (mol $s^{-1}$), and the molar flow rate of $CO_2$, $\dot{n}_{CO2,out}$ (mol $s^{-1}$), at the anode outlet were calculated from the concentration of CO, $C_{CO,out}$ (ppm), and the concentration of $CO_2$, $C_{CO2,out}$ (ppm) at the anode outlet, considering the $H_2$ consumed, $Q_{H2,cons}$ ($cm^3\ s^{-1}$), and the inert gas fed at the inlet, Eqs. 12-15:

$$Q_{out} = \left(Q_{H2} - Q_{H2,cons}\right) + Q_{N2} + Q_{N2(AB)} \tag{12}$$

$$Q_{H2,cons} = \frac{I_{tot} RT}{2FP} \tag{13}$$

$$\dot{n}_{CO,out} = \frac{Q_{out} \times C_{CO,out} \times P}{RT} \tag{14}$$

$$\dot{n}_{CO2,out} = \frac{Q_{out} \times C_{CO2,out} \times P}{RT} \tag{15}$$

where $Q_{out}$ ($cm^3\ s^{-1}$) is the volumetric flow rate of the gas mixture leaving the segmented cell in series and $Q_{N2(AB)}$ ($cm^3\ s^{-1}$) is the volumetric flow rate of $N_2$ from the air bleed.

## 4.4. Results and discussion

### 4.4.1. $CO_2$ sources at the anode inlet and outlet

Table 11 shows the $CO_2$ sources identified during the development of this study. It also contains recommendations on how to minimize their effect in the CO mass balance. Without careful identification of the $CO_2$ sources at the anode inlet and outlet, it would not be possible to plot $CO_2$ molar flow rate corresponding to the CO oxidation due to the external air bleed. Most of the $CO_2$ sources were identified using the GC.

The release of $CO_2$ dissolved in the anode humidifier water was observed as the experiments evolved. Specifically, $CO_2$ was released from the water during the operation of the cell at $I_{tot} \approx 60$ A. The last was observed as a continuous marginal decrease in the $CO_2$ concentrations, when no CO was yet fed to the cell. Depending on how often the humidifier was filled with "fresh water", it took more or less time for the $CO_2$ concentration to reach a steady state value.

Table 11 - Identified sources of CO2 at the anode inlet and outlet during the study.

| $CO_2$ sources | Action taken to minimize its effect and/or recommendation | Observations |
|---|---|---|
| Low purity $H_2$ (Anode inlet) | Use $H_2$ 5.0 (99.999% purity) or higher | Low purity $H_2$ may contain $CO_2$. Different $CO_2$ concentrations GC if $H_2$ bottles with different compositions are used. |
| Water of the anode humidifier (Anode inlet) | Fill the anode humidifier in the beginning of every experiment, then close water supply and allow for degassing | $CO_2$ may be dissolved in the water. Continuously decreasing $CO_2$ concentrations can be measured with the CG as the $CO_2$ is released. |
| Synthetic air used for air bleed (Anode inlet) | Use bottled synthetic air (80% $N_2$ and 20% $O_2$) or measure constantly the composition of the synthetic air produced on-site | The synthetic air used for the air bleed may contain different amounts of $CO_2$ depending on how it is produced. |
| Cathode (Anode outlet) | Quantify $CO_2$ crossover *in situ* or *ex situ* or use bottled synthetic air | $CO_2$ permeates from the cathode during PEMFC operation |

The $CO_2$ diffusing from the cathode was associated to the measured steady state $CO_2$ concentration after degassing the water present in the anode humidifier The $CO_2$ molar flow rate diffusing from the cathode was estimated to be $2.5 \times 10^{-9}$ mol $s^{-1}$, which is comparable to the value of $1.6 \times 10^{-9}$ mol $s^{-1}$ reported elsewhere [40].

The amount of $CO_2$ in the synthetic air was measured directly using the GC (230 ppm). The amount of $CO_2$ in the low purity $H_2$ was obtained from the gas supplier (20 ppm). It was assumed that the high purity $H_2$ did not contain $CO_2$, following the specification of the gas supplier (impurities: $H_2O \leq 3$ ppm, $O_2 \leq 2$ ppm, hydrocarbons $\leq 0.5$ ppm and $N_2 \leq 5$ ppm).

The contribution of internal air bleed to the oxidation of CO, which is another source of $CO_2$ at the anode, was neglected after comparing the parameters used in the present study with those of Wang [25]; for example: the lower operating temperature, thicker membrane, intermediate current densities and ambient cathode backpressure.

### 4.4.2. Response of the segmented PEMFC to severe CO poisoning and air bleed

The dynamic response of the segmented PEMFC to severe CO poisoning and high air bleed is shown in Figure 4.3 (Experiment #1). Interestingly, only after the current of segment 1 decreased almost to a steady state value, the current of segment 2 began a steep decrease ($t \approx 40$ min). Before the 2% air bleed was applied, it is clearly observed a pattern for the decrease in current for the segments. In the end of Experiment #1, the segmented PEMFC recovered 92% of its original current due to the air bleed (≈ 56 A).

The sequential decrease in current observed in Figure 4.3 for segments 1 and 2 showed a similar pattern for the other segments and was attributed to the preferential adsorption of CO onto the catalytic sites, which hindered the $H_2$ oxidation reaction (HOR). The pattern also suggests an adsorption front along the single channel serpentine flow fields and implies that, once the catalytic sites of the corresponding upstream segment are mostly covered by CO, the CO fed to the cell started to "breakthrough" to the corresponding downstream segment.

The term “breakthrough” was adopted in the present study due to its similarity of the phenomenon observed here with that occurring in fixed-bed adsorption columns [41]. In practice, the last indicates that in PEMFCs feed with CO, the anode catalyst layer behaves as an adsorption column (CO filter) as long as there is no significant conversion of CO to $CO_2$ due to the internal or external air bleeding. The CO breakthrough is clearly observed on the molar flow rate estimations presented below.

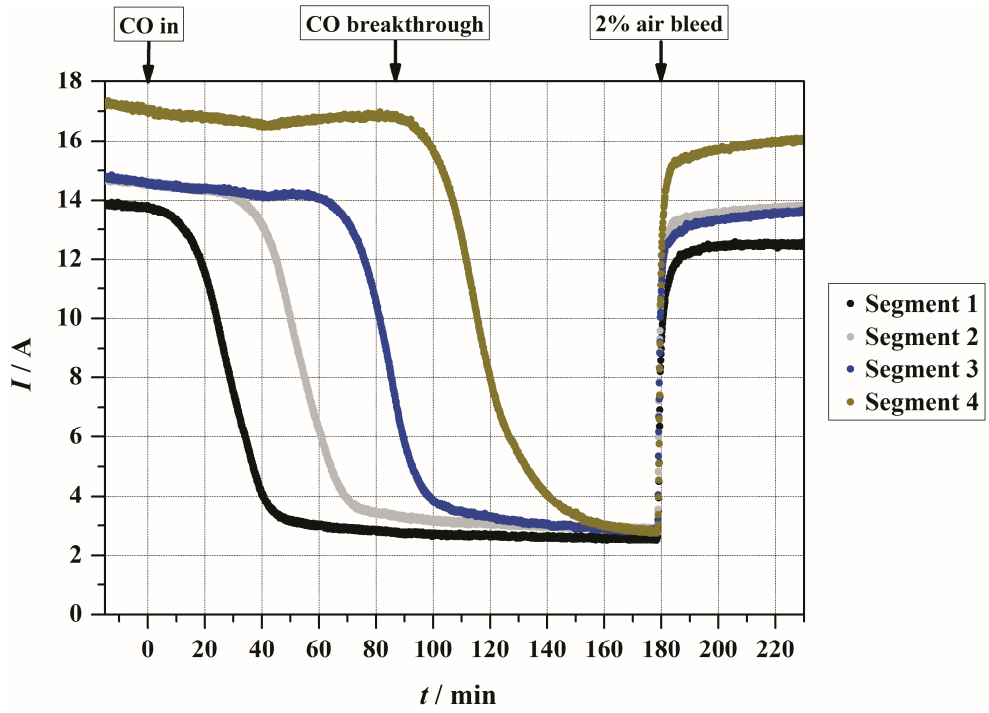


Figure 4.3. Response of the segmented PEMFC to severe CO poisoning and high air bleed. The CO concentration at the anode inlet was 16 ppm. Lower quality $H_2$ was used in this test (amount of impurities: $O_2$ < 20 ppm, $H_2O$ < 20 ppm, $CO_2$ < 20 ppm, $N_2$ < 500 ppm). Other experimental conditions as in Table 10.

Figure 4.4 shows the CO breakthrough curve for Experiment #1. The same time scales have been used to facilitate comparison with Figure 4.3. At $t$ = 86.3 min, the CO molar flow rate at the anode outlet started increasing gradually, indicating that the CO breakthrough was reached when the current of segment 3 decreased to 51% of its original value (7.5 A - Figure 4.3). The CO molar flow rate at the outlet reached a

maximum of 4.2 x $10^{-9}$ mol·$s^{-1}$ which was below the CO molar flow rate at the inlet, 7.3 x $10^{-9}$ mol·$s^{-1}$, indicating that approximately 43% of the CO continuously fed was still being adsorbed onto the catalytic sites at $t$ = 180 min. The latter is in accordance with a marginal decrease in performance observed in Figure 4.3 after $t$ = 160 min.

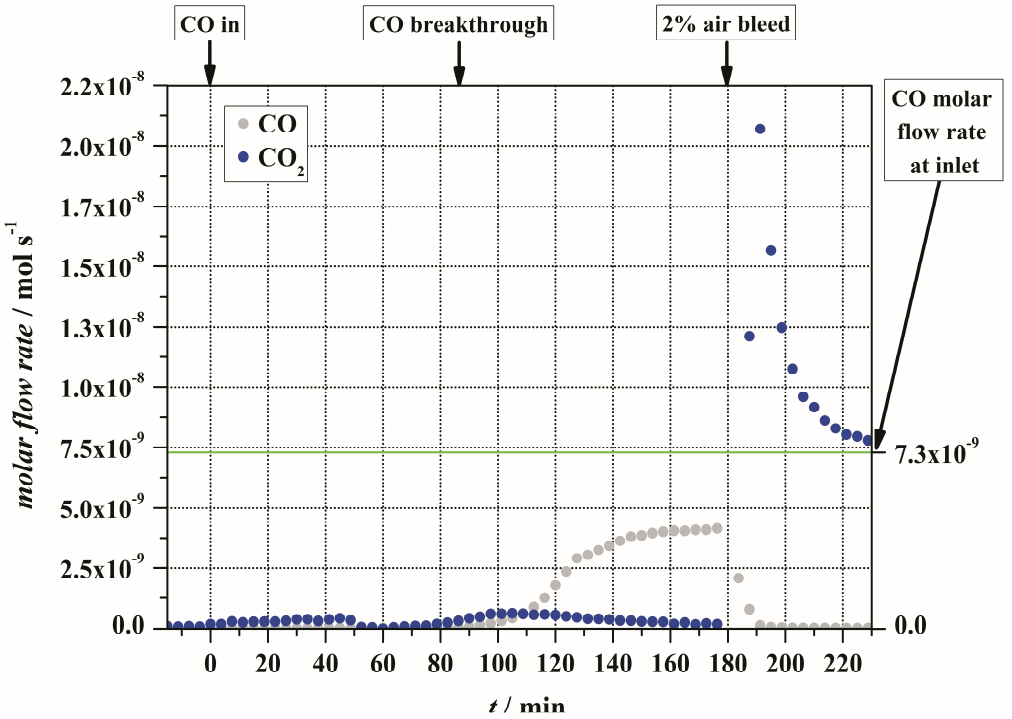


Figure 4.4. CO and $CO_2$ molar flows for experiment #1. The CO concentration at the anode inlet is 16 ppm. Lower quality $H_2$ (amount of impurities: $O_2$ < 20 ppm, $H_2O$ < 20 ppm, $CO_2$ < 20 ppm, $N_2$ < 500 ppm) was used in this test. Other experimental conditions as in Table 10.

It is also observed in Figure 4.4. that the $CO_2$ molar flow rate increased and decreased marginally until the CO breakthrough took place. The marginal increase in the $CO_2$ molar flow rate may indicate some CO electrooxidation, however, as it decreased after $t$ = 100 min no definitive explanation was found for this behavior by the authors.

In the same figure, a peak of $CO_2$ associated to the oxidation of CO was noticed after the air bleed was applied at $t$ = 183.8 min. By the end of Experiment #1 the $CO_2$ molar flow rate at the anode outlet remained 0.3 x $10^{-9}$ mol·$s^{-1}$ higher than the CO molar

flow rate at the inlet, suggesting that all the CO fed at the anode inlet plus a small amount of the CO that adsorbed in the catalyst before the air bleed took place was being oxidized.

Further analysis of Figures 4.2 and 4.3 indicate that PEMFCs with relatively high anode Pt loading (e.g. 0.4 mg $cm^{-2}$) can operate at quite high power levels the first tens of minutes without air bleed. The last was demonstrated in the present work and indicates that the air bleed may not be necessary if the objective is to generate power for short periods of time. This was also observed in other studies [21], which highlighted how lower anode Pt loadings, led to a faster decline in PEMFC performance for the same $C_{CO}$.

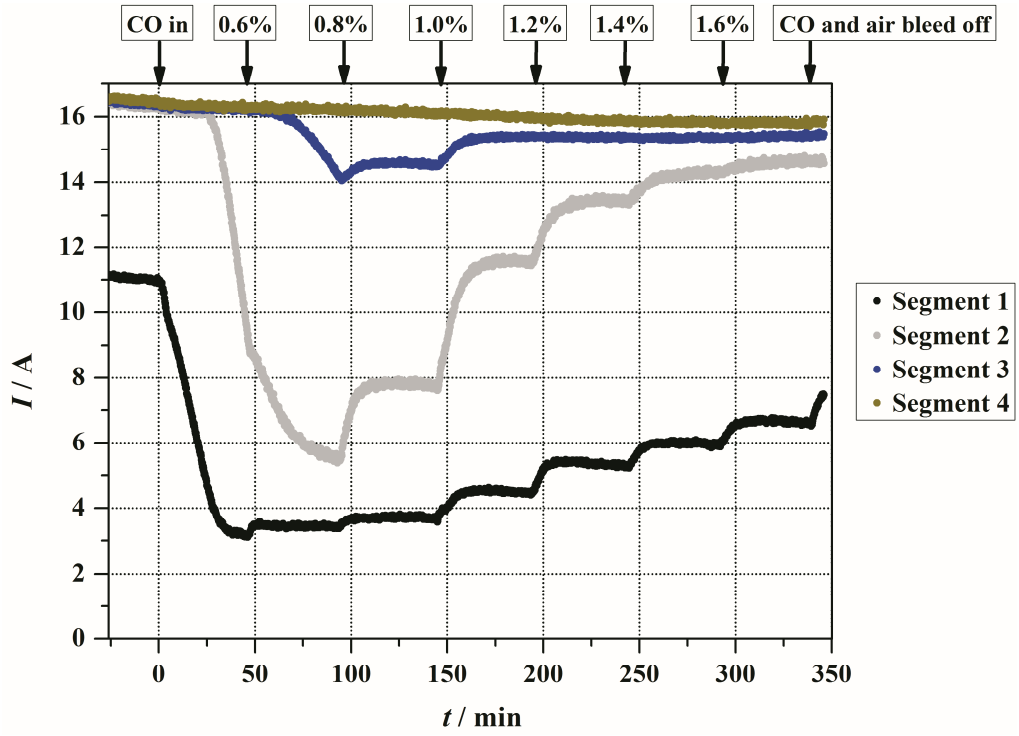


Figure 4.5. Segments current response to gradual increase in air bleed (experiment #2). The CO concentration the anode inlet was 15 ppm. Other experimental conditions as in Table 10.

It was previously observed that PEMFCs may operate without noticeable loss in performance in the absence of air bleed. However, if the PEMFC system is operated longer than few tens of minutes, it would be necessary to apply an optimized air bleed depending on the estimated power demand.

Figure 4.5 shows the amount of air bleed needed to recover 75% to 80% of the original current by gradually increasing the air bleed (Experiment #2). It is clearly observed that 0.6% air bleed already partially mitigated the effect of CO in segment 2 and stopped the decrease in performance of segment 1. However, this level of air bleed was not enough to stop the decrease in performance of segment 3. The last indicates that 0.6% air bleed was not enough to stop the CO breakthrough between segments 2 and 3.

When the air bleed was increased to 0.8%, the decrease in performance of segments 2 and 3 was stopped. It is evident that 0.8% air bleed was enough to stop the CO breakthrough between the segments but not to recover the desired level of performance (75% to 80% of the original current). The desired current was recovered when 1% air bleed was applied and gradually overpassed as the air bleeding level reached 1.6%.

It can be seen from Figure 4.5 the performance of segment 1 was 30% lower compared to the other cells that in the beginning of the experiment. Unfortunately, cell 1 was damaged due to temporary restriction in the anode humidifier water supply.

The $CO_2$ molar flow rate response in Figure 4.6 depicts how CO continuously adsorbs onto the catalyst and is oxidized to $CO_2$ when the air is applied (Experiment #2). The same time scales were used to facilitate comparison with Figure 4.5. No CO was detected during the experiment, which indicates that the CO fed continuously to the cell was either adsorbed onto the catalyst or oxidized to $CO_2$.

Between $t = 0$ and $t = 100$ min, the CO adsorbed (accumulated) onto the catalyst, even though 0.6% air bleed was applied at $t = 52.5$ min. This is in good agreement with the results in Figure 4.5 since 0.6% air bleed was not enough to stop the decrease in performance of segment 3. The linear increase in $CO_2$ molar flow rate suggests that a longer measurement with 0.6% air bleed would be needed in order to confirm the possibility of complete oxidation of the CO fed continuously to the cell.

A steady $CO_2$ molar flow rate was observed when 0.8% air bleed was applied (Figure 4.6), which is again in good agreement with a steady state cell performance observed

in Figure 4.5 between $t$ = 97.5 min and $t$ = 146.3 min. This result indicates that 0.8% air bleed was enough to oxidize the CO fed continuously to the cell so that no net accumulation of CO on the catalyst surface was taking place.

When higher air bleeds were applied (> 1%), a sudden increase followed by a decrease in the $CO_2$ molar flow rate was observed for each successive air bleed value – Figure 4.6. Since the $CO_2$ molar flow rates were always higher than $7.3 \times 10^{-9}$ mol·s$^{-1}$, this behavior was associated to the oxidation of the CO that was adsorbed onto the catalyst surface before $t$ = 97.5 min.

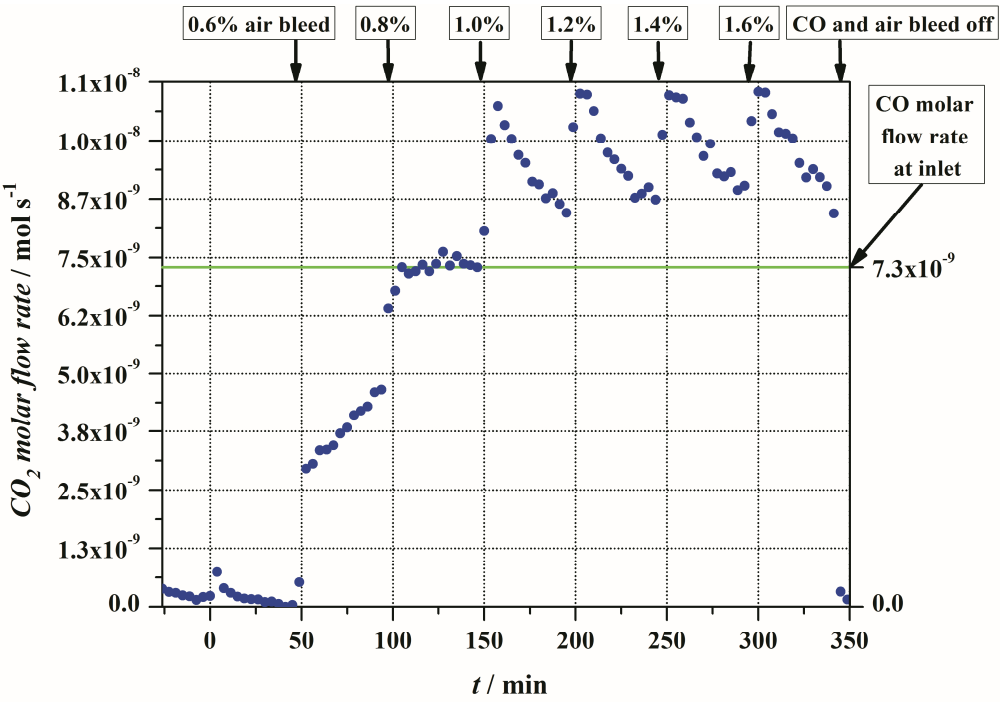


Figure 4.6. $CO_2$ molar flow rate responses to gradual increase in air bleed (Experiment #2). The CO concentration the anode inlet is 15 ppm. Other experimental conditions as in Table 10. No CO was detected at the anode outlet.

The analysis of Figures 4.5. and 4.6. clearly highlights three trends for CO oxidation when air bleed is applied: accumulation – insufficient air bleed, steady state – enough air bleed to oxidize the CO fed continuously to the cell – and removal – active oxidation of previously adsorbed CO.

### 4.4.3. Quantitative analysis of CO adsorption, breakthrough and oxidization

A more detailed quantification of the amount of CO adsorbed onto the catalyst surface would help to estimate the fraction of catalytic sites covered by CO which can be useful in determining the catalyst utilization factor and the catalyst effectiveness factor [42] if desired.

The quantification of CO is a challenging task as it is necessary to consider accurately all exogenous sources of $CO_2$ (Section 3.1) before performing a mass balance involving the amount of CO adsorbed, CO that slipped due to the breakthrough and CO oxidized. Great effort has been put by other groups to assess the CO mass balance in PEMFCs [40, 48]. Nonetheless this is the first time, to the knowledge of the authors, that the CO oxidized due to external air bleed is included in such analysis. An attempt to estimate the amount of CO (mol) adsorbed onto the catalyst surface and the fraction of catalytic sites covered by CO for Experiments #1 and #2 was performed below.

The CO mass balance was achieved using the information of Figures 4.4 and 4.6. It was first necessary to discriminate the time periods when the CO was adsorbing, oxidizing or slipping due to breakthrough. After this, the areas under each curve were delimited, each of which corresponded to an amount of CO. Finally, the amount of CO was determined following a fitting and integrating process for every single area.

Figure 4.7 highlights the areas considered to perfrom the CO mass balances for Experiments #1 and #2. Whenever the CO molar flow rate was below $7.3 \times 10^{-9}$ mol·s$^{-1}$, either the CO was adsorbed ($A_1$ – Figure 4.7a) or the CO breakthrough occurred ($A_2$ – Figure 4.7a). It was assumed that above this value the $CO_2$ molar flow rate corresponded to the CO oxidized ($A_3$ – Figure 4.7a). The areas depicted in Figure 4.7b were delimited using the same assumptions; nonetheless, no CO breakthrough was observed here due to the characteristics of the experiment.

Figure 4.7. CO adsorbed and molar flow rates for: a) Experiment #1 and b) Experiment #2. The dashed lines in the molar flow rate plots delimit the areas under the curve considered to estimate the amount of CO adsorbed and the fraction of catalytic sites covered by CO ($\vartheta_{CO}$). Experimental conditions as in Table 10.

The amount of CO that remained adsorbed in the cell, $n_{CO,ads}$ (mol), at the end of Experiments #1 and #2 was estimated subtracting the amount of CO that slipped due to the breakthrough and/or CO oxidized from the CO adsorbed. The results of the subtraction were 3.35 $10^{-5}$ mol of CO for Experiment #1 and 1.68 $10^{-5}$ mol of CO for Experiment #2. Thus, the CO mass balance indicated that that ≈ 52% of the CO

remained adsorbed in the cell at the end of Experiment #1 and ≈ 39% at the end of Experiment #2. The amount of CO that remained adsorbed revealed that considerably less catalytic sites were necessary to deliver almost the same current than before starting the CO feed, as can be recalled from Fig. 4.3. and Fig. 4.5.

Figure 4.7 also shows the fraction of catalytic sites covered by CO, $\theta_{CO}$ (%) for Experiments #1 and #2. These values were calculated according to Eq. 16 which was adapted from Ref. [43]:

$$n_m = \frac{A}{a_m \times L} \tag{16}$$

where $n_m$ (mol $g^{-1}$), is the monolayer capacity, A ($m^2$ $g^{-1}$) is the specific surface area of the electrode, assumed to be 112 $m^2$ $g^{-1}$ [44], $a_m$ ($m^2$) is the average area occupied by one molecule of CO, assumed to be 1.68 $10^{-19}$ $m^2$ [45] and L ($mol^{-1}$) is the Avogadro constant. The specific surface area of the electrode assumed for Eq. 16 corresponds to a catalyst with 20% wt. Pt supported on Vulcan® XC-72, which is commonly used as reference in PEMFC research [46, 47]

It was observed from Figure 4.7a that the CO breakthrough started when $\vartheta_{CO}$ = 85%. However, by the end of Experiment #1 this value decreased to $\vartheta_{CO}$ = 76%. This indicates that in Experiment #1 approximately 10% of the catalytic sites were needed to recover the original current from 18% before and up to 92% after the air bleed was applied.

The results from Fig. 4.7b also indicate that approximately half of the catalytic sites were covered with CO when the total current of the cell was 75% of its original value; this is, before the air bleed was applied (Figure 4.5). By the end of Experiment #2 the fraction of catalytic sites covered by CO was $\vartheta_{CO}$ = 38% which is half of the value observed for Experiment #1. The last was attributed to the less severe poisoning of the former experiment.

### 4.4.4. Air bleed applied to different hydrogen volumetric flow rates

Different $H_2$ volumetric flow rates were tested to see how the dynamics of CO adsorption and the recovery by air bleed changed. Figure 4.8 shows how the distributed performance of the segmented PEMFC is affected by the $C_{CO}$, the $H_2$ volumetric flow rate influence and the amount of air bleed (Experiments #3, #4 and #5). Only the performances of segments 1, 2 and 3 were plotted since the response of segment 4 remained constant during all the experiments.

Figure 4.8. Normalized current ratios as a function of time for Experiments #3 (a – low $H_2$ flow rate), #4 (b – intermediate $H_2$ flow rate) and #5 (c – high $H_2$ flow rate). The molar flow rate of CO at the anode inlet was $7.3 \times 10^{-9}$ mol $s^{-1}$ for all experiments. Experimental conditions as in Table 10.

The normalized current ratio was adopted to facilitate comparison and because the current of segment 1 did not reach the same value in the beginning of each experiment. Other research groups have reported the same type of plots to highlight the effect of CO on operating PEMFCs [15, 21].

The response of segments 2 and 3 was different for every experiment when 0.8% air bleed was applied. With $C_{CO}$ = 19 ppm (low $H_2$ flow rate), 0.8% air bleed was not enough to stop the decrease in performance of segment 3, highlighting the CO breakthrough in segment 2. For $C_{CO}$ = 15 ppm (intermediate $H_2$ flow rate), 0.8% air bleed was also not enough to stop the decrease in performance of segment 3, however, the decrease in performance was less pronounced than in the previous case. With $C_{CO}$ = 13 ppm (high $H_2$ flow rate), 0.8% air bleed was enough to stop the decrease in performance of segment 3, indicating that the CO fed continuously to the cell was oxidized and that the CO breakthrough was stopped.

The results in Figure 4.8 show that the $H_2$ volumetric flow rate influences not only the extent and severity of CO poisoning but also the extent and effectiveness of air bleed along the active area of the MEA. It is observed that at lower $H_2$ volumetric flow rates, the severity of CO poisoning was more pronounced in segments 2 and 3. It is important to highlight that the air bleed was fixed to the $H_2$ volumetric flow rate so proportionally more O2 from the air bleed was fed to the cell at higher $H_2$ volumetric flow rates. However, the molar flow rate of CO at the anode inlet was the same for all experiments.

When looking for a reason to the results in Figure 4.8, it was found that the extent and severity of CO poisoning has been studied numerically [10, 11]. Those authors stated that the extent and severity of CO was influenced by two related parameters namely: the mean gas velocity (residence time) of the gas in the flow field channels [10] and the $H_2$ stoichiometric flow rate (decrease in $H_2$ partial pressure towards the anode outlet) [11]. The experimental results presented here suggest that at higher $H_2$ flow rates, the CO adsorption front extended further and faster downstream the anode flow field. In the same way, it can be said that less severe implications in the local performance were observed also for higher $H_2$ flow rates, which implies a more even distribution of CO inside the cell.

Figure 4.9 compares the $CO_2$ molar flow rates at the anode outlet for the cases with different $C_{CO}$ and $H_2$ volumetric flow rates (Experiments #3, #4 and #5). When 0.8% air bleed was applied to the cases with $C_{CO}$ = 19 ppm and 15 ppm (low and intermediate $H_2$ flow rates) the average $CO_2$ molar flow rates at the outlet were

$4.5 \times 10^{-9}$ mol·s$^{-1}$ and $6.8 \times 10^{-9}$ mol·s$^{-1}$. Both of these are below the CO molar flow rate at the inlet. The last implies that part of the CO fed continuously to the cell was still being adsorbed onto the catalyst surface, which is in agreement with the decrease in performance of segments 2 and 3 depicted in Figure 4.8.

As for the case with $C_{CO}$ = 13 ppm, the average $CO_2$ molar flow rate at the anode outlet was $7.8 \times 10^{-9}$ mol·s$^{-1}$, which is, higher than the CO molar flow rate at the inlet of $7.3 \times 10^{-9}$ mol·s$^{-1}$. The latter indicates that the CO feed continuously to the cell was being oxidized along with part of the CO previously adsorbed.

Figure 4.9. $CO_2$ molar flow rates at the anode outlet for experiments #3 (a – low $H_2$ flow rate), #4 (b – intermediate $H_2$ flow rate) and #5 (c – high $H_2$ flow rate). Experimental conditions as in Table 10.

Figure 4.9 also shows that above 1% air bleed, the CO fed continuously to the cell was also oxidized for the cases with $C_{CO}$ = 19 ppm and 15 ppm (low and intermediate $H_2$ flow rates) as the $CO_2$ molar flow rate at the anode outlet was > $7.3 \times 10^{-9}$ mol·s$^{-1}$, this is, the molar flow rate of CO at the anode inlet.

As stated in Section 1, there is a lack of definitive values or guidelines aiming to determine the necessary air bleed needed to mitigate the effect of CO in PEMFCs. For practical purposes, it would be interesting to determine these values based on ratios of different PEMFC operating parameters; for example, $H_2$ to $O_2$ from air bleed fed to the anode, $O_2$ from air bleed to CO or air bleed percentage to $C_{CO}$. Table 12 shows these ratios for the present study along with some observations related to how effective the air bleed was for Experiments #3, #4 and #5.

Table 12 - Hydrogen to oxygen, oxygen to carbon monoxide and air bleed to carbon monoxide concentration ratios for selected experiments and air bleed values.

| Exp. # | $Q_{H2}$ ($cm^3\ min^{-1}$) | Air bleed (%) | $C_{CO}$ (ppm) | $\dot{n}_{H2}/\dot{n}_{O2(AB)}$ | $\dot{n}_{O2(AB)}/\dot{n}_{CO}$ | Air bleed/$C_{CO}$ (% $ppm^{-1}$) | Obs. |
|---|---|---|---|---|---|---|---|
| 3 | 508.4 | 0.8 | 19 | 544 | 94 | 0.042 | Not enough to mitigate the effect of CO |
| | | 1.0 | | 436 | 117 | 0.053 | Enough to mitigate the effect of CO |
| 4 | 635.5 | 0.8 | 15 | 544 | 117 | 0.053 | Not enough to mitigate the effect of CO |
| | | 1.0 | | 436 | 147 | 0.067 | Enough to mitigate the effect of CO |
| 5 | 762.6 | 0.8 | 13 | 544 | 141 | 0.062 | Not enough to mitigate the effect of CO |
| | | 1.0 | | 436 | 176 | 0.077 | Enough to mitigate the effect of CO |

On Table 12, it can be observed that both Experiments #3 and #4 resulted in air bleed to $C_{CO}$ ratios of 0.053% $ppm^{-1}$ and oxygen to CO molar flow ratios of 117 when 1% and 0.8% air bleeds were applied, respectively. This made necessary to analyze the

distributed performance of the cell (Figure 4.8) and compare the average $CO_2$ molar flow rates at the anode outlet (Figure 4.9). The average $CO_2$ molar flow rates at the anode outlet for Experiment #3 with 1% air bleed was $7.9 \times 10^{-9}$ mol·s$^{-1}$ while for Experiment #4 with 0.8% air bleed was $6.0 \times 10^{-9}$ mol·s$^{-1}$. So that, the effect of CO was mitigated for Experiment #3 with 1% air bleed as expected. Finally, it is important to note that the only differences between Experiments #3 and #4 are the $C_{CO}$ and $Q_{H2}$. The latter highlights the importance of these two parameters when trying to mitigate the effect of CO using an external air bleed.

## 4.5. Conclusions

A methodology to determine the amount of air bleed needed to mitigate the effect of CO in PEMFCs was developed. The methodology is based on the analysis of the distributed performance of the cell and the estimation of the $CO_2$ molar flow rates at the anode inlet and outlet, which was assessed using a gas chromatograph.

It was demonstrated that this methodology is suitable for studying the following aspects: i) the amount of air bleed needed to recover a desired level of performance of PEMFCs with continuous CO feed, ii) the amount of air bleed needed to oxidize the CO feed on a molar flow basis for different $H_2$ flow rates, iii) the amount of CO adsorbed/desorbed during a certain period of time and iv) the fraction of catalytic sites covered by CO.

Some similarities between the adsorption of CO in operating PEMFC and fixed-bed adsorption columns were stressed. Hence, the term CO breakthrough was associated to the point where the CO could no longer accumulate onto the catalyst surface. The CO breakthrough determined the extent and severity of the CO adsorption onto the catalyst along the single channel serpentine flow fields.

It was observed that the flow rate of $H_2$ affects both the extent and severity of the CO adsorption as well as the effectiveness of the air bleed. In order to assess the minimum amount of air bleed needed to oxidize the CO feed, it was necessary to estimate the $CO_2$ molar flow rate at the anode outlet.

It was noted that the air bleed value to CO concentration ratio (% $ppm^{-1}$) or the oxygen to CO molar flow ratio at the anode inlet could be misleading approaches to find the minimum air bleed levels needed to oxidize the CO feed. For the cases studied here, the decrease in performance attributed to CO was mitigated whenever the $H_2$ to oxygen molar flow ratio at the anode inlet was < 544, the oxygen to CO molar flow ratio at the anode inlet was ≥ 117 and the air bleed to CO concentration ratio was ≥ 0.053% $ppm^{-1}$.

## 4.6. Acknowledgements

This research has been conducted under the "Fuel Cell 2007-2013" technology program of Tekes, the Finnish Funding Agency for Technology and Innovation.
Luis C. Pérez is grateful to FCT for his PhD grant reference SFRH/BD/44684/2008. Financial support by FCT through projects PTDC/EQU-EQU/104217/2008 and PTDC/CTM/108454/2008 is also acknowledged. Luis C. Pérez is also grateful to CONACyT for its support.

## 4.7. References

[1] Dicks AL. PEM Fuel Cells: Applications. In: Comprehensive Renewable Energy. Sayigh A, Cruden A, editors. Oxford: Elsevier Ltd; 2012, p. 203-245.

[2] Pollet BG, Staffell I, Shang JL. Current status of hybrid, battery and fuel cell electric vehicles: From electrochemistry to market prospects. Electrochim Acta 2012, 84:235-249.

[3] Yuan X-Z, Li H, Zhang S, Martin J, Wang H. A review of polymer electrolyte membrane fuel cell durability test protocols. J Power Sources 2011, 196:9107-9116.

[4] Yu Y, Li H, Wang H, Yuan X-Z, Wang G, Pan M. A review on performance degradation of proton exchange membrane fuel cells during startup and shutdown processes: Causes, consequences, and mitigation strategies. J Power Sources 2012, 205:10-23.

[5] Staffell I, Green R. The cost of domestic fuel cell micro-CHP systems. Int J Hydrogen Energy 2013, 38:1088-1102.

[6] Wang G. Advanced vehicles: Costs, energy use, and macroeconomic impacts. J Power Sources 2011, 196:530-540.

[7] Ellram LM. Total cost of ownership: an analysis approach for purchasing. Int J Phys Distrib Logist Manag 1995, 25:4 - 23.

[8] Besancon BM, Hasanov V, Imbault-Lastapis R, Benesch R, Barrio M, Mølnvik MJ. Hydrogen quality from decarbonized fossil fuels to fuel cells. Int J Hydrogen Energy 2009, 34:2350-2360.

[9] Zamel N, Li X. Effect of contaminants on polymer electrolyte membrane fuel cells. Prog Energy and Combust Sci 2011, 37:292-329.

[10] Brett DJL, Aguiar P, Brandon NP, Kucernak AR. Measurement and modelling of carbon monoxide poisoning distribution within a polymer electrolyte fuel cell. Int J Hydrogen Energy 2007, 32:863-871.

[11] Bonnet C, Franck-Lacaze L, Ronasi S, Besse S, Lapicque F. PEM fuel cell Pt anode inhibition by carbon monoxide: Non-uniform behaviour of the cell caused by the finite hydrogen excess. Chem Eng Sci 2010, 65:3050-3058.

[12] Tingelöf T, Hedström L, Holmström N, Alvfors P, Lindbergh G. The influence of CO2, CO and air bleed on the current distribution of a polymer electrolyte fuel cell. Int J Hydrogen Energy 2008, 33:2064-2072.

[13] Murahashi T, Mitsumoto T, Nishiyama E: Current Distribution of a PEMFC under CO Poisoning. ECS Transactions 2009, 25:869-879.

[14] Boaventura M, Sander H, Friedrich KA, Mendes A. The influence of CO on the current density distribution of high temperature polymer electrolyte membrane fuel cells. Electrochim Acta 2011, 56:9467-9475.

[15] Reshetenko TV, Bethune K, Rocheleau R. Spatial proton exchange membrane fuel cell performance under carbon monoxide poisoning at a low concentration using a segmented cell system. J Power Sources 2012, 218:412-423.

[16] Ehteshami SMM, Chan SH. A review of electrocatalysts with enhanced CO tolerance and stability for polymer electrolyte membarane fuel cells. Electrochim Acta 2013, 93:334-345.

[17] Adams WA, Blair J, Bullock KR, Gardner CL. Enhancement of the performance and reliability of CO poisoned PEM fuel cells. J Power Sources 2005, 145:55-61.

[18] Tsampas MN, Sapountzi FM, Divane S, Papaioannou EI, Vayenas CG. Triode operation of CO poisoned PEM fuel cells: Fixed and cyclic potential triode operation. Solid State Ionics 2012, 225:272-276.

[19] Gottesfeld S, Pafford J. A New Approach to the Problem of Carbon Monoxide Poisoning in Fuel Cells Operating at Low Temperatures. J Electrochem Soc 1988, 135:2651-2652.

[20] Uribe FA, Valerio JA, Garzon FH, Zawodzinski TA. PEMFC Reconfigured Anodes for Enhancing CO Tolerance with Air Bleed. Electrochem and Solid-State Lett 2004, 7:A376-A379.

[21] Hashimasa Y, Matsuda Y, Akai M. Effects of Platinum Loading on PEFC Power Generation Performance Deterioration by Carbon Monoxide in Hydrogen Fuel. ECS Transactions 2010, 26:131-142.

[22] Knights S, Bashyam R, He P, Lauritzen M, Startek C, Colbow V, Cheng T, Kolodziej J, Wessel S. PEMFC MEA and System Design Considerations. ECS Transactions 2011, 41:39-53.

[23] Bashyam R, He P, Wessel S, Knights S. Impacts of Cathode Loading on Ru Crossover Related PEFC Durability. ECS Transactions 2011, 41:837-844.

[24] Inaba M, Sugishita M, Wada J, Matsuzawa K, Yamada H, Tasaka A. Impacts of air bleeding on membrane degradation in polymer electrolyte fuel cells. J Power Sources 2008, 178:699-705.

[25] Wang W. The effect of internal air bleed on CO poisoning in a proton exchange membrane fuel cell. J Power Sources 2009, 191:400-406.

[26] Gubler L, Scherer GG, Wokaun A. Effects of cell and electrode design on the CO tolerance of polymer electrolyte fuel cells. Phys Chem Chem Phys 2001, 3:325-329.

[27] Murthy M, Esayian M, Lee W-k, Van Zee JW. The Effect of Temperature and Pressure on the Performance of a PEMFC Exposed to Transient CO Concentrations. J Electrochem Soc 2003, 150:A29-A34.

[28] Chu H-S, Tsau F, Yan Y-Y, Hsueh K-L, Chen F-L. The development of a small PEMFC combined heat and power system. J Power Sources 2008, 176:499-514.

[29] Yim S-D, Sohn Y-J, Yoon Y-G, Um S, Kim C-S, Lee W-Y. Operating characteristics of 40W-class PEMFC stacks using reformed gas under low humidifying conditions. J Power Sources 2008, 178:711-715.

[30] Chung C-C, Chen C-H, Weng D-Z. Development of an air bleeding technique and specific duration to improve the CO tolerance of proton-exchange membrane fuel cells. Appl Therm Eng 2009, 29:2518-2526.

[31] Hedström L, Tingelöf T, Alvfors P, Lindbergh G. Experimental results from a 5 kW PEM fuel cell stack operated on simulated reformate from highly diluted

hydrocarbon fuels: Efficiency, dilution, fuel utilisation, CO poisoning and design criteria. Int J Hydrogen Energy 2009, 34:1508-1514.

[32] Sung L-Y, Hwang B-J, Hsueh K-L, Tsau F-H. Effects of anode air bleeding on the performance of CO-poisoned proton-exchange membrane fuel cells. J Power Sources 2010, 195:1630-1639.

[33] Scholta J, Pawlik J, Chmielewski N, Jörissen L. Longevity test results for reformate polymer electrolyte membrane fuel cell stacks. J Power Sources 2011, 196:5264-5271.

[34] Antolini E. The problem of Ru dissolution from Pt–Ru catalysts during fuel cell operation: analysis and solutions. J Solid State Electrochem 2011, 15:455-472.

[35] Pérez LC, Brandão L, Sousa JM, Mendes A. Segmented polymer electrolyte membrane fuel cells - A review. Renew Sust Energ Rev 2011, 15:169-185.

[36] Auvinen S, Tingelöf T, Ihonen JK, Siivinen J, Johansson M. Stainless Steel In-situ Corrosion Testing in a PEFC Multisinglecell. ECS Transactions 2009, 25:1811-1821.

[37] Auvinen S, Tingelof T, Ihonen JK, Siivinen J. Cost Effective In-Situ Characterization of Coatings for PEFC Bipolar Plates Demonstrated with PVD Deposited CrN. J Electrochem Soc 2011, 158:B550-B556.

[38] Stumper J, Campbell SA, Wilkinson DP, Johnson MC, Davis M. In-situ methods for the determination of current distributions in PEM fuel cells. Electrochim Acta 1998, 43:3773-3783.

[39] Weng FB, Jou BS, Li CW, Su A, Chan SH. The effect of low humidity on the uniformity and stability of segmented PEM fuel cells. J Power Sources 2008, 181:251-258.

[40] Bender G, Angelo M, Bethune K, Dorn S, Thampan T, Rocheleau R. Method using gas chromatography to determine the molar flow balance for proton exchange membrane fuel cells exposed to impurities. J Power Sources 2009, 193:713-722.

[41] Richardson JF, Harker JH, Backhurst JR. Chemical Engineering Vol. 2. 5th ed. Oxford: Butterworth-Heinemann; 2002.

[42] Chatenet M, Dubau L, Job N, Maillard F. The (electro)catalyst|membrane interface in the Proton Exchange Membrane Fuel Cell: Similarities and differences with non-electrochemical Catalytic Membrane Reactors. Catal Today 2010, 156:76-86.

[43] Scholten JJF. The use of adsorption methods for the assessment of the surface area and pore size distribution of heterogeneous catalysts. In: Studies in Surface Science and Catalysis. Moulijn JA, van Leeuwen PWNM, van Santen RA, editors. Amsterdam: Elsevier Ltd; 1993, p. 419-438.

[44] Shioyama H. Carbon Materials used for Polymer Electrolyte Fuel Cells. In: Handbook of Advanced Ceramics. Shigeyuki S, editor. Oxford: Academic Press; 2013, p. 199-210.

[45] Emmett PH, Brunauer S. The Use of Low Temperature van der Waals Adsorption Isotherms in Determining the Surface Area of Iron Synthetic Ammonia Catalysts. J Am Chem Soc 1937, 59:1553-1564.

[46] Bashyam R, Zelenay P. A class of non-precious metal composite catalysts for fuel cells. Nature 2006, 443:63-66.

[47] Shanahan PV, Xu L, Liang C, Waje M, Dai S, Yan YS. Graphitic mesoporous carbon as a durable fuel cell catalyst support. J Power Sources 2008, 185:423-427.

[48] Angelo M, St-Pierre J, Bethune K, Rocheleau R. Gas Chromatography Study of Reactions of Carbon Monoxide at Different Operating Temperatures within a PEMFC. ECS Transactions 2011, 35:167-178.

# Chapter V

# Chapter V - CO poisoning studies[4]

## 5.1. Abstract

In this work, the effect of fuel utilization on the carbon monoxide (CO) poisoning dynamics is studied under expected future Polymer Electrolyte Membrane Fuel Cell (PEMFC) automotive conditions. Three fuel utilizations, 70%, 40% and 25%, are used. The CO is fed in a constant concentration mode of 1 ppm and in a constant molar flow rate mode (CO concentrations between 0.18-0.57 ppm). The anode exhaust gas composition is analyzed using a gas chromatograph. The results indicate that the CO poisoning dynamics is strongly dependent on the fuel utilization for both CO feed modes. When the fuel utilization is decreased, the molar flow rate of CO at the anode outlet is increased, leading to a slower decrease in performance of the cell. The decrease in performance of the fuel cell becomes even slower when the CO molar flow rate is reduced. The results suggest that the effect of impurities in PEMFC systems with fuel recirculation is determined by the dynamics of their enrichment in the anode loop, so the accurate quantification of impurities limits in current regulation (ISO 14687-2:2012) should be determined using this type of fuel delivery configuration.

[4] The content of this chapter is adapted from: Luis C. Pérez, Pauli Koski, Jari Ihonen, Pauli Koski, José M. Sousa, Adélio Mendes, 2013. Effect of fuel utilization on the carbon monoxide poisoning dynamics of PEMFC. Submitted to the Journal of Power Sources.

## 5.2. Introduction

The heavy reliance on fossil fuels and increasing environmental concerns have raised interest in Polymer Electrolyte Membrane Fuel Cells (PEMFC) for automotive applications [1]. The main technical problems of PEMFC have been solved [2]; however, there is room to reduce costs and improve their durability [3, 4]. One still sensible issue is related to the presence of impurities in the fuel and/or the oxidant since they affect the performance and accelerate the degradation of PEMFC [5].

The composition of the fuel used in PEMFC is regulated according to its final application. Current $H_2$ fuel specifications for road vehicles, ISO 14687-2:2012 and SAE J2719, limit the amount of impurities such as carbon monoxide (CO) to 0.2 ppm and sulphur species, hydrogen sulphide ($H_2S$) and sulphur dioxide ($SO_2$), to 4 ppb. Comply with these specifications hinders the market growth of PEMFC vehicles due to increased cost of the fuel. This is especially true for the $H_2$ produced via methane steam reforming (MSR) [6] and purified using pressure swing adsorption (PSA) [7] as it contains trace amounts of CO. This latter process of production and purification is considered the lowest cost option for $H_2$ production if reasonably priced methane is available.The increase in cost due to the use of PSA comes from the fact that, the lower the level of impurities required, the lower the $H_2$ yield of the PSA system. This is well illustrated in a paper by Besancon *et al.* [8].

CO is considered the most challenging impurity since it is difficult to separate and to measure in a cost effective way at a concentration of 0.2 ppm. CO affects the performance of PEMFC as it preferentially adsorbs onto the anode catalyst, hindering the hydrogen oxidation reaction (HOR) [5]. This problem becomes critical when the catalyst (platinum – Pt) loading is reduced. As shown by Gasteiger *et al.* [9], only 0.05 mg $Pt{\cdot}cm^{-2}$ or less would be needed for the anode in the absence of impurities. Despite that, current membrane electrode assemblies (MEAs) of automotive PEMFC systems have much higher Pt loadings [10]. Hashimasa *et al.* have shown that for both CO [11] and $H_2S$ [12], the Pt loading has a dramatic influence on the catalyst poisoning dynamics. Nevertheless, many of the most relevant studies in the literature

[13-16] have been performed using high catalyst loadings (0.3-0.4 mg Pt·cm$^{-2}$). Therefore, the effect of impurities at low loadings (< 0.1 mg Pt·cm$^{-2}$) is still poorly understood for almost all impurities.

The effect of fuel utilization ($\mu_f$) on the CO poisoning dynamics of the anode catalyst has been poorly studied too. In the majority of studies the fuel utilization is normally set to high values ($\mu_f$ = 50-85%), not corresponding to actual automotive PEMFC systems [17-20] for which the fuel is delivered in dead end mode with recirculation (Figure 5.1). These systems may require fuel utilizations of 20% since recirculation is used to humidify the $H_2$ [21]. Only in the study of Matsuda *et al.* [14] the fuel utilization was set to $\mu_f$ = 25%, representing actual automotive PEMFC conditions.

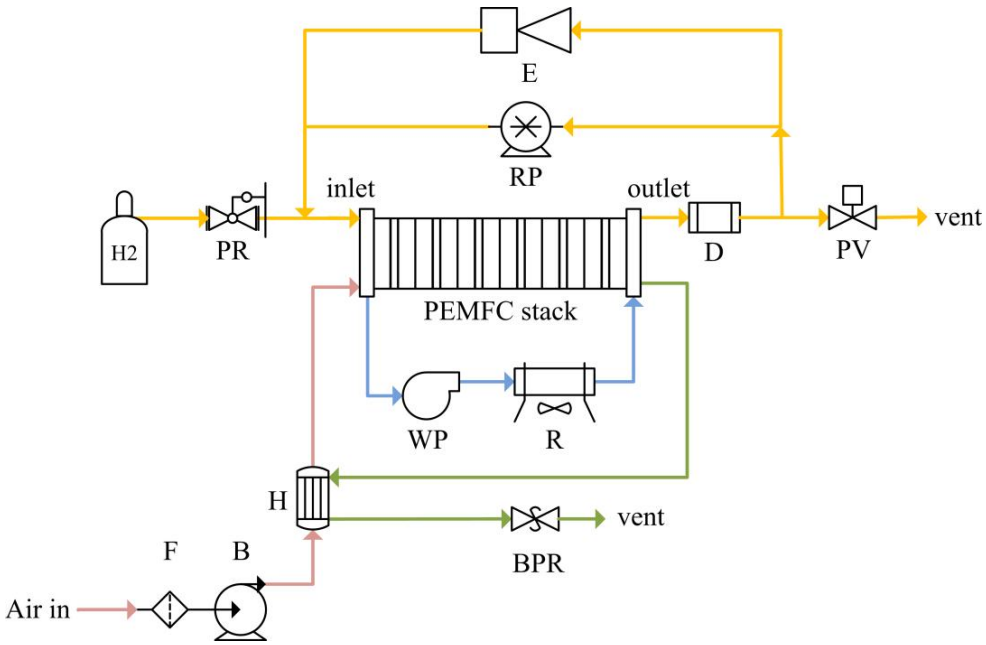


Figure 5.1. Simplified diagram of an automotive PEMFC system. PR, pressure regulator; D, demister; PV, purge valve; RP, recirculation pump; E, ejector; F, filter; B, blower; H, humidifier; WP, water pump; R, radiator; BPR, back pressure regulator. Adapted from [17-20].

In Chapter 3 [22] it was shown that the fuel utilization influences the anode catalyst poisoning dynamics when the CO concentration ($C_{CO}$), the anode catalyst loading and the fuel utilization were high, 15-19 ppm, 0.4 mg Pt·cm$^{-2}$ and 55-83% respectively. These authors also observed that under CO poisoning, the anode behaves similarly to a fixed-bed adsorption column (CO filter). In this analogy, the CO removal efficiency

from the $H_2$ stream depends on the catalyst loading (filter capacity) and the fuel utilization (residence time), which ultimately determine the CO breakthrough within the cell. In that study no significant amount of CO was detected in the anode exhaust gas before a significant drop in the current of the cell was observed due to the CO concentration and Pt loading. In contrast, in the studies by Hashimasa *et al.* [11] (1 ppm of CO and 70% fuel utilization) and by Santis [23] (50 ppm of CO and 50% fuel utilization), CO was detected for a marginal drop in performance during galvanostatic [11] and potentiostatic [23] operation. The study by Hashimasa indicates that less CO may breakthrough the cell for similar potential drops when the Pt loading is higher.

It is noteworthy that the fuel delivery configuration depicted in Figure 5.1 makes necessary to study the dynamic "enrichment" or "buildup" of impurities [24, 25] in the recirculation loop. One possibility to gain insight on the buildup of impurities is to analyze the anode exhaust gas composition in PEMFC without recirculation (single pass of fuel and venting). The latter has been applied in a few studies in the literature [11, 15, 23, 26], but again, in these studies the anode catalyst loading and/or the fuel utilization were too high. To the knowledge of the authors, only Matsuda *et al.*[14] have experimentally studied the buildup of impurities in the recirculation loop. However, in their work the anode catalyst loading was high and the CO concentration one order of magnitude higher than specified in current regulation.

The effect of fuel utilization on CO poisoning has been studied numerically [27-29]; however, no systematic experimental effort has been made to estimate the effect of impurity buildup with relevant CO concentrations and anode catalyst loadings. Ahluwalia and Wang [25] have modeled the buildup of CO and $CO_2$ in the recirculation loop and used this data to determine the optimum fuel quality for PEMFCs with low Pt loading. Those authors also observed that there could be significant buildup of CO in the recirculation loop.

The literature cited above indicates that the CO breakthrough is dependent on the fuel utilization and the Pt loading. Information about the CO breakthrough and buildup in the recirculation loop is of crucial importance to optimize the fuel quality

of PEMFC vehicles. However, for this purpose there are no experimental results in the literature with enough relevance.

In this paper, the influence of fuel utilization on the CO poisoning dynamics is studied in experimental conditions that are relevant for PEMFC vehicles. Three fuel utilizations 70%, 40%, 25% are experimented. The CO is fed in a constant concentration mode of 1 ppm and in a constant molar flow rate mode (CO concentrations between 0.18-0.57 ppm). A single cell with an anode catalyst loading of 0.05 mg Pt $cm^{-2}$ is operated in galvanostatic mode at 1 $A \cdot cm^{-2}$ and 80 °C. Furthermore, the drop in performance of the cell is tracked while the CO concentration at the anode outlet is continuously measured using a gas chromatograph (GC).

## 5.3. Experimental

### 5.3.1. Set-up description

The experiments were performed in a fuel cell test station (G60 series, Greenlight Innovation, Canada). The capabilities of the station include automated control and measurement of gases flow rates, temperatures, dew points, pressures and electrochemical characterization of the cell. Figure 5.2 shows a schematic of the experimental set-up. The single cell (Fuel Cell Technologies Inc., USA) comprised a MEA (H series, Solvicore, Germany) with 25 $cm^2$ active area loaded with 0.05 mg $Pt \cdot cm^{-2}$ on the anode and with 0.4 mg $Pt \cdot cm^{-2}$ on the cathode. The gas diffusion layers (Sigracet® SGL 24 BC, SGL technologies, Germany) were 235 μm thick. Teflon® gaskets with 150 μm thickness were used. The clamping pressure was regulated using disc springs (Belleville, UK). The bipolar plates were manufactured from graphite blocks (ISEM-3, Svenska Tanso, Sweden) with 88 mm length x 88 mm width x 20 mm thick. Single channel serpentine flow fields were machined on both bipolar plates. The geometry of the gas channel was 1 mm width x 1.5 mm depth while the rib was 1 mm width. Gases were fed in counter-flow.

The anode was fed with $H_2$ (99.999% pure, amount of impurities: $H_2O \leq 3$ ppm $O_2 \leq 2$ ppm $C_nH_m \leq 0.5$ ppm and $N_2 \leq 5$ ppm) at three fuel utilizations, $\mu_f = 70\%$, 40% and 25%. The anode relative humidity ($RH_{ano}$) was set to 50% and the anode pressure ($P_{ano}$) was atmospheric. The CO was obtained from a 150 bar gas bottle (AGA OY, Finland) with a nominal $C_{CO}$ of 90.9 ppm balanced with $N_2$.

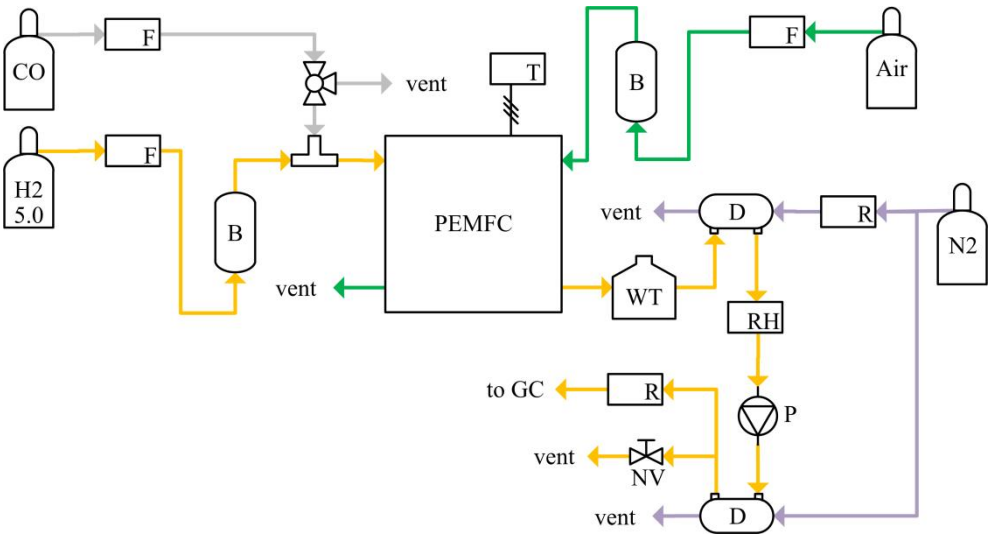


Figure 5.2. Schematic of the experimental set-up. F, mass flow controller; B: bubbler, T: thermocouple, WT: water trap, D, dryer; R, rotameter; RH, relative humidity probe; P, diaphragm pump and NV, needle valve.

The anode exhaust gas was passed through a water trap and the still warm gas was further dried using a selective membrane module (FC™- Series, Perma Pure LLC, USA). To remove the remaining water, nitrogen ($N_2$) was fed to the permeate side of the membrane module in counter current at a volumetric flow rate of $Q_{N2} = 1$ dm$^3$·min$^{-1}$ using a rotameter (UK-040 series, Honsberg, Germany). A micro diaphragm sample pump (NMS 020 B, KNF, Germany) was used to minimize the delay between the anode exit and the GC injection port. A second membrane drier (FC™- Series, Permapure LLC, USA) was placed after the pump to further dry the sample. A needle valve (Series AS, SMC, Japan) was used to control the amount of gas sent to the GC. A rotameter (FLD series, Omega, USA) measured the flow rate of the sample entering the GC. This conditioning configuration of the anode exhaust was implemented since it ensures minimal dissolution of CO and $CO_2$ into condensed water. The relative

humidity and temperature of the sample was measured after the first membrane drier with a probe model HMP110 (Vaisala, Finland).

The cathode was fed with humidified synthetic air. The oxidant utilization ($\mu_{ox}$) was 40% in all the experiments. The cathode relative humidity ($RH_{cat}$) was set to 50% and the cathode pressure ($P_{cat}$) was atmospheric. The cell temperature ($T_{cell}$) was 80 °C.

5.3.2. Gas chromatograph description

The gas chromatograph (model 6890N, Agilent Technologies, USA) was equipped with a flame ionization detector (FID) for CO and $CO_2$ detection. The equipment was calibrated daily using a gas mixture obtained from a 150 bar gas bottle (AGA OY, Finland) with a nominal $C_{CO}$ of 10.2 ppm and a nominal $CO_2$ concentration ($C_{CO2}$) of 9.63 ppm balanced with He. It was programmed to take a gas sample, plot the corresponding chromatogram and record it in a file. This process took ca. four minutes so 16 gas samples were automatically taken every hour.

Two actions, one concerning the GC hardware and the other the GC software, were taken to improve the accuracy of the measurements. In the beginning, a single column GC configuration was used; nonetheless, disturbances attributed to a marginal contamination of the sample ($N_2$ or $H_2O$) made it very hard to find a clear point to start integrating the CO peak. This was solved using a two column GC configuration, one for detecting the CO and one for detecting the $CO_2$. The other action was related to the GC signal processing. Even the small inherent fluctuation of the GC baseline may introduce noise to the measurements due to automatic selection of the points to start and finish integrating the CO peak. The GC software was not sensible enough, so an integration routine for the GC signals was developed using Matlab®. Linear least squares fitting was used to minimize the inherent fluctuation of the baseline and integration was done with trapezoid algorithm after careful selection of the CO integration limits.

The molar flow rate of CO, $\dot{n}_{CO,out}$ (mol $s^{-1}$), was calculated using Equation 1. The volumetric flow rate of the gas mixture leaving the cell (dry basis), $Q_{out}$ ($cm^3$ $s^{-1}$), was

calculated based on the input flow rate assuming 100% of coulombic efficiency of the cell, according to Equations 2-5 as follows:

$$\dot{n}_{CO,out} = \frac{Q_{out} \times C_{\mathrm{CO},out} \times P}{RT} \quad (1)$$

$$Q_{out} = Q_{H2} - Q_{H2,cons} \quad (2)$$

$$Q_{H2} = \dot{n}_{H2}\, R\, \frac{T}{P}\, \frac{1}{\mu_f} \quad (3)$$

$$\dot{n}_{H2} = \frac{I_{tot}}{2F} \quad (4)$$

$$Q_{H2,cons} = \frac{I_{tot} RT}{2FP} \quad (5)$$

where, $C_{\mathrm{CO},out}$ (ppm) is the CO concentration, $P$ (Pa) is the pressure, $R$ is the gas constant, 8.314 J mol$^{-1}$ K$^{-1}$, $T$ (K) is the temperature, $Q_{H2}$ (cm$^3$ s$^{-1}$) is the volumetric flow rate of hydrogen fed to the anode, $Q_{H2,cons}$ (cm$^3$ s$^{-1}$) is the hydrogen consumed, $\dot{n}_{H2}$ (mol s$^{-1}$) is the molar flow rate of hydrogen fed to the anode, $I_{tot}$ (A) is the total current of the cell and $F$ is the Faraday constant, 96485.34 C mol$^{-1}$.

### 5.3.3. Test procedure

Table 13 summarizes the experiments performed. Different CO feed regimes were used. In Experiments #1 to #3 a constant $C_{CO}$ of 1 ppm was used. During Experiments #4, #5 and #6 the molar flow rate of CO ($\dot{n}_{CO}$) was 1.87x10$^{-10}$ mol·s$^{-1}$. For Experiments #7, #8 and #9 the impurity flow rate was 0.93·10$^{-10}$ mol·s$^{-1}$. The experiments were repeated at least four times and their reproducibility assessed. The cell was activated using an in-house developed potentiostatic cycling protocol.

Every experiment started with a stabilization period of at least 1 h during which the cell was operated with the conditions of interest but without feeding CO. After this, CO was fed until a potential drop of 50 mV was reached and then stopped. Finally, a catalyst surface “clean-up” procedure was implemented. The procedure included three steps: i) substitution of $H_2$ by $N_2$ with galvanostatic operation of the cell at

$I_{tot}$ = 1.5 A until $E_{cell}$ = 0.6 V, ii) potentiostatic operation of the cell at $E_{cell}$ = 0.6 V until $I_{tot}$ = 0.150 A and iii) potentiostatic operation of the cell at $E_{cell}$ = 0.1 V until $I_{tot}$ = 0 A. The intention of the "clean-up" routine was to remove the entire CO from the catalyst surface and start every experiment from the same original potential.

Table 13 - Summary of experimental conditions. Note: n.a. states for no applicable.

| Exp. # | $T_{cell}$ (°C) | $\mu_f$ (%) | $C_{CO}$ (ppm) | $\dot{n}_{CO}$ (x $10^{-10}$ mol $s^{-1}$) | $\mu_{ox}$ (%) | $RH_{ano} = RH_{cat}$ (%) | $P_{ano} = P_{cat}$ (MPa) |
|---|---|---|---|---|---|---|---|
| 1 | 80 | 70 | 1 | 1.87 | 40 | 50 | ≈ 0.101 |
| 2 | | 40 | | 3.27 | | | |
| 3 | | 25 | | 5.24 | | | |
| 4 | | 70 | 0.57 | 1.87 | | | |
| 5 | | 40 | | | | | |
| 6 | | 25 | 0.36 | | | | |
| 7 | | 70 | 0.50 | 0.93 | | | |
| 8 | | 40 | 0.28 | | | | |
| 9 | | 25 | 0.18 | | | | |

## 5.4. Results and discussion

The sources of error and other factors affecting the CO and $CO_2$ concentration measurements during CO poisoning of PEMFC have been properly identified previously [15, 22]. Here, those sources of error were taken into account and the $H_2$ from the gas bottle was analyzed for several hours with the GC. It was concluded that it contained approx. 35 ppb of CO, so that value was subtracted from the CO concentrations presented below.

Figure 5.3. Performance of the fuel cell for $\mu_f$ = 70% and 1 ppm feed CO (Experiment #1): a) potential drop history, b) CO concentration at the anode outlet as a function of time and c) estimated molar flow rate of CO at the anode outlet as a function of time. The CO is injected at $t$ = 0 min. Other experimental conditions as in Table 13.

Before evaluating the effect of fuel utilization at CO concentrations below 1 ppm, it was necessary to assess the reproducibility of the tests. The latter is highlighted in Figure 5.3 for Experiment #1 with three repetitions, all performed consecutively. The reproducibility was evaluated from two perspectives: i) the potential drop curves (Figure 5.3a), which is related to the time needed to reach the 50 mV potential drop and ii) the anode exhaust gas composition analysis, which is related to the CO concentration (Figure 5.3b) and the CO molar flow rate (Figure 5.3c) at the anode outlet. It is observed that the results depicted in Figure 5.3 are reproducible and consistent. The same reproducibility and consistency was observed for the rest of the experiments.

One key issue for achieving the excellent reproducibility and consistency of the results shown in Figure 5.3 was the clean-up procedure. The procedure intended to promote the electrooxidation of CO [30] and thus liberate the anode catalytic sites covered by CO. It was noticed a positive effect of the procedure on the reproducibility of the results until the effect of catalyst aging was noticed (last set of experiments).

### 5.4.1. Effect of fuel utilization for a constant CO feed concentration of 1 ppm

Figure 5.4 shows the potential drop, CO concentrations and CO molar flow rates at the anode outlet for a constant 1 ppm feed CO concentration. A single test with no repetitions was plotted for each experiment. Figure 5.4a shows that it took approximately 10 min more for the lowest fuel utilization to reach a potential drop of 50 mV, despite the molar flow rate of CO was ≈ 2.8 times higher when compared to the highest fuel utilization (Table 13). The potential drop was attributed to the adsorption of CO onto the anode catalytic sites; however, the results of Figure 5.4a seem to be counterintuitive once it would be expected a faster drop in performance for a CO molar feed almost 3 times higher.

Figure 5.4b shows that the CO concentration at the outlet exceeded 1 ppm for the 70% fuel utilization after 27.5 min but was not exceeded for 40% and 25% fuel utilizations. The CO concentration decreases along the flow field channels if the CO is oxidized by the $O_2$ permeating from the cathode due to the internal air bleed [31]. However, not all the CO is oxidized by the internal air bleed nor is adsorbed onto de catalyst, so the CO concentration increases towards the anode outlet as a function of the consumed of $H_2$ along the flow field channels. In fact, it is expected that the CO concentration increases until the anode overpotential reaches a steady-state [11, 15, 16]. From a practical point of view, it is important to measure the CO concentration at the anode outlet but only if the molar flow rate of CO at the anode outlet is estimated afterwards. Figure 5.4b suggests that CO may start being recirculated in the anode loop before the CO concentration at the anode inlet is overpassed.

Figure 5.4. Performance of the fuel cell for $\mu_f$ = 70% (Experiment #1), $\mu_f$ = 40% (#2) and $\mu_f$ = 25% (#3) and 1 ppm feed CO: a) potential drop history, b) CO concentration at the anode outlet as a function of time and c) estimated molar flow rate of CO at the anode outlet as a function of time. The Y axis on the right of Figure 5.4c is the corresponding molar flow rate of CO at the anode inlet. The CO is injected at $t$ = 0 min. Other experimental conditions as in Table 13.

Figure 5.4c shows that the lowest the fuel utilization, the highest the molar flow rate of CO at the outlet. The molar flow rates of CO at the anode inlet are highlighted on the right Y axis of the same figure. It is observed that the ratio between the molar flow rate of CO at the anode outlet and inlet increases more steeply in the beginning at lower fuel utilizations. By the end of the experiments the ratios between the outlet and inlet were 64% for $\mu_f$ = 25%, 49% for $\mu_f$ = 40% and 48% for $\mu_f$ = 70%. The ratios between the outlet and inlet and the results of Figure 5.4c suggest that proportionally more CO leaves the cell without being adsorbed or reacting into a different compound at the lowest fuel utilization, which alleviates partially the effect of CO, but not fully explains why it took more time to reach the 50 mV potential drop at the lowest fuel utilization.

From Figure 5.4, it can be concluded that the internal air bleed should be somehow more effective at lower fuel utilizations since the total amount of CO molar feed to the cell for the same period of time was the highest during Experiment #3 and the electrooxidation of CO is not favored for the low anode overpotentials expected under the conditions of the tests [30].

For Experiments #1, #2 and #3, the total amount of CO fed to the cell was different for similar periods of time. Below, it is discussed a case for which the total amount of CO fed is different for similar periods of time.

### 5.4.2. Effect of fuel utilization for a low constant CO molar flow rate

In a PEMFC system with fuel recirculation it is expected that the $H_2$ tank contains a certified CO concentration. If the system is operated in galvanostatic regime, the $H_2$ coming from the tank is only the necessary to meet the demanded current and the recirculation pump increases the $H_2$ flow rate in the anode loop, decreasing proportionally the fuel utilization [25, 32]. Then, for transient current demand periods, the CO molar flow rate coming from the $H_2$ tank is variable (Section 3.1); on the other hand, during steady state current periods the CO molar flow rate supplied by the $H_2$ tank is constant (Sections 3.2 and 3.3).

Figure 5.5 shows the potential drop, CO concentrations and CO molar flow rates at the anode outlet for a constant CO molar flow rate of $1.87 \times 10^{-10}$ mol·s$^{-1}$ at the inlet. It can be observed that at lower fuel utilizations more time is needed to reach the 50 mV potential potential drop (Figure 5.5a). Furthermore, the time needed to reach the 50 mV potential potential drop is five times higher for the lowest fuel utilization compared with the highest fuel utilization. The results in Figure 5.4a and Figure 5.5a demonstrate that the fuel utilization influences the CO poisoning dynamics for both a constant CO concentration and a constant CO molar flow feed.

Figure 5.5c shows that the CO breakthrough is faster in time and higher in magnitude for the lowest utilization. Interestingly, at the end of every experiment the ratio between the molar flow rate of CO at the anode outlet and inlet was ≈ 50% for the

three fuel utilizations, thus proving that at higher fuel utilizations, the total amount of CO needed to cause a potential drop of 50 mV in the cell is lower.

The reason why the potential drop is slower at a lower fuel utilization for a constant molar flow rate of CO can be attributed to three factors: i) the total amount of CO adsorbed onto the anode catalytic sites is lower for similar periods of time (as suggested by Figure 5.5c) and, since the catalytic area reduction is smaller, the resulting overpotential is smaller and ii) the CO that adsorbs onto the anode catalytic sites is more evenly distributed within the cell and thus the internal air bleed is somehow more effective.

Figure 5.5. Performance of the fuel cell for $\mu_f$ = 70% (Experiments #1), $\mu_f$ = 40% (#2) and $\mu_f$ = 25% (#3) and molar flow rate of CO at inlet of $1.87 \times 10^{-10}$ mol·s$^{-1}$: a) potential drop history, b) CO concentration at the anode outlet as a function of time; and c) estimated molar flow rate of CO at the anode outlet as a function of time, for Experiments #4, #5 and #6. The CO is injected at $t$ = 0 min. Other experimental conditions as in Table 13.

It is noteworthy the effort made by other authors to study distribution of CO within the cell both experimentally [33, 34] and numerically [28, 29]. The numeric study by Bonnet *et al.* [29] shows that at 25% fuel utilization the gas composition, the fraction of catalytic sites covered by CO, the anode overpotential and the current density distribution is quite even between the anode inlet and outlet. The model by Brett *et al* [28] also predicts that the fraction of catalytic sites between the inlet and outlet is more even at higher flow rates. Nonetheless, the results by Bonnet *et al.* for higher fuel utilizations are not in accordance with the experimental results by Tingelöf *et al.* [33] and Reshetenko *et al*. [34] which observed a lower current density close to the anode inlet using a segmented PEMFC. More experimental work is needed in order to analyze the effect of fuel utilization on the distribution of CO within the cell. However, the results presented here support the hypothesis that the factor dominating the distribution of CO within the cell is the mean gas velocity at the anode inlet, as resulting from the simulation results by Brett *et al.* [28].

### 5.4.3. Effect of fuel utilization for a ultra-low constant CO molar flow rate

Figure 5.6 shows the potential drop, CO concentrations and CO molar flow rates at the anode outlet for a constant CO molar flow rate of $0.93 \times 10^{-10}$ mol·s$^{-1}$ at the anode inlet. The CO molar flow rate is halved compared with results of section 3.2 (CO molar flow rate of $1.87 \times 10^{-10}$ mol·s$^{-1}$) and the time needed to reach the 50 mV potential drop is 2 - 2.3 times higher for the corresponding fuel utilizations. It is observed that the time needed to reach the 50 mV potential drop is seven times higher for the lowest fuel utilization compared with the highest fuel utilization (Figure 5.6a).

Figure 5.6a shows that in Experiment #8 ($\mu_f$ = 40%) the onset potential started approx. 20 mV lower than for the other two Experiments (#7 and #9). This experiment (which comprises at least three repetitions) was the last to be performed and this difference might highlight the aging of the anode catalyst. It has been reported a loss of electrochemically active area at the anode after consecutive CO poisoning-recovery cycles [35]. Here, aging of the anode catalyst might have been accelerated as a consequence of the clean-up procedure.

Figure 5.6. Performance of the fuel cell for $\mu f$ = 70% (Experiments #1), $\mu f$ = 40% (#2) and $\mu f$ = 25% (#3) and molar flow rate of CO at inlet of $0.93 \times 10^{-10}$ mol·s-1: a) potential drop history; b) CO concentration at the anode inlet as a function of time; and c) estimated molar flow rate of CO at the anode outlet as a function of time. CO is injected at t = 0 min. Other experimental conditions as in Table 13.

Figure 5.6b and 5.6c show how it becomes difficult to accurately measure the CO concentration and determine the molar flow rate of CO at the anode outlet for Experiments #8 and #9. In these experiments the CO concentration at the inlet was 0.28 ppm and 0.18 ppm respectively. The fluctuations observed were attributed to current configuration of the GC, which was not optimized for these low concentrations. Despite the noise, the results of Figures 5.6b and 5.6c are in accordance with those observed in the previous Section (Figures 5.5b and 5.5c). It is believed that this type of set-up achieves a CO resolution of 30–50 ppb.

The test with 25 % fuel utilization depicted in Figure 5.6 meet the current $H_2$ fuel specifications for road vehicles (ISO 14687-2:2012) concerning the CO concentration (limit of 0.2 ppm). It took approximately 5.5 h to reach the 50 mV potential drop for

this case. The conditions of the test, particularly the constant current density of 1 A $cm^2$ and the 5.5 h length, will not correspond to the conditions demanded from a PEMFC automotive system. This suggests that the CO concentration limit of the current H2 fuel regulation may be inherently safe for PEMFC vehicles but strongly remarks the importance of systematically studying the effect of CO buildup in anode loop and evaluate its possible implications on the regulation. This kind of evaluation may ultimately lead to develop principles of safety engineering [36] aiming to reduce the risk and uncertainty associated to the presence of impurities present in the $H_2$ fuel.

## 5.5. Conclusions

The CO poisoning dynamics of the anode catalyst was studied for CO concentrations between 0.18-1 ppm and three fuel utilizations in a single cell. CO was fed to the cell in a constant concentration and a constant molar flow rate mode.

It was observed a gradual decrease in performance when the CO was fed to the cell that was attributed to the adsorption of CO onto de anode catalytic sites. It was demonstrated that the fuel utilization strongly influences the CO poisoning dynamics in PEMFC independently of the CO feed mode used. For lower fuel utilizations the decrease in performance of the cell was slower. The decrease in performance was even slower when the molar flow rate of CO was reduced.

The anode exhaust gas composition was measured during the tests and the CO molar flow rate at the anode outlet was estimated accordingly. It was found that at lower fuel utilizations, the CO breakthrough was faster and higher in magnitude, partially mitigating the effect of CO. Besides that, it was proposed that the increased tolerance to CO at lower fuel utilizations should be related to: i) a smaller anode overpotential, which is a consequence of a lower amount of CO that adsorbed onto the anode catalytic sites for similar periods of time and ii) a more even distribution of CO within the cell, which in turn makes more effective the internal air bleed.

These results indicate that dynamics of impurity enrichment in PEMFC systems with fuel recirculation will determine the effect of impurities at lower concentration levels. This means that accurate determination of impurity limits for ISO 14687-2:2012 standard requires that PEMFC catalyst poisoning measurements should be studied using fuel recirculation systems.

## 5.6. Acknowledgements

This research has been conducted under the "Fuel Cell 2007-2013" technology program of Tekes, the Finnish Funding Agency for Technology and Innovation.

L. C. Pérez is grateful to the National Foundation of Science and Technology of Portugal (FCT) for his PhD grant reference SFRH/BD/44684/2008. L. C. Pérez also acknowledges the support from the National Council of Science and Technology of Mexico (CONACyT).

## 5.7. References

[1] Mench, M. M., 2008, Fuel Cell Engines, John Wiley & Sons, Inc., New Jersey.

[2] Wang, Y., Chen, K. S., Mishler, J., Cho, S. C., and Adroher, X. C., 2011, "A review of polymer electrolyte membrane fuel cells: Technology, applications, and needs on fundamental research," Applied Energy, 88(4), pp. 981-1007.

[3] El-kharouf, A., Chandan, A., Hattenberger, M., and Pollet, B. G., 2012, "Proton exchange membrane fuel cell degradation and testing: review," Journal of the Energy Institute, 85(4), pp. 188-200.

[4] Miller, M., and Bazylak, A., 2011, "A review of polymer electrolyte membrane fuel cell stack testing," Journal of Power Sources, 196(2), pp. 601-613.

[5] Zamel, N., and Li, X., 2011, "Effect of contaminants on polymer electrolyte membrane fuel cells," Progress in Energy and Combustion Science, 37(3), pp. 292-329.

[6] Bhat, S. A., and Sadhukhan, J., 2009, "Process intensification aspects for steam methane reforming: An overview," AIChE Journal, 55(2), pp. 408-422.

[7] Adhikari, S., and Fernando, S., 2006, "Hydrogen Membrane Separation Techniques," Industrial & Engineering Chemistry Research, 45(3), pp. 875-881.

[8] Besancon, B. M., Hasanov, V., Imbault-Lastapis, R., Benesch, R., Barrio, M., and Mølnvik, M. J., 2009, "Hydrogen quality from decarbonized fossil fuels to fuel cells," International Journal of Hydrogen Energy, 34(5), p. 2350.

[9] Gasteiger, H. A., Panels, J. E., and Yan, S. G., 2004, "Dependence of PEM fuel cell performance on catalyst loading," Journal of Power Sources, 127(1-2), pp. 162-171.

[10] Debe, M. K., 2012, "Electrocatalyst approaches and challenges for automotive fuel cells," Nature, 486(7401), pp. 43-51.

[11] Hashimasa, Y., Matsuda, Y., and Akai, M., "Effects of platinum loading on PEFC power generation performance deterioration by carbon monoxide in hydrogen fuel," Proc. ECS Transactions, p. 131.

[12] Hashimasa, Y., Matsuda, Y., Imamura, D., and Akai, M., 2011, "PEFC power generation performance degradation by hydrogen sulfide and ammonia - Effects of lowering platinum loading," Electrochemistry, 79(5), p. 343.

[13] Imamura, D., Ebata, D., Hashimasa, Y., Akai, M., and Watanabe, S., 2007, "Impact of Hydrogen Fuel Impurities on PEMFC Performance," SAE Paper 2007-01-2010.

[14] Matsuda, Y., Hashimasa, Y., Imamura, D., Akai, M., and Watanabe, S., 2009, "Accumulation behavior of impurities in fuel cell hydrogen circulation system," Review of Automotive Engineering, 30(2), p. 167.

[15] Bender, G., Angelo, M., Bethune, K., Dorn, S., Thampan, T., and Rocheleau, R., 2009, "Method using gas chromatography to determine the molar flow balance for proton exchange membrane fuel cells exposed to impurities," Journal of Power Sources, 193(2), pp. 713-722.

[16] Bender, G., Angelo, M., Bethune, K., and Rocheleau, R., 2013, "Quantitative analysis of the performance impact of low-level carbon monoxide exposure in proton exchange membrane fuel cells," Journal of Power Sources, 228, p. 159.

[17] Wu, B., Matian, M., and Offer, G. J., 2012, "Hydrogen PEMFC system for automotive applications," International Journal of Low-Carbon Technologies, 7(1), pp. 28-37.

[18] Cordner, M., Matian, M., Offer, G. J., Hanten, T., Spofforth-Jones, E., Tippetts, S., Agrawal, A., Bannar-Martin, L., Harito, L., Johnson, A., Clague, R., Marquis, F., Heyes, A., Hardalupas, Y., and Brandon, N. P., 2010, "Designing, building, testing and racing a low-cost fuel cell range extender for a motorsport application," Journal of Power Sources, 195(23), pp. 7838-7848.

[19] Ahluwalia, R. K., and Wang, X., 2008, "Fuel cell systems for transportation: Status and trends," Journal of Power Sources, 177(1), pp. 167-176.

[20] Zhai, S., Sun, P., Chen, F., Zhou, S., and Zhang, C., 2010, "Collaborative simulation for dynamical PEMFC power systems," International Journal of Hydrogen Energy, 35(16), pp. 8772-8782.

[21] Ahluwalia, R. K., Wang, X., Kwon, J., Rousseau, A., Kalinoski, J., James, B., and Marcinkoski, J., 2011, "Performance and cost of automotive fuel cell systems with ultra-low platinum loadings," Journal of Power Sources, 196(10), pp. 4619-4630.

[22] Pérez, L. C., Rajala, T., Koski, P., Ihonen, J., Sousa, J., and Mendes, A., "Development of a methodology to optimize the air bleed in PEMFC systems operating with low quality hydrogen". International Journal of Hydrogen Energy, 38 (2013) 16286-16299.

[23] Alvarez, M. V. S., 2006, "Investigations of current density inhomogeneities in polymer electrolyte fuel cells,"PhD, ETH/PSI, Zürich.

[24] Karimäki, H., Pérez, L. C., Nikiforow, K., Keränen, T. M., Viitakangas, J., and Ihonen, J., "The use of on-line hydrogen sensor for studying inert gas effects and nitrogen crossover in PEMFC system," *International Journal of Hydrogen Energy* 2011, *36*, 10179-10187.

[25] Ahluwalia, R. K., and Wang, X., 2008, "Effect of CO and CO2 impurities on performance of direct hydrogen polymer-electrolyte fuel cells," Journal of Power Sources, 180(1), pp. 122-131.

[26] Angelo, M., St-Pierre, J., Bethune, K., and Rocheleau, R., 2011, "Gas Chromatography Study of Reactions of Carbon Monoxide at Different Operating Temperatures within a PEMFC," ECS Transactions, 35(32), pp. 167-178.

[27] Zhang, J. X., Thampan, T., and Datta, R., 2002, "Influence of anode flow rate and cathode oxygen pressure on CO poisoning of proton exchange membrane fuel cells," Journal of the Electrochemical Society, 149(6), pp. A765-A772.

[28] Brett, D. J. L., Aguiar, P., Brandon, N. P., and Kucernak, A. R., 2007, "Measurement and modelling of carbon monoxide poisoning distribution within a polymer electrolyte fuel cell," International Journal of Hydrogen Energy, 32(7), pp. 863-871.

[29] Bonnet, C., Franck-Lacaze, L., Ronasi, S., Besse, S., and Lapicque, F., 2010, "PEM fuel cell Pt anode inhibition by carbon monoxide: Non-uniform behaviour of the cell caused by the finite hydrogen excess," Chemical Engineering Science, 65(10), pp. 3050-3058.

[30] Iwasita, T., 2010, "Methanol and CO electrooxidation," Handbook of Fuel Cells, John Wiley & Sons, Ltd.

[31] Wang, W., 2009, "The effect of internal air bleed on CO poisoning in a proton exchange membrane fuel cell," Journal of Power Sources, 191(2), pp. 400-406.

[32] Pérez, L. C., Ihonen, J., Sousa, J. M., and Mendes, A., 2013, "Use of Segmented Cell Operated in Hydrogen Recirculation Mode to Detect Water Accumulation in PEMFC," Fuel Cells, Fuel Cells, 13(2), pp. 203-216.

[33] Tingelöf, T., Hedström, L., Holmström, N., Alvfors, P., and Lindbergh, G., 2008, "The influence of CO2, CO and air bleed on the current distribution of a polymer electrolyte fuel cell," International Journal of Hydrogen Energy, 33(8), pp. 2064-2072.

[34] Reshetenko, T. V., Bethune, K., and Rocheleau, R., 2012, "Spatial proton exchange membrane fuel cell performance under carbon monoxide poisoning at a low concentration using a segmented cell system," Journal of Power Sources, 218(0), pp. 412-423.

[35] Angelo, M., Bethune, K., and Rocheleau, R., 2010, "The Impact of sub ppm Carbon Monoxide and ppm Level CO/Toluene and Methylcyclohexane/CO Mixtures on PEMFC Performance and Durability," ECS Transactions, 28(23), pp. 169-181.

[36] Möller, N., and Hansson, S. O., 2008, "Principles of engineering safety: Risk and uncertainty reduction," Reliability Engineering & System Safety, 93(6), pp. 798-805.

# Chapter VI

# Chapter VI - Conclusions and future work

A literature review on segmented PEMFC (SFC) was performed. The approaches to design, construct and characterize the SFC were categorized in invasive and non-invasive. In turn, the main invasive approaches were divided in printed circuit board, resistors network, Hall effect sensors and resistors network. General guidelines for the design, construction and electrochemical characterization of SFC were provided. It was found that the current density distribution of PEMFC is inhomogeneous over the MEA active area as a consequence of the complex interaction of design features (i.e. flow field geometry), assembling characteristics (i.e. clamping pressure) and operating parameters (i.e. relative humidity, flow rate, pressure or fuel composition) as well as on the properties of the MEA and GDL. It was highlighted how the current density distribution measurements can be complemented with other analytical techniques that allow: i) $H_2$, $O_2$, $N_2$ and water vapor distribution determination, ii) liquid water distribution analysis, iii) temperature distribution measurements and iv) local high frequency resistance (HFR) and local electrochemical impedance spectroscopy (EIS) analysis.

A test bench was built around a SFC operated in hydrogen recirculation mode with continuous removal of water. The test bench capabilities include fundamental electrochemical analysis as well as current density distribution, water balance and nitrogen crossover measurements at the single cell level. The concept of partially segmented bipolar plates was introduced. The major advantage of the partially segmented bipolar plates is a decrease in the lateral current spreading while at the same time it avoids the total segmentation. In contrast, the major disadvantage is the decrease in mechanical strength of the bipolar plates. Representative anode operating conditions namely, recirculated gas flow rate, pressure and the time between purges, were varied to analyze their effect on the current density distribution of the SFC. Two different current density distribution diagram shapes were observed for the two different gas recirculation flow rates used. When the gas recirculation rate was low, the current density distribution reached a maximum value

upstream the flow field close that decreased downstream, indicating flooding conditions towards the outlet. When the gas recirculation rate was high, there was a decrease in performance upstream the flow field but homogeneous current density distribution afterwards, indicating drying conditions upstream. The anode pressure and time between purges did not change to a great extent the shape of the current density distribution diagrams. Two complementary approaches were used to determine the likelihood of flooding in the cell: one based on a water balance analysis and the other based on the estimating the mean gas velocity of reactants. It was noted that flooding conditions resulted from the impossibility of the anode to remove water diffusing from the cathode, leading to water condensation at the cathode and the anode. In turn, drying conditions resulted from excessive water removal of the water diffusing from the cathode upstream the flow fields.

A methodology to determine the amount of air bleed needed to mitigate the effect of CO in PEMFC was developed. The methodology is based on the analysis of the distributed performance of the cell and the estimation of the $CO_2$ molar flow rates at the anode inlet and outlet, which was assessed using a gas chromatograph. It was demonstrated that this methodology is suitable for studying the following aspects: i) the amount of air bleed needed to recover a desired level of performance of PEMFCs with continuous CO feed, ii) the amount of air bleed needed to oxidize the CO feed on a molar flow basis for different $H_2$ flow rates, iii) the amount of CO adsorbed/desorbed during a certain period of time and iv) the fraction of catalytic sites covered by CO. It was observed that the flow rate of $H_2$ affects both the extent and severity of the CO adsorption as well as the effectiveness of the air bleed. For the cases studied, it was found that air volumetric flow rates ≤ 1% (as a percentage of the $H_2$ flow rate at the anode inlet) are enough to mitigate the effect of CO at concentrations between 13-19 ppm and a cell operating temperature of 65 °C.

The CO poisoning dynamics of the anode catalyst was studied for CO concentrations between 0.18-1 ppm and three fuel utilizations in a single cell. CO was fed to the cell in a constant concentration and in a constant molar flow rate mode. It was observed a gradual decrease in performance when the CO was fed to the cell that was

attributed to the adsorption of CO onto de anode catalytic sites. It was demonstrated that the fuel utilization strongly influences the CO poisoning dynamics in PEMFC independently of the CO feed mode used. For lower fuel utilizations the decrease in performance of the cell was slower. The decrease in performance was even slower when the molar flow rate of CO was reduced. The anode exhaust gas composition was measured during the tests and the CO molar flow rate at the anode outlet was estimated accordingly. It was found that at lower fuel utilizations, the CO breakthrough was faster and higher in magnitude. It was proposed that the slower decrease in performance at lower fuel utilizations should be related to: i) a lower amount of CO that adsorbed onto the anode catalytic sites for similar periods of time, which led to a slower increase in the anode overpotential, and ii) a more even distribution of CO within the cell, which made more effective the internal air bleed. Furthermore, these results suggest that the CO poisoning dynamics of PEMFC systems with fuel recirculation is determined by the CO buildup in the anode loop.

Taking into account the results presented in this thesis, suggestions of future work can be made.

It was showed that evaluation of the current density distribution may contribute to optimize the performance of PEMFC, nevertheless, there is a lack of experimental work concerning SFC operated in hydrogen recirculation mode. The test bench incorporating the SFC operated in hydrogen recirculation mode should be improved. The improvements proposed include incorporation of a humidification device to the anode recirculation loop, refinement of the purge system regarding the amount of gas purged and incorporation of other ways to trigger the purge (i.e., based on the voltage-drop of the cell or pressure-drop of the anode).

A wider systematic study of the effect of the anode and cathode operating parameters on current density distribution should be performed using the SFC operated in hydrogen recirculation mode. The impact of impurities (i.e. CO, $CO_2$ and sulphur species) enrichment on the current density distribution should be also studied for impurities concentrations below 1 ppm. It is recommended to implement

suitable analytical techniques such as gas chromatography or mass spectrometry to analyze the composition of the gas recirculating in the loop.

The methodology to minimize the amount of air bleed should be applied as well under galvanostatic operation and for a cell incorporating Pt-Ru as anode catalyst. The differences in the amount of air bleed needed for the Pt and Pt-Ru catalysts should be assessed and critically compared. The results of Pt-Ru catalysts may contribute to define the hydrogen fuel specifications for stationary applications (ISO/DIS 14687-3 in enquiry stage).